Patient-specific gating scheme for thoracoabdominal tumor radiotherapy guided by magnetic resonance imaging

Yang Li

To cite this version:

Yang Li. Patient-specific gating scheme for thoracoabdominal tumor radiotherapy guided by magnetic resonance imaging. Medical Imaging. Université de Rennes; Southeast university (Nanjing, Chine), 2024. English. NNT : 2024URENS015 . tel-04693137

HAL Id: tel-04693137

https://theses.hal.science/tel-04693137v1

Submitted on 10 Sep 2024

COLLEGE DOCTORAL BRETAGNE | MATHS, TELECOMS INFORMATIQUE, SIGNAL SYSTEMES, ELECTRONIQUE

Université de Rennes

THÈSE DE DOCTORAT DE

L'UNIVERSITÉ DE RENNES

ÉCOLE DOCTORALE Nº 601
Mathématiques, Télécommunications, Informatique, Signal, Systèmes, Électronique
Spécialité : *Signal,Image,Vision*

Par
Yang LI

Patient-specific gating Scheme for Thoracoabdominal Tumor Radiotherapy Guided by Magnetic Resonance Imaging

Thèse présentée et soutenue à Rennes , le 03/06/2024
Unité de recherche : LTSI,UMR INSERM U 1099 and LIST, Southeast University, Nanjing, China
Thèse Nº : « si pertinent »

Rapporteurs avant soutenance :

Anne Humeau-Heurtier	Professeur, HDR, LARIS, Université de Angers
Jie XUE	Professeur, Shandong Normal University

Composition du Jury :

Président :	Jean-Louis DILLENSEGER	Professeur, Universite de Rennes
Examinateurs :	Anne Humeau-Heurtier	Professeur, HDR, LARIS, Université de Angers
	Jie XUE	Professeur, Shandong Normal University
	Jian ZHU	Professeur, Shandong Cancer Hospital and Institute
	Da CHEN	Professeur, Qilu University of Technology (Shandong Academy of Sciences)
Dir. de thèse :	Di GE	Maîtrede Conférences, Université de Rennes
Co-dir. de thèse :	Baosheng LI	Professeur, Shandong Cancer Hospital and Institute

Invité(s) :

Huazhong SHU	Professeur, Southeast University,Nanjing, China

ACKNOWLEDGEMENT

As I approach the completion of my PhD dissertation, I am filled with immense respect and gratitude for all those who have supported and helped me throughout my academic and life journey.

First and foremost, I extend my heartfelt thanks to my supervisor, Professor Li Baosheng. At Shandong Cancer Hospital, a fertile ground for research, Professor Li not only provided me with a top-notch research platform and cutting-edge projects but also guided me with his profound academic insight, rigorous scholarly attitude, and exceptional research capabilities. His mentorship will be a lifelong treasure for me.

I am deeply grateful to my on-campus advisor, Professor Shu Huazhong, who opened the door to the international academic community for me. He built an academic bridge between Southeast University and the University of Rennes in France. Professor Shu offered meticulous guidance in my research and provided tremendous assistance with study abroad procedures and school affairs, ensuring a smooth journey for my overseas studies.

During my time at the University of Rennes in France, I received generous teaching and attentive care from Professor GE Di. His profound academic knowledge, unique insights, and rigorous research attitude set a high academic standard for me. His teachings have been like spring rain, nourishing my heart and inspiring me to keep progressing on the academic path.

I also want to thank the teachers in the laboratory at Southeast University : Yang Guanyu, Chen Yang, Kong Youyong, Wu Jiasong, and Yang Chunfeng. They offered generous and kind advice on my studies and personal life.

At Shandong Cancer Hospital, I received strong support from Zhu Jian, Li Zhenjiang, and Li Yukun. They provided invaluable guidance in research topics and experimental design, and offered substantial support in data collection and processing, enabling me to complete my experiments and achieve academic results smoothly.

I am grateful to my lab mates Cao Qiang, Xu Zilong, Li Minghao, Gu Jiabing, Gu Yunbo, Yang Yu, He Bingsheng, and Zhang Bin. The days we struggled and grew together are some of the most precious memories of my life. Their companionship and support made

my academic journey less lonely, and their friendship is one of my most valuable assets.

During my studies in France, my friends Wu Fuzhi, Zhang Chen, Chen Meng, and Ma Qixiang gave me meticulous care and assistance. They extended a helping hand when I encountered difficulties and provided guidance when I was confused. Their friendship made me feel the warmth of home in a foreign country.

I must also express my special thanks to my boyfriend. His wisdom, talent, and perseverance have always been my role models. His companionship and support have strengthened my resolve and confidence on the path of scientific research, and his love has made me appreciate the beauty and happiness of life.

Lastly, I extend my deepest gratitude to my parents and sister. They are the most important people in my life. Their selfless dedication and silent support have allowed me to pursue my academic dreams without distraction. Their love is my greatest motivation and my most precious treasure.

Here, I once again express my sincere thanks to all those who have helped and supported me! I will always remember your kindness, continue to strive forward, and live up to your expectations and trust.

RÉSUMÉ

Contexte de l'étude

Le cancer reste une menace majeure pour la santé humaine mondiale, ayant un impact significatif sur la qualité de vie des patients. Le cas de tumeurs thoraco-abdominales, ou le cancer du poumon occupe la première place en termes de nouveaux cas diagnostiqués et de décès en Chine, suivi par le cancer du foie. Avec les progrès de la technologie dans la radiothérapie, son importance dans le traitement du cancer ne cesse d'accroître, avec environ 70% des patients atteints de cancer nécessitant une radiothérapie, et 40% des tumeurs pouvant être guéries par cette modalité [6][175].

Le traitement du cancer du foie implique une approche multidisciplinaire complexe, où la chirurgie est une intervention primaire, mais le rôle de la radiothérapie devient de plus en plus prépondérant. La radiothérapie stéréotaxique corporelle (SBRT) a montré une efficacité significative chez les patients, dépassant les autres modalités de traitement [160]. Cela souligne le rôle critique de la radiothérapie dans l'amélioration des résultats thérapeutiques et dans le développement de nouvelles options thérapeutiques. Quant au cancer du poumon non à petites cellules (NSCLC) représentant 80% des cas, les modalités de traitement sont la chirurgie, la chimiothérapie et la radiothérapie, la dernière occupant une part substantielle de 70% [175]. Malgré les progrès significatifs dans le traitement du NSCLC avec l'évolution des techniques en radiothérapie, la résistance à la radiothérapie reste un défi majeur, en particulier dans le NSCLC à un stade précoce.

La radiothérapie de précision vise à administrer une irradiation à haute dose ciblant précisément les tumeurs, épargnant les tissus normaux environnants, améliorant ainsi l'efficacité du traitement et réduisant les effets secondaires. Cependant, son application dans les tumeurs thoraco-abdominales rencontrent des défis en raison des mouvements de tumeurs induits par les activités respiratoires, entraînant des déplacements des tumeurs allant jusqu'en dehors du champ de traitement tout en y laissant les tissus normaux. La stratégie actuelle consiste à étendre le champ d'irradiation afin de garantir une dose adéquate, mais cela a pour conséquences des dommages excessifs aux tissus sains environnants. Par conséquent, la prise en compte des mouvements de tumeurs liés à la respiration est primordiale dans la radiothérapie de précision pour les tumeurs thoraco-abdominales.

Tout d'abord, la stratégie par synchronisation respiratoire est utilisée pour gérer le mouvement respiratoire en milieu clinique. Contrairement aux techniques du blocage de respiration, la synchronisation permettant la respiration libre du patient pendant le traitement est plus populaire, ne nécessitant pas une grande capacité pulmonaire. La figure 1(a) illustre le schéma de synchronisation, administrant sélectivement une irradiation lorsque la tumeur rentre dans une zone cible plus restreinte et calculée en temps réel (comme le montre la figure 1(b)). L'application de la synchronisation réduit considérablement la marge du volume cible planifié, entraînant une diminution des doses nocives pour les organes critiques environnants (comme le montre la figure 1(c)). Actuellement, les systèmes de radiothérapie en temps réel avec suivi de la tumeur (RTRT) sont largement utilisés pour la synchronisation respiratoire[139][144]. Ces systèmes suivent le mouvement de la tumeur pendant la respiration en surveillant en temps réel à l'aide de la fluoroscopie X stéréoscopique avec des marqueurs métalliques implantés. Cependant, il convient de noter que ce système est invasif, nécessitant l'implantation de marqueurs métalliques à l'intérieur du patient pour le suivi. En revanche, la synchronisation non invasive repose sur l'observation du mouvement de marqueurs externes en guise de signaux de déplacements de tumeurs, certes corrélés mais considérés comme moins précis avec un déphasage incertain.

L'introduction des systèmes accélérateurs linéaires guidés par IRM (MR-Linac), tels que Elekta Unity, a ouvert de nouveaux horizons dans l'acquisition des signaux de synchronisation de plus haute précision. Ces systèmes peuvent surveiller directement les tumeurs et les organes à risque (OAR) sans marqueurs fiduciaires implantés ni ceux de substitution externes pour localiser la cible du traitement. Bien que les systèmes MR-Linac aient progressé dans l'ajustement des cibles et des plans de traitement entre les fractions, ils ne peuvent toujours pas répondre complètement aux défis des déplacements de tumeurs et des OAR pendant la radiothérapie.

Pour parvenir à une adaptation en temps réel dans la radiothérapie guidée par IRM (MRgRT), plusieurs défis scientifiques persistent :

1. Algorithme efficace de suivi des tumeurs : La détection rapide de la morphologie et de la position de la tumeur à l'aide des images en mouvement (Cine-MRI) reste un obstacle majeur. Dans la pratique clinique, les tâches telles que la segmentation manuelle par des experts comme les radio-oncologues, sont chronophages et annuleraient l'intérêt de l'imagerie IRM de l'Unity pendant le processus de radio-

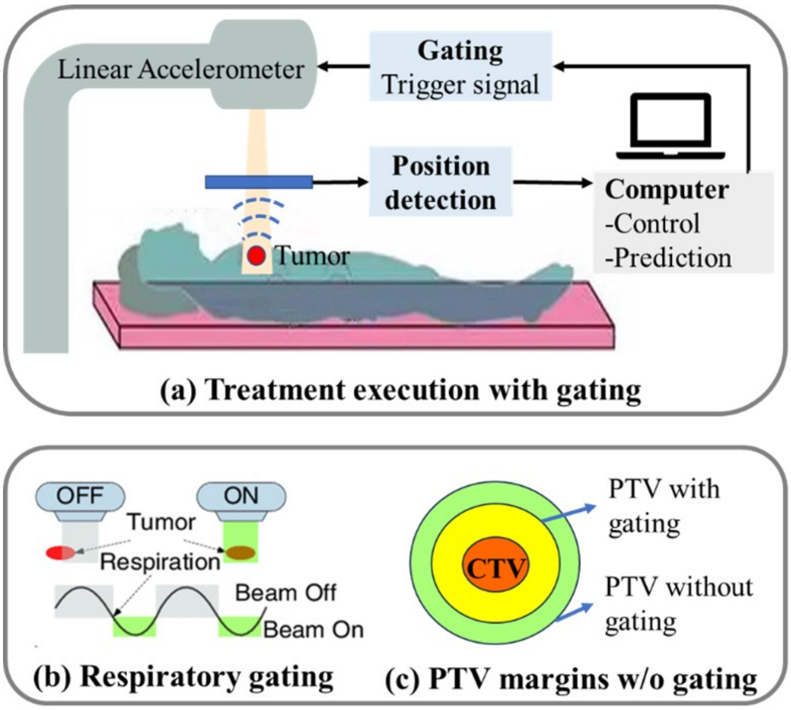

FIGURE 1 – Schéma de synchronisation pour la compensation des mouvements respiratoires.

thérapie.

2. Prédiction des signaux de synchronisation basée sur les données de mouvement acquises à basse fréquence : il y a un délai (latence) entre la détection du mouvement de la cible et la délivrance de la dose à la cible, période pendant laquelle la tumeur aurait pu bouger, entraînant potentiellement un décalage et une délivrance de radiation inexacte. Dans le cas de Elekta Unity, le délai globale du système est de l'ordre de 0,5 seconde, incluant le délai de l'acquisition par IRM, des traitements (segmentation et prédiction de la trajectoire de cible), et du déclenchement du faisceau d'irradiation. Pour compenser la latence du système d'Unity, il faut prédire en temps réel les positions de la tumeur et des structures internes critiques, posant ainsi un défi quant à l'efficacité des traitements de données sachant que la période d'échantillonnage du système par Cine-MRI est de l'ordre de 0,2s (5Hz).
3. Validation cross-modalité : Des revues récentes suggèrent que les méthodes linéaires montrent une efficacité suffisante dans la prédiction des signaux respiratoires sur la base de données CyberKnife. Cependant, en raison des différences dans les modes d'imagerie, les fréquences d'acquisition (30 Hz vs 5 Hz) et la latence du système

entre les systèmes guidés par rayons X et ceux par IRM, l'application directe de ces méthodes de prédiction peut ne pas reproduire les résultats escomptés. Par conséquent, la validation des méthodes linéaires des trajectoires de mouvement de la tumeur et des OAR obtenues à partir de données d'IRM ciné 2D est cruciale.

4. Évaluation complète dans le suivi et la prédiction des tumeurs, et validation dosimétrique : Les algorithmes de suivi des tumeurs visent à détecter précisément les positions des tumeurs dans les images de Cine-MRI au fil du temps, tandis que les algorithmes de prédiction estiment les positions futures pour la compensation de la latence du matériel. Comme les deux tâches sont généralement indépendantes, calculer les erreurs cumulées s'avère indispensable par une comparaison dosimétrique pour évaluer sa fiabilité du système de synchronisation proposé.

Contenu de la Recherche

L'objectif ultime de thèse est de développer un système de synchronisation de bout en bout pour la compensation en temps réel des mouvements lors du traitement du cancer du poumon et du foie sur l'Elekta Unity. La figure 2 montre le flux de travail et le contenu de la solution. Ce système surveillera et localisera automatiquement en temps réel la position spatiale tridimensionnelle de la tumeur, et prédira sa trajectoire dans 0.5 secondes. Un signal de synchronisation sera généré pour contrôler l'activation et la désactivation du faisceau pendant la radiothérapie, réduisant ainsi l'inexactitude dans la délivrance de la dose due au mouvement respiratoire. Pour atteindre cet objectif, les étapes suivantes ont été réalisées :

Un Flux de Travail de Suivi de Tumeur Basé sur KCF Utilisant l'IRM Ciné 2D pour la Radiothérapie Guidée par IRM (MRgRT)

Dans le contexte de la radiothérapie, la localisation précise des tumeurs est un aspect crucial appliqué avec succès dans la compensation des mouvements en temps réel pour les patients atteints de cancer du poumon. Diverses méthodes ont été proposées par les chercheurs pour le suivi des tumeurs dans les images IRM ciné 2D.

Le template matching (TM), qui cherche simplement la corrélation spatiale maximale entre le template (la cible) et l'image courante s'est avéré efficace dans le suivi des tumeurs et a été appliquée dans la radiothérapie de synchronisation MRIdian, bien que les coûts computationnels seraient significatifs sur les images de grandes dimensions ou des modèles complexes [149]. Pour contourner les calculs directs de la corrélation dans le domaine

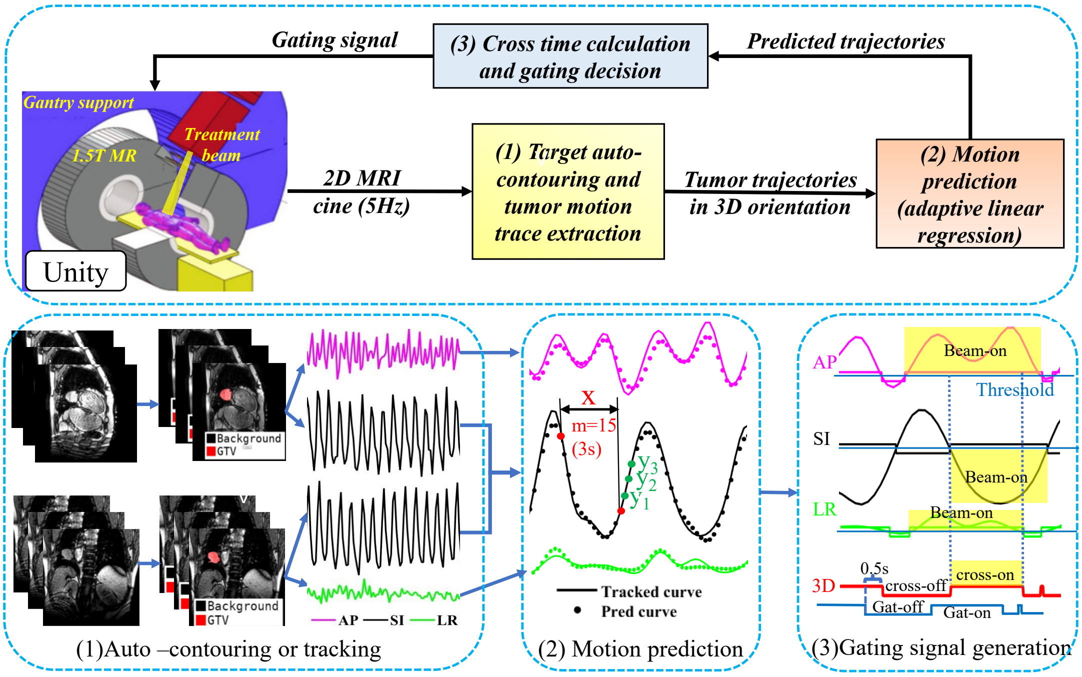

FIGURE 2 – Flux de travail du Schéma de Synchronisation en Ligne Spécifique au Patient.

spatial afin de réduire le temps de traitement, des filtres tels que le MOOSE [11] et le KCF [58] sont introduits pour réduire la complexité computationnelle en calculant la corrélation (proche de la convolution) dans le domaine fréquentiel par une transformation de Fourrier associée d'une approche de noyau (*kernel*). Ces méthodes ont été particulièrement efficaces dans le suivi de cibles dans des images naturelles. Les algorithmes MOOSE et KCF seront validés dans le suivi des tumeurs avec l'IRM ciné 2D dans la thèse.

De plus, en ce qui concerne la localisation de tumeur dans la direction supérieure-inférieure (SI), Seregni et al. [145] ont prouvé l'efficacité de l'approche avec deux directions de coupe (sagittal et coronal) pour le traitement guidé par IRM ciné 2D. Ils ont montré que les informations similaires sur la localisation sont obtenues à partir des deux plans. Cependant, en raison de l'irrégularité des bords des tumeurs malignes, la forme de la tumeur diffère généralement entre ces deux plans, introduisant ainsi de perturbations sur les algorithmes de la localisation de la tumeur.

Pour surmonter ces limitations, nous proposons une méthode de suivi de tumeur basé sur le KCF. Notre recherche vise à améliorer les performances de KCF grâce aux calculs de centroïdes et à la sélection de plans pour la localisation dans la direction SI. Nous avons cherché à remédier aux lacunes des méthodes existantes en fournissant une solution fiable par une approche patient-spécifique de compensation des mouvements en temps réel pour la radiothérapie de cancer thoracique et abdominal.

Pour valider la méthode proposée, nous avons initialement rassemblé une base de données comprenant des données de IRM ciné 2D de 10 patients atteints de cancer du poumon et 10 patients atteints de cancer du foie, collectées par l'Elekta Unity. Le dernier est composé d'un scanner IRM Achieva 1.5T et d'un accélérateur linéaire avec un faisceau non filtré de 7 MV, utilisant une fréquence d'imagerie de 5 Hz.

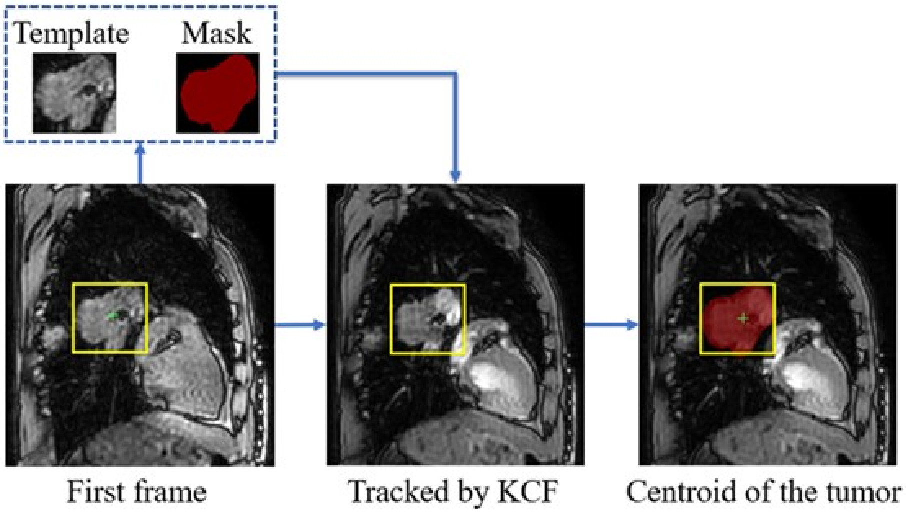

FIGURE 3 – Calcul du Centre de Masse Améliore le Suivi de la Cible. La boîte jaune délimite la limite de la tumeur dans la première image ou les images suivantes, tandis que le "+" vert représente le centre de masse de la tumeur dans la première image ou les images suivantes.

Le schéma est illustré dans la Figure 3. Pour chaque patient, est segmentée manuellement la tumeur sur la première image à l'aide de l'outil Labelme [138], générant un masque binaire de la tumeur pour le suivi ultérieur. L'algorithme KCF a été choisi pour le suivi, en déterminant la localisation par la réponse maximale. Le centre de masse des pixels couverts par le modèle dans cette région est ensuite pris pour la cible. Quant à la sélection entre le plan coronal et sagittal, la corrélation maximale entre le masque et les 20 images suivantes est utilisée comme critère de sélection.

Les résultats montrent que l'utilisation du centre de masse et la sélection de plans améliorent significativement les performances de KCF. Chez les 10 patients de cancer du poumon, les erreurs moyennes de suivi dans les directions Gauche-Droite (LR) et Antérieure-Postérieure (AP) ont diminué respectivement à 0,32 (34,7%) et 0,30 pixels (40%), grâce aux calculs de centroides. Pour la direction SI, en plus des calculs de centroïdes, la sélection de coupe a réduit davantage les erreurs de suivi de 24%. Chez les 10 patients de cancer du foie, la réduction des erreurs dans les directions LR et AP ont été réduites respectivement à 0,47 (45,3%) et 0,53 pixels (38,4%). Dans la direction SI, l'amélioraion par la sélection de coupe était de 15,3%.

Dans l'ensemble, notre méthode de suivi de tumeur basé sur KCF démontre une efficacité et une précision dans la localisation de tumeur avec l'IRM ciné 2D, marquant une étape importante dans la compensation des mouvements respiratoires en radiothérapie et jettant la base nécessaire pour l'étape de prédiction.

Prédiction du mouvement des tumeurs à l'aide du transfert C-NLSTM

Les réseaux neuronaux récurrents (RNN) et leur variante améliorée, les réseaux neuronaux à mémoire à court et long terme (LSTM), présentent des avantages dans la modélisation non linéaire pour la prédiction du mouvement respiratoire [7][110][92]. Les modèles *deep learning* nécessitent généralement de grandes quantités de données annotées pour l'entraînement. Cependant, l'obtention de telles quantités sur la plateforme Elekta Unity sera irréaliste. Pour contourner le manque de données, on introduit le transfer learning pour exploiter les modèles pré-entraînés et les connaissances des ensembles de données existantes afin de résoudre efficacement des tâches connexes avec un ensembles de données plus restreint.

Plus spécifiquement, le modèle C-NLSTM spécifique au patient, exploitant les connaissances des modèles pré-entraînés et des ensembles de données existants, a été adopté . Cette approche adresse efficacement le problème de la prédiction inexacte du mouvement respiratoire pour un petit ensemble de données.

Ce modèle est d'abord évalué avec deux bases de données disponibles publiquement, CyberKnife (137 patients, 25-132 min per recording)[36] et Fantasia (40 patients, 120 min per recording)[66], Les deux bases de données se composent de signaux respiratoires venant du marqueur de surface sans information sur les trajectoires réelles de la tumeur. Cependant, grâce au volume conséquent de données, elles évaluent adéquatement les capacités prédictives du modèle. Ensuite la validation du modèle de transfert C-NLSTM a été effectuée sur les données IRM collectées par l'Elekta Unity.

Le modèle de transfert C-NLSTM spécifique au patient (illustré dans la Figure 4), se compose d'un modèle C-NLSTM pré-entraîné et d'un modèle C-NLSTM cible, ce dernier prédira en temps réel les trajectoires de tumeurs sur IRM ciné 2D. Tout d'abord, nous avons pré-entraîné le modèle C-NLSTM sur les bases de données CyberKnife et Fantasia pour évaluer sa stabilité et la robustesse. Cela permet d'extraire et de simuler des motifs et

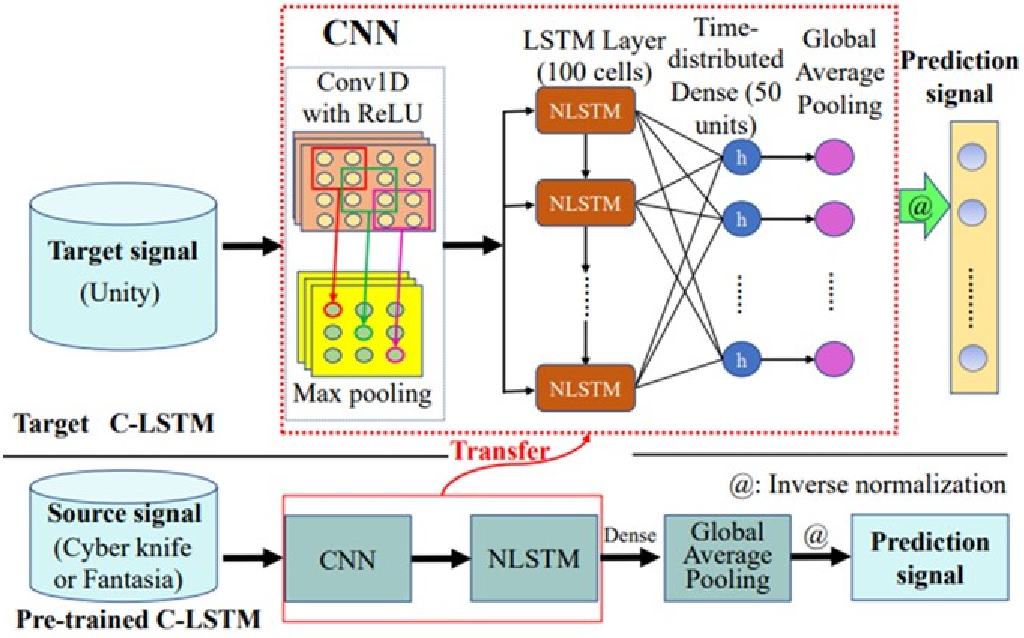

FIGURE 4 – Architecture du cadre de transfert C-NLSTM proposé.

des caractéristiques similaires au mouvement des tumeurs. Ensuite, nous avons initialisé le modèle C-NLSTM cible en utilisant les paramètres, la structure et les hyperparamètres du modèle pré-entraîné. Et enfin, le modèle cible a été optimisé sur les données Unity avec seulement les deux premières minutes pour chaque patient, avant de balayer sur les données restantes.

Les résultats montrent que cette approche par le C-NLSTM fonctionne bien sur les bases de données CyberKnife et Fantasia, et l'apprentissage par transfert améliore significativement les performances du modèle alors que les données pour optimiser le modèle cible ne durent que de 2 minutes. Les erreurs moyennes normalisées (nRMSE) de la prédiction sont réduites de 54,3%, 42,0% et 30,6%, dans les trois directions (SI, LR, AP) pour le cancer du poumon, et 48,4%, 41,0% et 43,9% pour le cancer du foie, en prenant la base de Fantasia pour préapprentissage et celle de Unity pour cible, mettant en évidence l'avantage significatif de transfer learning.

En conclusion, ce travail présente une solution innovante pour prédire les trajectoires de mouvement des tumeurs, mettant en évidence le potentiel de l'apprentissage profond et de l'apprentissage par transfert pour relever les défis des motifs d'imagerie complexes et des données d'entraînement limitées.

Gating en temps réel pour la compensation des mouvements respiratoires avec prédiction

Le signal de gating permet d'émettre de l'irradiation uniquement lorsque la tumeur rentre dans une région cible plus petite, connue sous le nom de "gating wondow" afin de réduire les doses nocives aux organes critiques environnants grâce à la prédiction du mouvement de la tumeur. Ce concept repose sur la surveillance des signaux respiratoires du patient, généralement obtenue par le biais de marqueurs externes ou d'imagerie. Par conséquent, la précision des signaux de gating joue un rôle crucial dans la compensation du mouvement respiratoire lors de la radiothérapie.

Les trajectoires de centroïdes de tumeurs des trois plans sont délimités par des radiologues expérimentés pour référence. Ensuite les mouvements dans les trois directions sont combinés en un seul vecteur 3D dans un espace euclidien. Les signaux de gating (binaires) de référence seront donc déterminés en vérifiant à chaque instant si le vecteur se trouve à l'intérieur de la région cible pour chaque patient.

Pour générer le gating en temps réel lors de la radiothérapie, la position future (de 0,4 s et 0,6 s) de tumeur sera estimée de façon séquentielle pour prédire le temps de croisement (dans un sens comme dans l'autre) de la région cible. Ce dernier avancé de 0,5 secondes correspond au déclenchement du signal de gating (passage de 0 à 1 ou l'inverse) pour compenser les retards du système. Dans la partie de prédiction, nous avons comparé de manière exhaustive trois modèles linéaires de prédiction avec trois modèles RNN, évaluant la précision du signal gating binaire généré avec des métriques temporelles. L'avantage en complexité des modèles linéaires a permis également le développement d'une approche patient-spécifique, dite la régression linéaire adaptative (ALR) qui s'initialise avec une période d'amorçage de 30 secondes (150 échantillons) pour chaque patient, et s'optimise au fil du temps pour mettre à jour ses paramètres.

La Figure 5 montre le schéma par seuillage de la trajectoire tumorale prédite pour une fenêtre de prédiction de 0,6 s. Le délai du système était de 0,5 s dans cette étude, donc les signaux de synchronisation idéaux devraient être avancés de 0,5 s par rapport au temps de croisement réel. Les signaux de gating binaires noir et rouge ont été générés en calculant le temps de croisement de référence et prédit, respectivement.

Pour l'application du modèle ALR sur des données cliniques réelles, nous avons observé d'excellentes performances, avec une précision de gating atteignant 98,3% et 98,0% pour le cancer du foie et du poumon, respectivement. Ces résultats montrent clairement la faisabilité et pertinence du modèle proposé dans des applications pratiques. Bien que

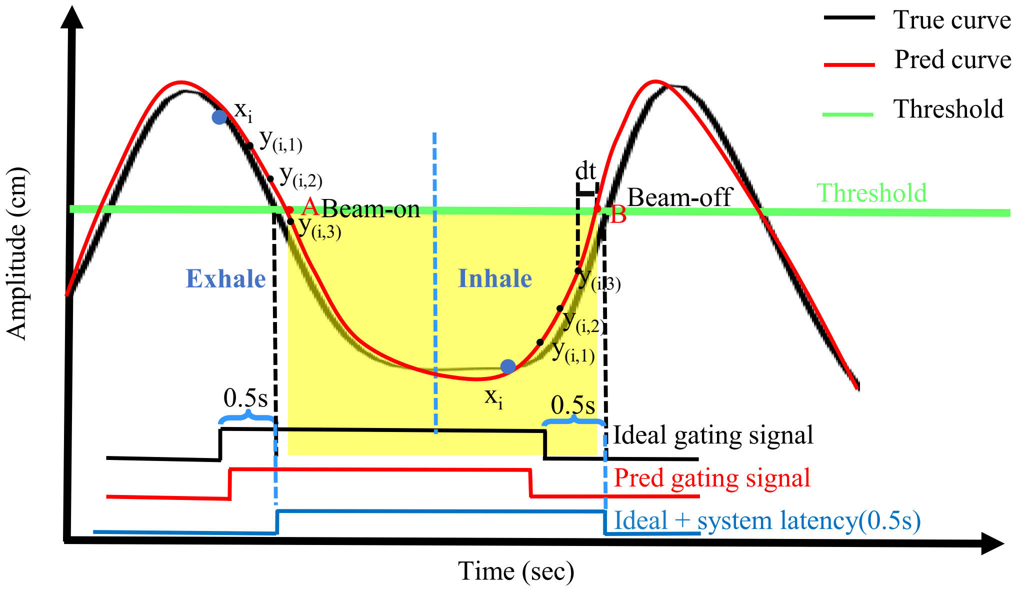

FIGURE 5 – Schéma de contrôle de la porte par seuillage de la trajectoire tumorale prédite pour une fenêtre de prédiction de 0,6 s.

le mode adaptatif entraîne une légère augmentation du temps de calcul, principalement concentrée sur la mise à jour des paramètres de régression linéaire (en moyenne de 1 ms), le temps de calcul global reste raisonnable.

En conclusion, notre méthode de gating est efficace et précise au vu des spécificités du système de l'imagerie et des retards associés, et constitue donc une solution viable pour la radiothérapie de précision avec l'Unity.

Gating patient-spécifique avec IRM ciné orthogonale

L'idée de gating par IRM ciné orthogonale est une extension naturelle au 3D pour planifier la radiothérapie. Seregni et al. [145] ont proposé une fenêtre sphérique comme région cible en analysant la fonction de densité de probabilité de la localisation de tumeur de chaque patient afin de déterminer le rayon du sphère, fixée à 30% de l'amplitude de mouvement 3D de la tumeur. Ils ont cherché à maximiser le cycle de service (pourcentage du temps d'irradiation effective sur la durée totale de radiothérapie) pour déterminer le centre du sphère, ce qui implique une isotropie dans les trois directions. Cependant, en analysant la courbe de mouvement respiratoire du patient, nous avons constaté que le mouvement de la tumeur dans la direction Supéro-Inferieure (SI) est significativement plus important que dans les deux autres directions (AP et LR). Par conséquent, le modèle de région cible sphérique proposé par Seregni et al. ne tient pas compte des spécificités des mouvements de la tumeur.

Notre objectif est de déterminer les paramètres optimaux d'un modèle pavé, noté E, pour représenter l'anisotropie des mouvements. Simultanément, nous visons à maximiser le cycle de service (nombre d'occurences où le centroïde de tumeur rentre dans le pavé E_{Ω}) tout en minimisant son volume $(vol(E_{\Omega}))$ correspondant au volume cible de planification (VCP).

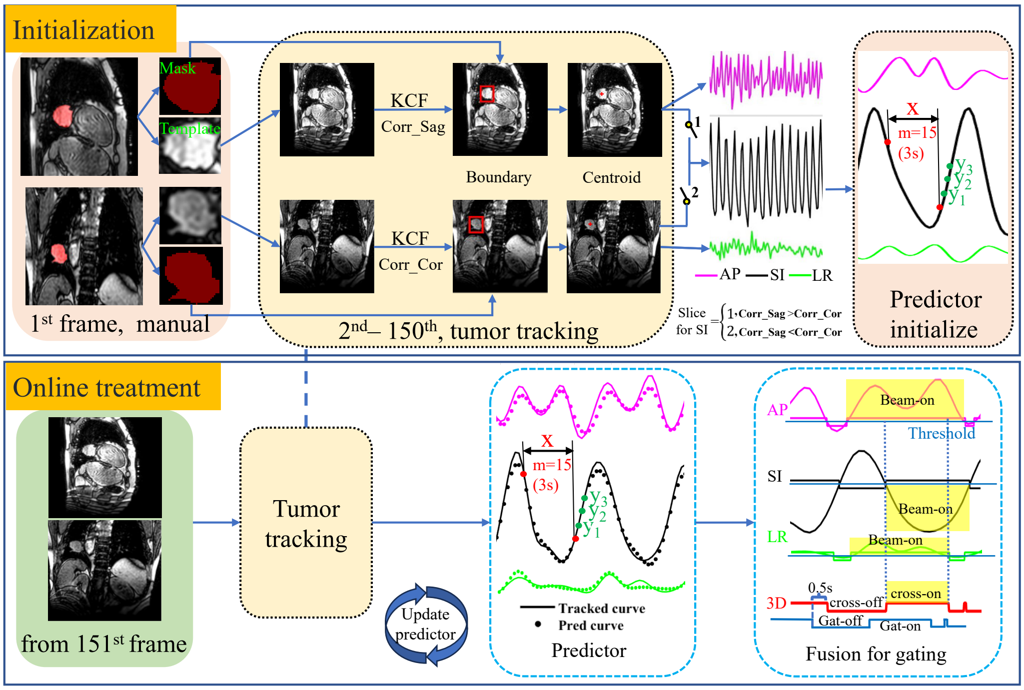

FIGURE 6 – Organigramme de la solution en ligne pour la gating 3D spécifique au patient en MRgRT.

Nous avons utilisé l'ensemble de données de IRM ciné 2D Le schéma de gating 3D proposé est illustré dans la Figure 6. Les dimensions du pavé optimal a été déterminée en fonction des amplitudes de mouvement des 150 premières images (30 s). À partir de la 151ème image, les étapes suivantes seront itérées : 1) localiser le centroïde de tumeur dans l'image courante, 2) prédire la position future de tumeur dans les 0,6 seconde , 3) mettre à jour le prédicteur en temps réel, 4) vérifier si la tumeur franchira la région cible et mettre à jour le signal de gating en fonction.

De plus, pour valider l'amélioration clinique avecle gating proposé pour les cancers du foie et du poumon, nous avons calculé l'extention d'irradiation autour de tumeur par la moyenne temporelle générés par le système proposé. Ces derniers permettent d'obtenir un nouveau PTV (PTV_{new}) et un nouveau plan de traitement (Plan2). L'histogramme dose-volume (HDV) résultant du Plan2 a été comparé avec le plan de traitement d'origine (Plan1).

Les résultats expérimentaux démontrent que le système gating proposé a atteint une précision de porte optimale. En tenant compte du mouvement tridimensionnel, la précision moyenne du signal de gating pour les cancers du poumon et du foie a atteint respectivement 93,6% et 91,3%. Il est à noter que le système a montré des améliorations significatives dans la protection des organes à risque environnants. Les indicateurs critiques pour le poumon droit et le cœur pour le cancer du poumon, ainsi que pour le foie normal et le rein droit chez pour le cancer du foie, ont montré des améliorations notables.

En résumé, nous avons introduit et validé avec succès une méthode d'optimisation du gating avec un modèle de pavé. C'est une solution en ligne efficace grâce à l'intégration de la localisation de tumeur et de la prédiction du mouvement. Cette recherche innovante ouvre une nouvelle voie pour la technologie gating en radiothérapie thoraco-abdominale, dans l'optimisation des plans de traitement.

Conclusion

Cette thèse présente un système de gating pour la compensation en temps réel des mouvements par IRM cine, avec un accent sur les patients atteints de cancer du poumon et du foie. Le système surveille en continu et localise automatiquement la position spatiale en 3D des tumeurs, et prédit les trajectoires des tumeurs dans les trois directions. Le système génère des signaux de gating pour contrôler précisément l'activation/désactivation du faisceau pendant la MRgRT, compensant les inexactitudes dans la délivrance de dose dues au mouvement respiratoire. Les contributions spécifiques sont les suivantes :

1. Validation de l'efficacité de KCF dans le suivi des tumeurs en 2D sur des images en IRM cine, plus efficace et précise par rapport aux méthodes traditionnelles (TM). La précision est améliorée en calculant le centroïde des pixels, et la sélection des plans (coronales vs sagittales) pour localiser les tumeurs dans la direction SI.
2. Proposition d'un modèle C-NLSTM spécifique au patient qui combine la préformation du modèle C-NLSTM et l'optimisation de la cible pour obtenir une meilleure prédiction du mouvement de tumeurs. Le transfer learning, en utilisant efficacement le modèle préformé sur un ensemble de données limité, est une solution pertinente face au manque de données de l'Elekta Unity. Le modèle montre une performance

satisfaisante dans la prédiction en temps réel pour la compensation du mouvement spécifique au patient.

3. Validation de la régression linéaire dans la prédiction du mouvement des organes ou des tumeurs en utilisant des images MR ciné 2D et proposition d'un schéma de prédiction en ligne pour les signaux de gating. Les signaux de gating sont déclenchés à l'aide de modèles prédictifs, prouvant son efficacité dans la MRgRT en comparant avec des modèles RNN.
4. Intégration des travaux susmentionnés, proposition d'une solution complète de compensation des mouvements respiratoires basée sur la IRM cine orthogonale. En optimisant un modèle de pavé et en explorant différents scénarios, des signaux de gating sont générés pour répondre aux besoins de traitement des différents patients. La validation par étude dosimétrique confirme que l'efficacité de la solution proposée dans la protection des organes environnants à risque.

En résumé, le système proposé est robuste et fiable, réalisant une adaptation en temps réel au mouvement des tumeurs en MRgRT. Il fournit un solide soutien pour la compensation du mouvement respiratoire dans le traitement des cancers thoraciques et abdominaux, servant d'outil essentiel pour la radiothérapie de précision.

Côté équipement, bien que les progrès technologiques de MR-Linac ait permis une nette amélioration dans la localisation et la prédiction du mouvement, certains défis techniques persistent dans la gestion du mouvement respiratoire pour les tumeurs thoraciques et abdominales. Équilibrer la résolution spatiale et temporelle de l'IRM, augmenter le contraste de tumeurs du foie en imagerie sont des défis actuels. Côté algorithmique, certaines pistes de peaufinement ne sont pas prises en compte dans l'étude, comme la segmentation de tumeur (au lieu de la localisation du centroïde) pour tenir compte de la déformation morphologiques, des modèles elliptiques plus sophistiqués (au lieu de pavé) et son optimisation pour davantage minimiser le volume sans réduire le cycle de service, sans oublier la possibilité de définir une extension de contour de GTV plus flexible dans la plannification.

En dehors des méthodes de gating, la technologie émergente par le suivi MLC [168] montre aussi du potentiel malgré les complexités supplémentaire dans les flux de travail cliniques. Cette approche MRgRT adaptative exige notamment une qualité et des tests et pourrait jouer un rôle plus important dans la protonthérapie à l'avenir. En conclusion, la gestion du mouvement respiratoire avec le MRI-Linac nécessite encore des développements et, avec l'expérience accumulée, la MRgRT en fera des progrès significatifs.

TABLE OF CONTENTS

LIST OF FIGURES

LIST OF TABLES

INTRODUCTION

Motivation

Cancer remains one of the major threats to human health worldwide, with its high mortality rate severely reducing patients' quality of life. Thoracic and abdominal tumors have a high incidence. Lung cancer is the top malignant tumor in China in terms of both incidence and mortality, follow by liver cancer closely behind in mortality rates. Radiation therapy technology plays an increasingly important role in cancer treatment, with approximately 70% of cancer patients requiring radiation therapy throughout their treatment process [6][175].

The emergence of precision radiotherapy has enabled high-dose radiation to be accurately focused on tumor sites, while better protecting surrounding normal tissue, improving treatment effectiveness, and reducing side effects. However, in the radiotherapy process for thoracic and abdominal tumors, due to close relationship the respiratory rhythm and the vary inform in breathing patterns, it may result in tumor leaving irradiation target and surrounding normal tissue entering the irradiation field, thereby affecting the accuracy of radiation therapy. Special attention needs to be paid to various aspects from imaging and treatment plan formulation to dose delivery, as respiratory motion needs to be taken into consideration in each step.

The goal of precision radiotherapy for thoracic and abdominal tumors is to precisely irradiate the tumor target while minimizing damage to organs at risk (OAR). However, dealing with the continuous tumor motion due to respiratory activity is a major challenge. Currently, the clinical strategy is to expand the irradiation field to ensure that sufficient therapeutic dose reach the target, but this inevitably causes excessive damage to surrounding healthy tissues.

Gating schemes reduce harmful doses to surrounding critical organs by limiting radiation delivery temporal periods of the tumor entering into a smaller target volume. Currently, real-time tumor tracking radiotherapy (RTRT) systems have been applied in respiratory gating. Its basic principle is to track the position changes of the tumor in real time through stereoscopic X-ray fluorescence microscopy by implanting fiducial markers.

It should be noted that this system is invasive as fiducial markers need to be implanted into the patient's body for tracking. Non-invasive gating mainly controls through external surrogate monitoring, instead of direct tumor motion monitoring. It is generally believed that external monitoring may not be accurate enough in comparison.

The emergence of MR-Linac systems such as the Elekta Unity (Elekta AB, Stockholm, Sweden) has opened up new possibilities for providing higher precision gating signals. These systems can directly observe tumors and internal structures, without relying on implanted fiducial markers or external respiratory signals to locate the treatment target area. However, clinical experiences have shown that quickly detecting the shape and position of the tumor on cine-MRI during MRI-guided radiotherapy (MRgRT) is still one of the main bottlenecks[74][149]. Additionally, there is a certain system delay between detecting the target movement and radiation being transmitted to the target, during which time the tumor may have already moved, potentially leading to displacement and inaccurate radiation delivery. Studies [85][169] have shown that the Elekta Unity can control the system delay time to within 0.5 seconds, including image acquisition, trajectory extraction, and beam switch triggering processes. To compensate for its overall system delay, it is necessary to predict in real-time the position of the tumor and important internal structures, for which the prediction algorithm is another challenge in achieving precise radiotherapy.

Objectives and Context

The ultimate aim of this paper is to develop an end-to-end gating system for real-time motion compensation during lung cancer and liver cancer treatment on the Elekta Unity. This system will monitor and automatically locate the three-dimensional spatial position of the tumor in real-time, and predict the tumor's motion trajectory in the Superior-Inferior (SI), Left-Right (LR), and Anterior-Posterior (AP) directions in advance. Based on the set gating rules, a unique gating signal will be generated to control the beam on and off during radiotherapy, thereby compensating for the inaccuracy of dose delivery due to respiratory motion. To achieve this goal, the following steps have been carried out :

1. Tumor Tracking Workflow Based on Kernel Correlation Filters

To address the issues of time consumption and accuracy in tumor tracking using Cine-MRI, we proposed a tumor tracking workflow based on Kernelized Correlation Filter (KCF). KCF [58] leverages Fourier transformation to enhance computational speed, effectively solving the time-consuming problem associated with Template Matching (TM) when dealing with large images or complex templates[149].

To address irregular tumor shapes and tracking errors caused by respiratory motion-induced deformation, we innovatively introduced a method to calculate the centroid of pixels covered by the template, significantly improving tracking accuracy. Additionally, to determine the optimal position of tumors in the SI direction, we proposed a strategy to select coronal or sagittal planes with stronger template correlation.

Results demonstrate that our proposed centroid calculation and SI direction optimizations significantly enhance the performance of KCF. In 10 lung cancer patients, the average tracking errors in the LR and AP directions decreased to 0.32 and 0.30 pixels, respectively, with centroid calculations reducing errors by 34.7% and 40%. For the SI direction, slice optimization further reduced tracking errors by 24%. In 10 liver cancer patients, errors in the LR and AP directions were reduced to 0.47 and 0.53 pixels, respectively, with centroid calculations decreasing errors by 45.3% and 38.4%. Slice optimization in the SI direction further reduced errors by 15.3%.

Our proposed workflow for tumor tracking based on KCF demonstrates efficiency and accuracy in 2D Cine-MRI, marking the first step in respiratory motion compensation for thoracoabdominal cancer patients undergoing radiotherapy and laying the foundation for subsequent work.

2. Transfer C-NLSTM Tumor Motion Prediction Algorithm Based on 2D Cine-MRI

Recurrent neural networks (RNNs) and their improved version, demonstrate advantages in nonlinear modeling for respiratory motion prediction [7][110][92]. Deep learning models typically require large amounts of annotated tumor motion data for training. However, obtaining such data on the Elekta Unity platform often poses challenges and is cost-intensive. To address this challenge, We proposed a patient-specific transfer C-NLSTM model for real-time prediction of tumor motion trajectories on 2D Cine-MRI.

Firstly, we constructed a C-NLSTM model and train it extensively using historical data to extract and simulate patterns and characteristics similar to tumor motion. We then utilized the parameters, structure, and hyperparameters of this pre-trained C-NLSTM model to initialize the Target C-NLSTM model. Subsequently, we further optimized the model using the first 2 minutes of data from each patient in the Unity databases, followed by a comprehensive evaluation of the proposed transfer model using the remaining data.

Results demonstrate that the C-NLSTM model performs well on the CyberKnife and Fantasia databases, and transfer learning significantly enhances model performance on the Fantasia and the Unity databases when training data is only 2 minutes. Transfer C-NLSTM reduced the average nRMSE of respiratory motion prediction by 54.3%, 42.0%, and 30.6% for lung cancer patients, and 48.4%, 41.0%, and 43.9% for liver cancer patients.

Overall, this study provided an innovative solution for predicting tumor motion trajectories, emphasizing the potential of deep learning and transfer learning in addressing challenges posed by complex imaging patterns and limited data.

3. Gating Signal Prediction Algorithm Based on 2D Cine-MRI

Compared to complex methods, linear methods demonstrated sufficient effectiveness in predicting respiratory signals collected during CyberKnife treatment [68]. However, considering the differences in imaging modes, sampling periods, and system delays, directly transferring prediction methods developed for X-ray guidance to MRgRT might have faced some challenges. This study aimed to validate the effectiveness of linear regression (Linear) in predicting internal organ or tumor motion trajectories in 2D Cine-MRI and proposed an online prediction scheme for gating signals to improve the accuracy of MRgRT for liver and lung cancer.

This study first predicted the position of the tumor after 0.4 seconds and 0.6 seconds, then updated the predicted threshold crossing time, triggered the gating signal 0.5 seconds (system delay) in advance. The study emphasized the comparison of the linear model with three latest RNN models (LSTM, Bi-LSTM, and GRU), and evaluated the accuracy of the generated binary gating signal using temporal metrics. Additionally, the study also proposed and evaluated an adaptive linear regression (ALR) model, which only used the data from the first 30 seconds of each patient as the training set, and updated the model parameters during online prediction.

Results demonstrate that when the system delay is 0.5 seconds, linear regression outperforms RNN models in both accuracy and efficiency. When the system delay is not a multiple of the MRI sampling period, overprediction (0.6 seconds) is a better choice compared to underprediction (0.4 seconds). Moreover, our proposed adaptive gate control signal prediction model exhibits outstanding performance on real clinical data, with average gate control accuracies of 98.3% and 98.0% for liver and lung cancer patients, respectively, strongly supporting the feasibility of the model in practical applications. Our proposed gate control scheme effectively addresses challenges posed by imaging patterns and system delays by predicting the gating signal in advance.

4. An efficient patient-specific gating scheme with 2D cine-MRI

Building upon previous work, this study proposes an end-to-end respiratory motion online solution based on 2D Cine-MRI, applied in the Elekta Unity's MR-Linac gated radiotherapy. This solution allows real-time monitoring and automatic localization of the tumor's three-dimensional spatial position, along with predicting its motion trajectory in three directions. By fitting the optimal cuboid and exploring different strategies, three-dimensional gating signals are generated to meet the treatment needs of various patients. Furthermore, to validate the clinical applicability of this system, we conducted dosimetric verification of the proposed gating system.

Results demonstrate that the proposed gating system achieves optimal gating accuracy. When considering motion in three dimensions, the average gate control accuracy for lung and liver cancer patients reaches 93.6% and 91.3%, respectively. Additionally, from the dosimetric results of 20 patients, the system significantly improves the protection of surrounding critical organs. For example, in lung cancer patients, the V_5 and V_{20} of the right lung, as well as the V_{40} of the heart, in Plan2 increased by 22.2%, 25.9%, and 22.6%, respectively. In liver cancer patients, the V_{30} and V_{40} of the normal liver in Plan2 increased by 15.3% and 20%, respectively, and the V_{10}, V_{15}, and V_{20} of the right kidney in Plan2 increased by 21.3%, 26.9%, and 26.2%, respectively.

Overall, the proposed gating system is robust and reliable, achieving real-time adaptation to tumor motion during MRgRT, ensuring the accuracy of three-dimensional gating signals throughout the MRgRT process. This provides strong support for respiratory motion-compensated radiation therapy for thoracoabdominal cancer patients and offers valuable tools for precise radiotherapy.

Contributions

The main contributions of this thesis are summarized as follows :

1. We outlined existing respiratory motion control strategies, analyzed the advantages of MRI-Linac, and identified challenges in compensating for respiratory motion. Then we introduced the goal of developing a gating system for real-time motion compensation during the MR-Linac treatment for lung and liver cancer patients. The details are described in Chapter 1.
2. We proposed a tumor tracking workflow based on KCF, addressing the issues of time consumption and accuracy in tumor tracking using 2D Cine-MRI. Firstly, we verified the efficiency and accuracy of KCF in 2D Cine-MRI tumor tracking. By calculating the centroid, we improved the situation where the fixed-size template

generated errors when the tumor shape changed, thus enhancing the tracking accuracy. In particular, we focused on the tracking in the SI direction by optimizing the selection of coronal slices or sagittal slices to determine the optimal position of the tumor in the SI direction. The details are described in Chapter 2.

3. We proposed a patient-specific transfer C-NLSTM model for real-time prediction of tumor motion, addressing the issue of insufficient training data. We constructed a C-NLSTM model, and introduced transfer learning to fully leverage the rich knowledge and feature representation capabilities embedded in the pre-trained model, while fine-tuning is conducted based on specific patient data to achieve high-precision prediction of tumor motion. Through this approach, the model can be trained with only two minutes of patient-specific data, effectively overcoming the challenge of data acquisition. The details are described in Chapter 3.
4. We proposed an efficient gating signal prediction method, overcoming the challenge of precise predictions in 2D Cine-MRI with limited sampling frequencies. We validated the effectiveness of linear regression for predicting internal organ or tumor motion in 2D MR cine. And we proposed an online gating signal prediction scheme based on ALR to enhance the accuracy of gating radiotherapy for liver and lung cancers. The details are described in Chapter 4.
5. We proposed an end-to-end gating system based on 2D Cine-MRI for the Elekta Unity MRgRT. It enables real-time monitoring and automatic localization of the tumor's 3D spatial position, prediction of tumor motion in three directions, and fitting an optimal cuboid (gating threshold) for each patient based on the tumor's motion range. Additionally, we explored various approaches to derive 3D gating signals based on tumor motion in one, two, or three directions, aiming to cater to different patient treatment needs. Finally, the results of dosimetric validation demonstrate that the proposed system can effectively enhance the protection of OAR. The detailed results are described in Chapter 5.

Chapitre 1

RESPIRATORY MOTION MANAGEMENT IN RADIOTHERAPY

This chapter presents the background of thoracic and abdominal radiotherapy and the current status of respiratory motion compensation techniques. Firstly, it delves into the background of thoracic and abdominal tumors, expounding the significance of radiotherapy in the treatment of oncology patients, and highlights the challenges respiratory motion poses to the accuracy of radiotherapy for these tumors. Secondly, various existing strategies for respiratory motion management are introduced. Subsequently, it discusses the advantages of MRI and the pressing issues to be addressed in radiotherapy. Finally, it outlines the main research work of this paper and the organization of the full text.

1.1 External Beam Radiotherapy

1.1.1 Thoracic and Abdominal Tumors

Cancer remains one of the diseases that pose a serious threat to global human health and quality of life, with high mortality rates. Among thoracic and abdominal tumors, lung cancer, liver cancer, esophageal cancer, colorectal cancer, gastric cancer, cervical cancer, and breast cancer have the highest incidence, accounting for 60% to 70% of all cancer cases. Among them, lung cancer has the highest incidence and mortality in China, with liver cancer mortality ranking second. According to global cancer epidemic statistics (GLOBOCAN) [161], there were approximately 2.2 million new cases of lung cancer and 1.79 million deaths from lung cancer worldwide in 2020, accounting for 11.4% and 18.0% of all new malignancies and deaths, respectively. In 2020, there were approximately 906 thousand new cases of liver cancer and 800 thousand deaths from liver cancer worldwide, accounting for 4.7% and 8.3% of all new malignancies and deaths, respectively.

As the country with the largest population base globally, China is facing unprecedented challenges in the prevention and treatment of lung cancer and liver cancer. In the past decade, with the aging of the population and the popularization of lung cancer screening nationwide, the incidence of lung cancer and liver cancer in the Chinese population has shown a slow but steady increase [161][194][19]. GLOBOCAN data show that [187], there were approximately 871 thousand new cases of lung cancer and 767 thousand deaths from lung cancer in China in 2022, accounting for 18.1% and 23.9% of all malignancies and deaths worldwide, respectively. In 2022, there were approximately 431 thousand new cases of liver cancer and 412 thousand deaths from liver cancer in China, accounting for 8.9% and 12.8% of all malignancies and deaths worldwide, respectively. Therefore, the treatment and prevention of lung and liver cancer play a crucial role and their importance is obvious.

The treatment of liver cancer requires the participation of multiple disciplines and multiple treatment modalities, including surgical resection, liver transplantation, radiofrequency ablation, arterial embolization/chemoembolization, systemic chemotherapy, radiotherapy, and molecular targeted therapy. Surgery remains the main curative treatment for liver cancer. The classic molecular targeted drug for liver cancer is sorafenib, but its use can only increase the median survival time of HCC patients by 3 months [97], and the objective response rate is only 2%-3% [105]. Systemic chemotherapy is the most recommended method for advanced and recurrent liver cancer [56], but liver cancer patients are often insensitive to chemotherapy, and resistance and drug resistance to chemotherapy drugs are one of the main reasons for treatment failure in patients. The overall efficacy of liver cancer treatment is still unsatisfactory.

Radiotherapy plays an increasingly important role in cancer treatment, and about 70% of cancer patients require radiotherapy intervention throughout their treatment. In recent years, clinical studies related to liver cancer SBRT have shown significant benefits in survival. For example, a study by Su et al. [160] in 2017 compared the efficacy of SBRT with surgical resection for stage 1a hepatocellular carcinoma and found no significant difference in the 1-, 3-, and 5-year overall survival rates between SBRT and surgical resection patients. In addition, another study published in Hepatology in 2020 [54] compared the survival difference between SBRT and radiofrequency ablation and found that SBRT and radiofrequency ablation had similar 3-year overall survival rates, but SBRT showed advantages over radiofrequency ablation in terms of 3-year local recurrence.

Non-small cell lung cancer (NSCLC) accounts for approximately 80% of the total cases of lung cancer [96]. Its treatment involves multidisciplinary cooperation including surgery, radiotherapy, chemotherapy, targeted therapy, immunotherapy, and individualization [174]. 70% of all patients with lung cancer have an evidence-based indication for radiotherapy, although it is often underutilized [175]. Radiotherapy can be used as curative or palliative treatment across all stages of disease. In recent years, radiation therapy has made significant progress in the treatment of NSCLC, which has benefited from the continuous development of radiation physics and radiation biology.

For early stage patients, large-fraction stereotactic radiotherapy can achieve even the equivalent efficacy of surgery [21]. At the same time, conventional intensity-modulated radiotherapy (IMRT) is not only equivalent to 3D-CRT in effectiveness, but also significantly reduces the incidence of radiation pneumonia [26]. However, radiation resistance remains a major cause of poor local control and recurrence in NSCLC, with the local recurrence rate of even early stage NSCLC still being as high as 10-30% in large fractionation radiotherapy (HFRT) [33]. In conventional fractionation radiotherapy, local recurrence remains the main cause of treatment failure, accounting for over half. Therefore, it is urgent to conduct in-depth research on the pathways and regulatory mechanisms involved in cell death induced by radiotherapy, and to explore effective targets for enhancing radio sensitizing, as well as developing targeted radiation therapies, which are crucial issues for current researchers to address.

1.1.2 External Beam Radiotherapy and Its Procedure

External Beam Radiation Therapy (EBRT), also known as radiotherapy, is one of the main treatment modalities in modern cancer therapy. It utilizes a linear accelerator to precisely direct high-energy radiation to the tumor tissue to suppress or destroy cancer cells (shown in figure 1.1). EBRT is used to kill cancer cells, reduce tumors, and alleviate cancer symptoms, and can be the sole treatment or used before surgery to reduce tumors, after surgery to eliminate residual cancer cells, and for managing symptoms of benign tumors. In clinical practice, the following forms of external radiotherapy are commonly used :

Two dimensional radiation therapy (2D-RT) uses hand-contact or 2D X-ray fluoroscopy/film imaging to determine the irradiation range, and then passes through a low-melting-point lead baffle or tungsten gate to form a rectangular or combination of irregularly shaped irradiation fields to irradiate tumors.The main modality of 2D-RT is deep X-rays, The main modes of 2D-RT are deep X-rays, 60Co therapy, high-energy X-rays and electron beam radiotherapy, which have the advantages of wide range of application

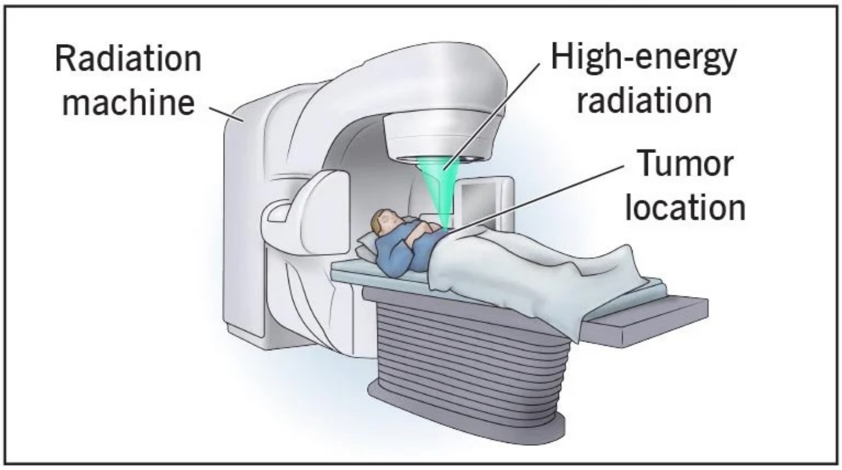

FIGURE 1.1 – Schematic Diagram of External Beam Radiation Therapy.

and fast irradiation speed, and play a very important role in the early stage of tumor radiotherapy. The main disadvantage of 2D-RT lies in the fact that the irradiation field can not be shaped to match the shape of the tumor, which leads to the irradiation of too many normal tissues and the probability of radioactive damage. At present, 2D-RT is still used in some tumor radiotherapy, but it is gradually replaced by the precision radiotherapy technology represented by conformal radiotherapy.

Stereotactic Body Radiation Therapy (SBRT) [16] is a kind of precise radiotherapy for tumors by using stereotactic technology and X-ray knife as the carrier of linear accelerator. It can complete a few (5-10 times) high-dose radiotherapy in a short time. Stereotactic radiosurgery (SRS) [16] uses high-dose concentrated radiation to accurately destroy small brain tumors, usually no more than 3 times of high-dose radiotherapy, to achieve the same effect as surgical resection of the tumor. SRT and SRS are especially suitable for small volume tumors. Through precise positioning and high-dose radiation, it can minimize the damage to surrounding normal tissues, and provide personalized, non-invasive treatment options.

Three-dimensional conformal radiation therapy (3D-CRT)[5] marks the transition from two-dimensional radiotherapy to three-dimensional precision radiotherapy. It uses CT scans and computer software to create a three-dimensional model of the tumor, and adjusts the shape of the radiation field from a common square or rectangular shape to the shape of the tumor using multileaf collimators (MLC) or conformal lead block technology. Through isocenter technology, a dose distribution similar to the shape of the tumor is formed from different angles in three dimensions. 3D-CRT is the starting point for precise radiotherapy for tumors, with advantages such as dose distribution that fits the shape of the tumor, fast radiotherapy speed, and low equipment requirements. However, 3D-CRT does not fully consider the uniformity of dose within the tumor. It is undeniable that before the wide application of inverse intensity modulated radiotherapy, 3D-CRT has been a representative technology for precise radiotherapy for a long time.

Intensity-Modulated Radiation Therapy (IMRT) [13] is currently the most widely used radiation therapy technique worldwide. It achieves precise control of dose intensity distribution by segmenting the irradiation field from each angle in traditional 3D-CRT into multiple small fields. This approach is more in line with the actual tumor burden, considering factors such as the quantity and distribution density of tumor cells. IMRT not only ensures that the shape of the irradiation field matches the target area but also enables a uniform distribution of the dose within the target area. Its main drawbacks include long irradiation time, multiple scattering beams, and low radiation utilization efficiency.

Volumetric Intensity Modulated Arc Therapy (VMAT) [184] is a form of IMRT. During the continuous rotation of a linear accelerator, VMAT dynamically adjusts the shape of the multi-leaf collimator (MLC) and the dose rate. Compared to traditional IMRT, VMAT can complete irradiation more quickly, with an irradiation speed comparable to 3D-CRT. Helical Tomotherapy (HT) [102] addresses the challenges of IMRT for tumors with unusual shapes or lengths ($\geq$ 40cm). HT utilizes an aerodynamic binary MLC and combines continuous rotation of a helical CT-like tube with synchronous movement of the treatment bed, delivering radiation in a manner similar to helical computed tomography scans. The greatest advantage of HT lies in its optimal dose distribution, often considered the "gold standard." However, its drawback is the long irradiation time, comparable to traditional IMRT.

Image-Guided Radiation Therapy (IGRT) [30] is the primary method to ensure the accurate positioning of tumors. IGRT can be broadly categorized into General IGRT and Specific IGRT. General IGRT refers to all imaging modalities that can provide images of tumors or surrounding normal tissues, including X-ray imaging, CT, Positron Emission Tomography-CT (PET-CT), MRI, ultrasound, Electronic Portal Imaging Device (EPID), and others. Specific IGRT specifically pertains to imaging methods within the treatment room, such as kilovoltage cone-beam CT (CBCT), X-ray fluoroscopy, two-dimensional radiography, CT-on-Rail, as well as megavoltage (MV) CBCT, MV EPID, and others.

Specific IGRT places greater emphasis on real-time guidance of patients on the treatment bed. Its main purpose is to correct positional errors, compensate for tumor position errors caused by physiological motion, track changes in tumors and normal tissues, and assess in real-time whether the dose distribution is reasonable. MRI, with its high soft tissue resolution, absence of radiation, and multi-dimensional functional imaging advantages, is destined to become the primary form of IGRT when combined with accelerators.

Proton therapy utilizes protons [39] rather than photons (X-rays) for radiation treatment. For certain patients, proton therapy can achieve radiation doses similar to those with photons while reducing radiation exposure to healthy tissues.

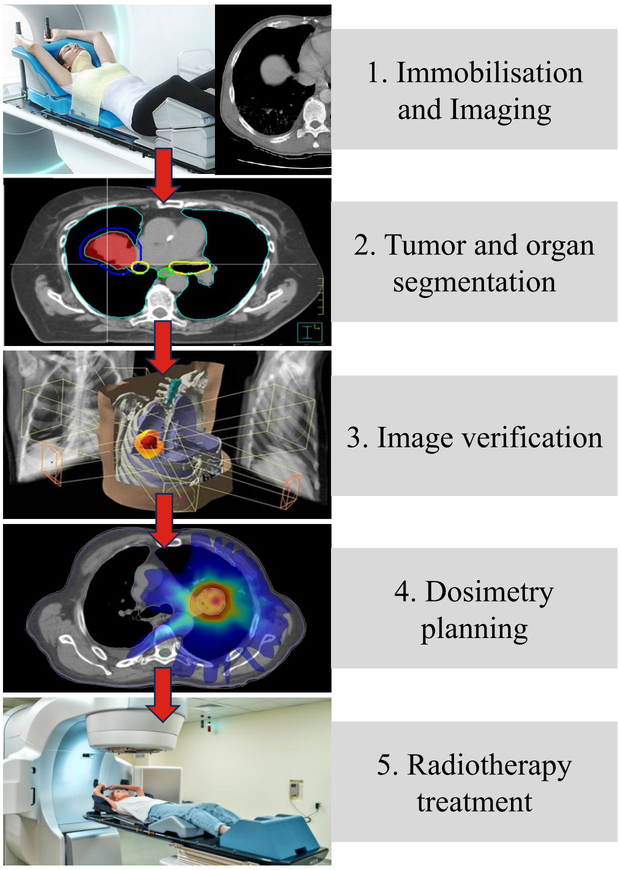

Figure 1.2 – Common clinical workflow of EBRT.

The process of EBRT typically involves multiple key steps, as shown in figure 1.2, including the following : after the doctor conducts a preliminary evaluation and determines the radiotherapy plan, the first step is positioning, where precise positioning and good reproducibility of the position are crucial for radiotherapy. In the case of simulated radiotherapy, X-ray and CT images are obtained to obtain tumor location information. Subsequently, the doctor delineates the target and critical organs based on the simulation data, verifies and adjusts the accuracy of delineation through reconstructed three-dimensional images. Then, the physicist designs the treatment plan based on the prescription doses specified by the radiation oncologist. The radiotherapy can only be implemented after the irradiation position and dose verification have passed. The radiotherapy technician positions the patient to ensure that the patient is fixed in the same position as during the simulated positioning. The radiotherapy process is carried out within the planned time frame, typically lasting only a few minutes each time. Conditioned equipment can use technology to monitor tumor location during radiotherapy to ensure the accuracy and precision of treatment. Finally, after the treatment is completed, the treatment effectiveness is evaluated and monitored.

1.1.3 Impact of Respiratory Motion on Radiotherapy

The goal of precision radiotherapy is to maximize treatment effectiveness while reducing damage to healthy tissues. Although technologies such as 3D-CRT, IMRT, and IGRT allow for the shape and dose distribution of the target volume to be conformal, in the process of radiotherapy for thoracic and abdominal tumors, the position of these tumors changes with the patient's respiration, causing the tumor to overflow the irradiation target and surrounding normal tissues to enter the irradiation field, which can affect the accuracy of radiotherapy. Their position changes with the patient's respiratory cycle, leading to potential tumor escape from the irradiation target area and the inclusion of surrounding normal tissues in the radiation field. This variability may affect the precision of radiotherapy.

Due to the strong individual differences in respiratory motion and the apparent variations in a patient's breathing at different times, it is challenging to describe respiratory motion using a unified model. In recent decades, with the development of imaging technologies, significant progress has been made in the use of images for diagnosis and treatment planning. However, challenges persist in dealing with image artifacts caused by respiratory motion and organ motion during the radiation process. These challenges remain a hurdle in achieving precision radiotherapy for thoracoabdominal tumors, requiring consideration of respiratory motion in various aspects from imaging and treatment planning to dose delivery. Addressing the impact of respiratory motion on the accuracy of radiation therapy has become a focal point in the research of thoracoabdominal tumor radiotherapy techniques.

Firstly, traditional static images may not accurately reflect the true position of the tumor due to respiratory-induced tumor movement. To solve this problem, healthcare professionals often use 4D CT scanning technology to obtain images at different respiratory stages, thereby more accurately describing the spatial location changes of the tumor. These images help doctors better understand the characteristics of tumor movement and provide reference for treatment planning. Secondly, respiratory motion needs to be fully considered during treatment planning. Typically, radiotherapy plans are designed around a region called the planning target volume (PTV) to ensure that the tumor receives appropriate irradiation throughout the treatment process [43]. However, due to respiratory-induced tumor movement, the PTV may require a larger margin to cover the changes in tumor position at different respiratory phases. This means that radiation needs to cover a broader area, while also increasing the dosage to surrounding normal tissues. Finally, respiratory motion may cause tumor positional shifts, thereby affecting radiotherapy accuracy. Sufficient consideration should be given to this factor in dose delivery in order to ensure the accuracy of radiotherapy.

With the development of Image-Guided Radiation Therapy (IGRT) technology, real-time anatomical images of the tumor and organs at risk during treatment are incorporated, allowing for the correction of treatment positioning. The application of IGRT technology can, to some extent, reduce the need for extensive expansion margins beyond the PTV, thereby minimizing radiation toxicity to normal tissues. However, it still cannot completely eliminate the impact of issues such as respiratory motion on the initial treatment plan during the radiation process.

1.2 Management of Respiratory Motion

In the process of thoracoabdominal tumor radiation therapy, respiratory motion stands out as a critical factor affecting treatment precision. To address this challenge, a variety of respiratory motion management strategies have emerged as focal points of research. These encompass techniques such as abdominal compression, respiratory control, respiratory gating, and real-time tumor tracking. These strategies have demonstrated significant advancements in improving the precision of thoracoabdominal tumor radiation therapy, minimizing unnecessary radiation damage, and consequently enhancing treatment efficacy and safety. However, it is essential to acknowledge that these strategies still face certain limitations and constraints. Further research and refinement are needed to provide a more comprehensive and accurate foundation for clinical practice.

1.2.1 Abdominal Compression

Abdominal compression (AC) technology is a respiratory motion management method used to alleviate the impact of abdominal organ movement on thoracic and abdominal cancer radiotherapy. This technique limits abdominal movement by applying external pressure, thereby reducing tumor positional changes and enhancing radiotherapy accuracy. AC technology is mainly applied to tumors located in the thoracic and abdominal regions, such as lung cancer, liver cancer, pancreatic cancer, etc. In AC technology, patients typically need to wear a special device, such as an abdominal compression belt or an abdominal compression pad. This device exerts a certain degree of pressure on the patient's abdominal area, reducing diaphragmatic deviation by stabilizing abdominal position and limiting organ movement while still allowing normal respiration. Therefore, during radiotherapy treatment, tumor positional changes are reduced, thereby improving treatment accuracy and effectiveness. Figure 1.3 shows the patient setting using Elekta's BodyFIX abdominal compression device in SBRT, and the accuracy and reproducibility of this technology have been studied [121][98][10].

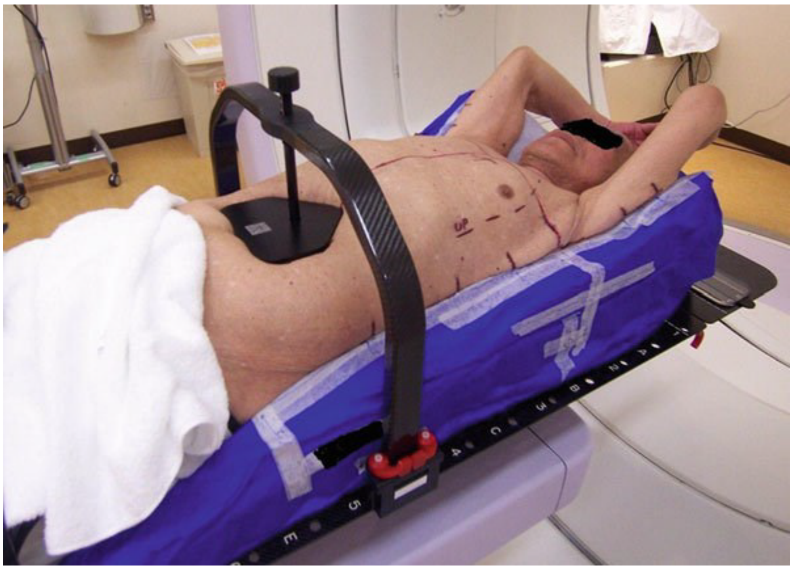

FIGURE 1.3 – Patient setup using Elekta BodyFIX abdominal compression device.

Negoro et al [121] found that using pressure plates can reduce tumor motion in 10 out of 11 patients . Without abdominal compression, the range of tumor motion in these patients was 8-20 mm (average 12.3 mm), while using pressure devices reduced the range of tumor motion to 2-11 mm (average 7.0 mm). It should be noted that AC technology is not applicable to all patients. For example, AC technology may worsen the condition or cause other complications in patients with poor pulmonary function, dyspnea, or abdominal surgical scars. Additionally, the effectiveness of AC technology may be influenced by factors such as pressure level, pressure distribution, and patient compliance. If the pressure level is too high or the pressure distribution is uneven, it may cause increased abdominal compression sensation and affect patient respiration and comfort levels. At the same time, if patients are unwilling to actively cooperate with using AC devices due to poor compliance, it will also affect the effectiveness of this technology. Therefore, when selecting AC technology for use, it is necessary to evaluate the specific situation of patients to ensure its applicability and safety.

1.2.2 Respiratory Control

Active Breathing Control (ABC) is a technology that uses a ventilator to temporarily limit the flow of air in patients. This technology monitors and controls the inhalation and exhalation volume of patients digitally by calculating the respiratory cycle curve, making it possible to monitor and control the respiratory cycle in real time [185][45]. By using the ABC technology, the inhalation and exhalation paths of patients can be temporarily closed at a predetermined flow rate and respiratory volume. Figure 1.4 demonstrates active breathing control system of Elekta. The patient is placed in the supine position by a fixation device and prevented from nasal breathing by a nose clip to ensure breathing only through the mouth. Additionally, multimedia glasses serve as a display unit and use a unique optical system to enlarge computer images generated on small liquid crystal display screens, allowing the patient to visualize the flow time curve and display the states of inhalation, exhalation, and apnea. During radiation therapy, the radiation beam is synchronized with the patient's actively paused breath time, which is typically comfortable for the patient and lasts for 15 to 20 seconds. The advantage of ABC technology is that it can reduce respiratory motion artifacts and tumor movement during treatment, thereby reducing the treatment margin. However, one drawback of this technology is that patients may feel discomfort, and it may not be suitable for patients with respiratory dysfunction.

Voluntary Breath-Hold (VBH) is a method similar to ABC technology that delivers

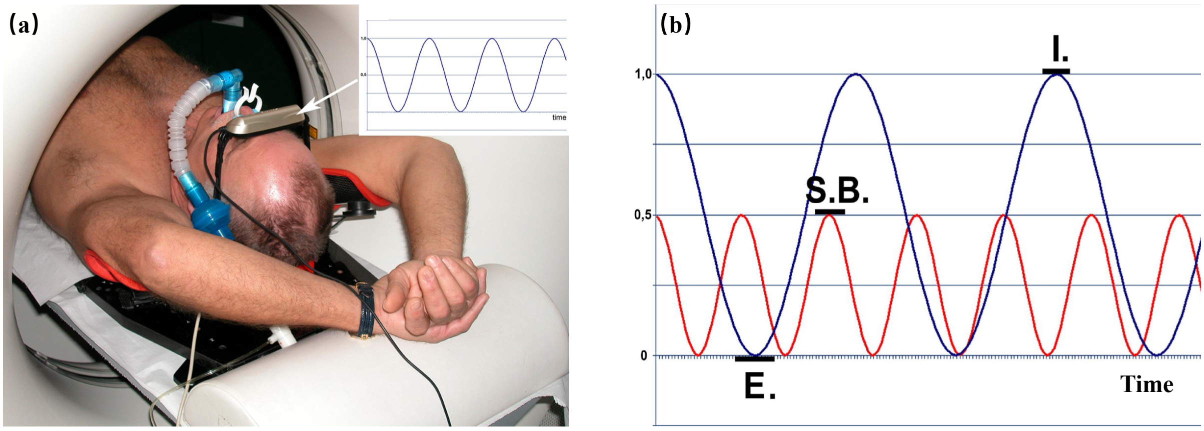

FIGURE 1.4 – Elekta's Active Breathing Control system. (a) Patient is placed in the supine position using a fixation device, and a multimedia glasses display unit shows the flow time curve. (b) Graphic display of the respiratory cycle (blue curve = normal breathing, red curve = shallow breathing) ; breath-holding preset. E = exhalation ; I = inhalation ; S.B. = shallow breathing.

radiation while the patient holds their breath to minimize the impact of breathing on treatment. Unlike ABC, VBH allows patients to independently control their breath holding without using a ventilator [77]. For all breath-holding techniques, patients are typically trained before simulation and treatment. They hold their breath at a specific stage of the respiratory cycle, and the therapist controls the radiation beam from the accelerator based on the patient's breathing pattern. If the patient is unable to continue holding their breath, they can terminate the radiation treatment at any time. It should be noted that this technique is based on the assumption that the patient's breath-holding behavior and related internal anatomical organs and structures are reproducible during each treatment session. If this assumption is invalid, it may impact the treatment's effectiveness.

Deep Inspiration Breath-Hold (DIBH) is a method similar to ABC that involves patients taking a deep inspiration and holding their breath while receiving treatment, which fills their lungs with air and pushes the heart away from the chest wall, reducing the risk of radiation exposure to the heart [53]. This technique is particularly useful in situations where radiation is needed for the chest region but avoidance of radiation to the heart is necessary, such as for left breast cancer treatment. The ABC system adds precision and reproducibility to the DIBH concept, providing all the necessary functions for implementing breath-holding techniques and offering more options and possibilities for radiation therapy improvement. DIBH requires patients to maintain the same deep inspiration breath-holding state during both CT simulation scanning and treatment, with lung

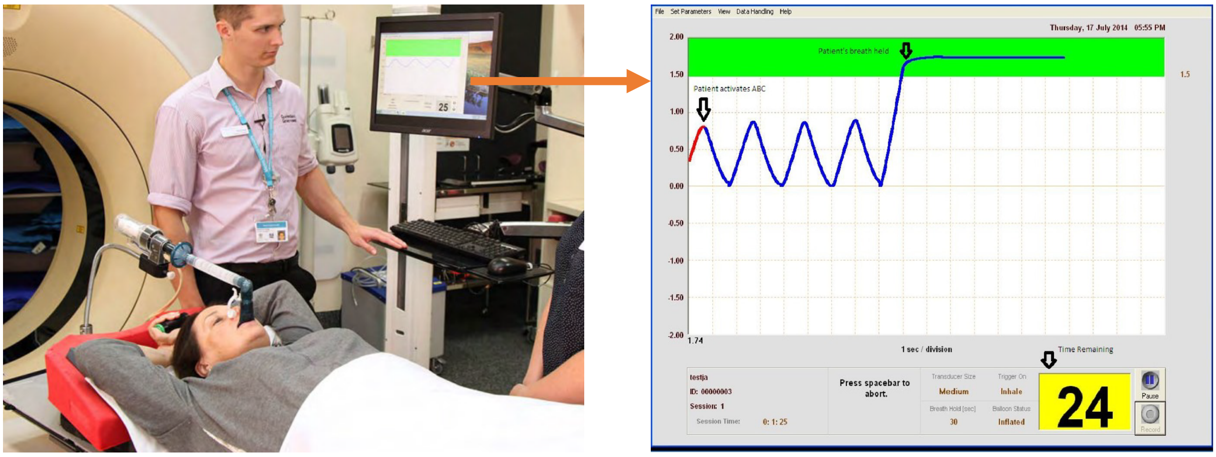

testja
ID: 00000003
Session: 1
Session Time: 0: 1: 25
Press spacebar to abort.
Transducer Size: Medium
Trigger On: Inhale
Breath Hold [sec]: 30
Balloon Status: Inflated

FIGURE 1.5 – Example of a patient undergoing DIBH. The patient maintains the treatment position on the accelerator, breathes through a spirometer mask, and the respiratory level is monitored. To prevent nasal breathing, a nose clip is used. The right figure shows a screenshot of the ABC monitor during DIBH treatment.

expansion levels monitored by a respiratory monitor. Patients breathe through a mask connected to the respiratory monitor and typically use a nose clip to prevent nasal breathing (shown in figure 1.5). Compared to voluntary breath-hold techniques, DIBH is more accurate because it uses respiratory monitoring. Deep inspiration breath-hold techniques have numerous advantages in radiation therapy, such as reducing radiation exposure to the heart, but they also have some disadvantages. Patients need to actively cooperate by holding their breath, which may be uncomfortable for some patients. Additionally, this technique is not suitable for all treatment situations and is typically only used in specific cases where radiation exposure to critical organs such as the heart needs to be avoided. Potential psychological stress is also a consideration because some patients may feel anxious or burdened. Therefore, when applying deep inspiration breath-holding techniques, it is necessary to comprehensively consider the patient's condition to achieve the best treatment outcome.

1.2.3 Gating

In 1987, a US research team observed that treating patients during a deep inspiration can help protect specific areas of the lungs, and thus proposed the concept of "breath-gated radiotherapy". Subsequently, the term "gating" was used to describe various practical methods [48][180]. In 1989, Japan first developed breath-gating technology, which used a microwave oscillator to control the radiation ON/OFF based on the gating signal, and measured the pressure of the patient's thoracoabdominal region using a balloon sensor. The results showed that this technique could achieve more accurate treatment for tumors located near the diaphragm [123].

In the field of breath-gating, two main approaches are considered : managing the patient's breath-hold, which is referred to as respiratory control technology as mentioned earlier ; and free breath-gating, which monitors the patient's free breathing in real time and controls the radiation beam ON/OFF based on the patient's respiratory movement. The radiation beam ON/OFF is based on predetermined standards or thresholds to ensure that radiation treatment can accurately target the tumor and minimize the radiation dose to surrounding normal tissues.

When developing a gating strategy, selecting a "gating window" or "threshold" is crucial, requiring a trade-off between achieving complete target coverage with the necessary treatment margin and overall treatment time, as reducing the margin will increase the overall treatment time [172]. There are mainly two types of gating thresholds : phase-based gating and amplitude-based gating. In phase-based gating, the radiation beam is turned ON when the calculated respiratory cycle enters a predetermined phase ; while in amplitude-based gating, the radiation beam is turned ON when the respiratory cycle reaches a predetermined displacement position. In most cases, the gating window is preferably selected at the end of expiration in the respiratory cycle because this is where the tumor is most stable during respiration, and airway volume may influence doses to organs at risk during inspiration [48]. Figure 1.6 shows the basic process and principle of the gating scheme. By monitoring tumor motion in real time and setting gating thresholds to selectively irradiate, the PTV margin is reduced to decrease the OAR dose.

One of the most widely used breath-gating systems is the Real-time Position Management (RPM) system. Taking this device as an example, we will introduce its preparation, CT scan acquisition, and treatment delivery stages in detail. As shown in figure 1.7, the RPM system tracks the patient's respiratory cycle by placing a reflective plastic box on the patient's abdomen surface. This box must always be installed in the same position, typically between the sternum and umbilicus, as this is usually the external region with maximum respiratory movement [121][155][135]. The reflector reflects infrared light emitted by an infrared illuminator onto a charge-coupled device (CCD), which is fixed relative to the patient's position and connected to a computer that is connected to a linear accelerator. The respiratory movement of the reflector will be analyzed in real time by software

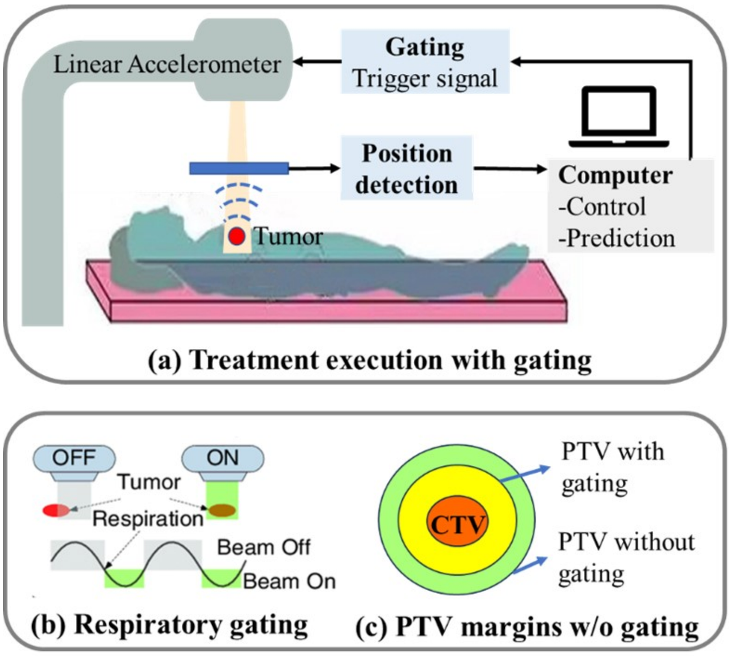

FIGURE 1.6 – Gating Scheme for Respiratory Motion Compensation. (a) Flowchart of gating scheme, with real-time monitoring and prediction of tumor motion caused by respiration ; (b) Selective irradiation when the tumor enters a smaller target area ; (c)PTV margin w/o gating.

that controls the trigger of the accelerator and controls the ON/OFF of the radiation beam based on pre-defined gating windows. Therefore, radiation beam transmission will be interrupted between each breath, and the total treatment dose will be delivered in several smaller fractions. Additionally, the RPM system can also track the patient's respiratory cycle during CT scanning and select pre-defined windows (prospective mode) or perform retrospective reconstruction of respiratory phases (retrospective mode or 4D-CT) [135][72].

The preparation work for treatment using the RPM respiratory gating device, such as patient fixation and isocenter selection, is similar to that of conformal radiotherapy (CRT) and does not require prior training. Although visual and/or audio guidance may improve reproducibility of respiratory patterns [47][23][24]. As the system is based on the patient's free breathing, there is no need for special attention to skin markers. Unlike breath-holding techniques, respiratory gating during free breathing requires specific adaptation of the equipment during image acquisition. A specific software interface should be provided for communication with an external system responsible for acquiring and analyzing respiratory signals (such as the RPM external box or belt). Whether the

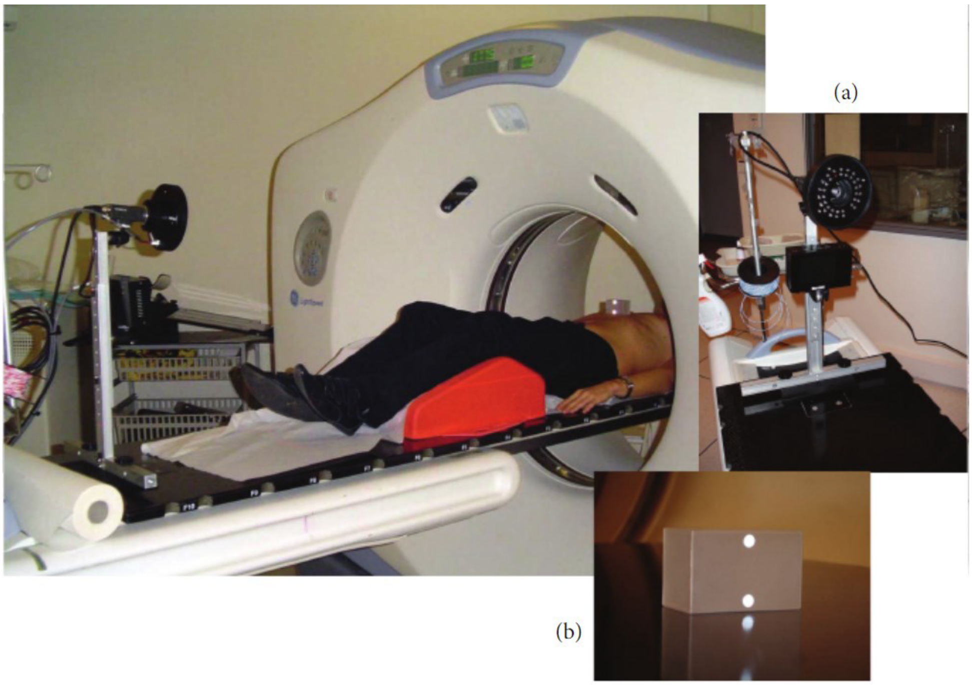

FIGURE 1.7 – Varian's RPM system. An infrared camera (a) illuminates a marker with two reflectors (b) placed on the patient's abdomen.

mode chosen is retrospective or prospective, the external system records the exact time of image acquisition, which allows for reconstruction of specific respiratory phases into full three-dimensional (3D) CT scans in the case of 4DCT [155][135][23][24][42].

In respiratory gated radiotherapy, the free breathing technique requires dealing with multiple short radiation exposures compared to breath-holding techniques, especially when combined with intensity-modulated radiation therapy (IMRT)[32][73]. First, it is necessary to ensure that the linear accelerator can switch between beam ON and OFF quickly and maintain stable projection rates, energy, and uniformity. Second, treatment delivery must be done under the same conditions as its preparation to ensure consistency. Additionally, marking the position of the RPM box on the patient's skin may seem simple, but it must be ensured that the patient's accessories or clothing do not hinder the movement of the external device [156]. To ensure treatment quality, it is also necessary to ensure there is no phase shift during treatment delivery, which can lead to inconsistent target location with respiratory monitoring [132]. These steps are key factors ensuring the effectiveness and safety of respiratory gated radiotherapy.

The technology of respiration gating relies on information from the respiratory cycle (also known as the"gating signal") to control radiation transmission. Non-invasive respiratory movement substitutes are commonly used clinically. In order to ensure the accuracy and reproducibility of the treatment, it is necessary to deeply understand the relationship between tumor motion and corresponding respiratory motion surrogates, and this relationship should be reproducible over time [28][62]. In most gating techniques, the tumor location is inferred from external surrogate respiratory signals, such as lung volume or skin motion. When Mageras et al. [104] performed gating radiotherapy on six lung cancer patients, they placed respiratory motion substitutes between the abdominal muscle tip and the umbilical region based on the minimum amplitude observed, which was 5 millimeters. Patients were subjected to a fluoroscopy examination for about one minute while breathing normally, and five of them were then instructed to inhale and exhale according to audio instructions.

Their report states that in most cases, the external respiration motion surrogate is able to accurately predict internal respiration motion. Research findings from Dick et al. [31] and Ionascu et al. [65] suggest a strong correlation between the liver or inferior lung lobe tumor and diaphragmatic muscle motion in the upper and lower direction. However, Feng et al. [40] found that there was little correlation between the location of pancreatic cancer and the external movements of the abdominal wall and diaphragm. Therefore, the correlation and reproducibility between tumor motion and external respiration substitutes are limited by tumor location and placement of substitutes. Keall et al. [73] clearly stated that respiratory motion surrogates should be considered for determining the consistency of the phase of respiratory motion, rather than predicting the absolute location of the tumor. Therefore, displacement correlation is not the primary concern. For tumors in certain locations, the short-term correlation between external surrogates and internal target locations may be high ; However, due to the transient changes in breathing and waveform drift, this correlation may be unstable during long-term treatment sessions [24].

1.2.4 Real-time Tumor-Tracking

Real-time Tumor-Tracking Radiotherapy (RTRT) technology is another form of motion management that allows patients to breathe freely while compensating for respiration-induced motion without patient intervention. RTRT includes two main aspects : real-time positioning of the constantly moving tumor and real-time adjustment of the radiation beam to adapt to its location. Compared to gating methods, tumor tracking technology may have additional advantages, such as higher delivery efficiency and less residual target motion. These factors may be particularly important in the treatment of thoracic and abdominal tumors that require the delivery of large doses during a single relatively long treatment session. It is crucial to emphasize that true real-time beam adaptation cannot be achieved without accurate real-time localization of the tumor in three-dimensional space [48].

Synchrony ™ is a RTRT system integrated to CyberKnife ® (Accuray Inc., Sunnyvale, CA), which uses external markers in conjunction with diagnostic x-ray imaging to compensate for respiratory motion, to emphasize the synchronized delivery of the radiation beam with respiratory cycle [139][144]. Figure 1.8 depicts the basic components of the CyberKnife with Synchrony (CKS). The CKS works differently for radiotherapy on thoracic and abdominal mobile organs compared to the head and neck region. In the head and neck region, due to the relative static nature of the organs, the real-time X-ray tracking system acquires image information every 10 seconds. However, this interval is too long for organs such as the lungs, pancreas, and liver, which are constantly in motion with respiration and heartbeat. To avoid overdosing the patient and overheating the diagnostic X-ray transmitter, the interval cannot be too short or continuous. To achieve real-time tracking of these moving organs, CyberKnife has introduced an infrared tracking system based on the X-ray image tracking system, which combines the two to achieve real-time tracking of the moving organs.

For thoracic and abdominal organs, since there is no fixed positional relationship between them and the bony landmarks of the body, spherical or cylindrical high atomic number (high-Z) metal fiducial markers (internal markers) (as shown in figure 1.9) is first implanted in or around the tumour tissue, which should remain relatively fixed in position with the tumour and serve as a detection marker for the X-ray tracking system [142][150]. In addition, three optical markers (external markers) (as shown in figure 1.10) that can emit infrared rays are pasted and fixed on the skin of the patient's chest and abdomen, and the infrared camera receives the information of the change in the position of these diodes and transmits it to the central processing system, and the infrared information receiving process is continuous at a frequency of 25-40 Hz. Under the condition of calm breathing, a correlation model that establishes a relationship between the external breathing signal and the motion of internal markers offers the tumour position in real time specific to that patient. The correlation model is built just before the start of each treatment fraction. It is updated during the fraction by taking, every 1 to 6 min, an X-ray image pair and is rebuilt if necessary. In this way, during the treatment process, when the patient maintains calm breathing, the robotic arm can always follow the movement of the tumour tissue according to the information received by the continuous infrared tracking system, thus real-time tracking irradiation can be achieved. At this time, the X-ray tracking system is off. When the movement of the target area exceeds the range of infrared tracking adjustment due to the patient's deep breathing and other actions, the infrared tracking system will order the linear accelerator to stop irradiation, and at the same time, start the X-ray detection system to automatically reposition the target area, and then start irradiation after confirmation. After confirming, the irradiation will start again. The whole treatment process will be completed by repeating this process.

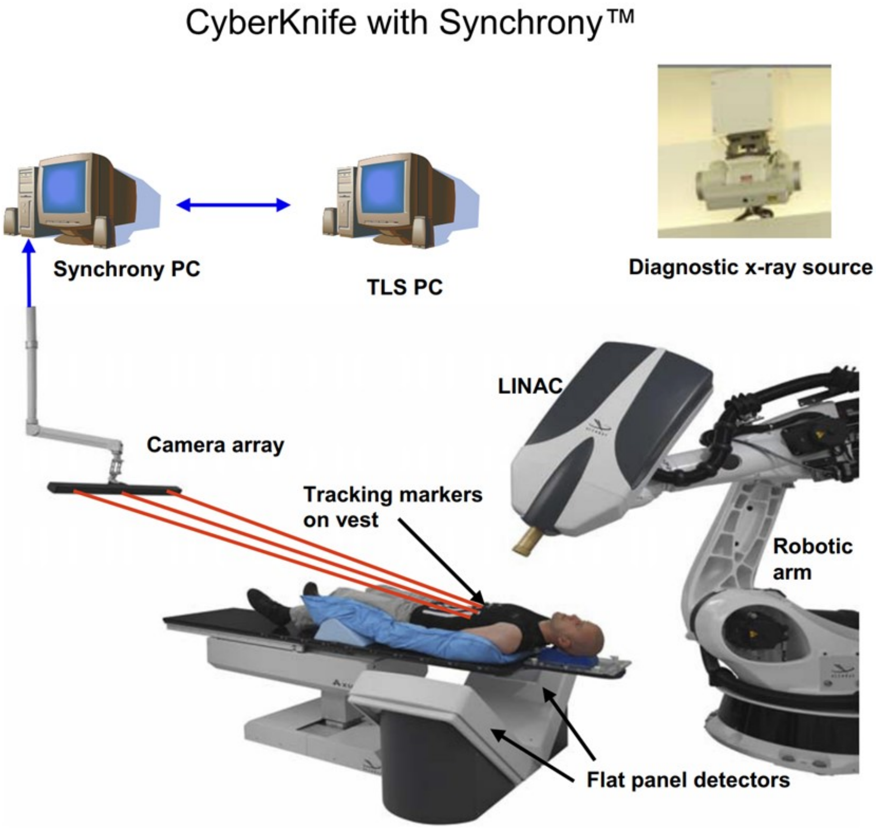

Figure 1.8 – Main components of the CyberKnife Robotic Radiosurgery System with the Synchrony Respiratory Tracking System are : (1) compact 6-MV X-band LINAC mounted to robotic arm ; (2) two orthogonal flat-panel x-ray detectors positioned perpendicular to diagnostic x-ray sources mounted to ceiling ; (3) Synchrony tracking vest with LED markers attached ; (4) camera array that holds 3 CCD cameras ; (5) Synchrony and Target Locating Computers. Image used with permission from Accuray Incorporated.

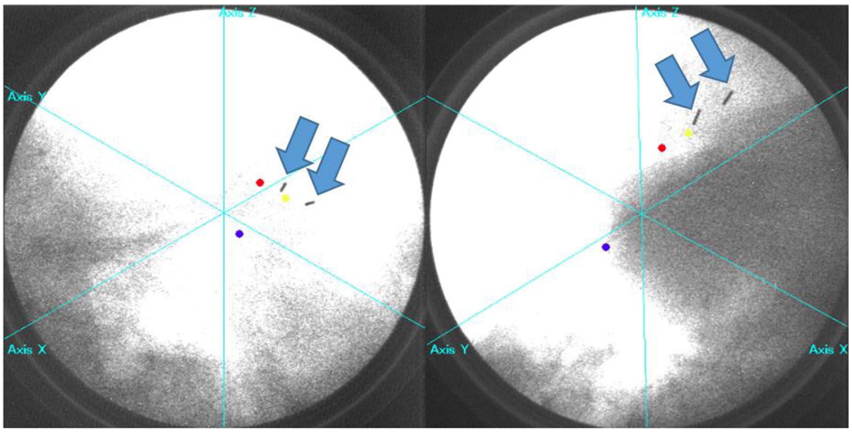

FIGURE 1.9 – Real-time tumor tracking radiotherapy console window displaying fluoroscopic images in two directions. Two spiral reference markers (shown by the arrow) were implanted in this patient.

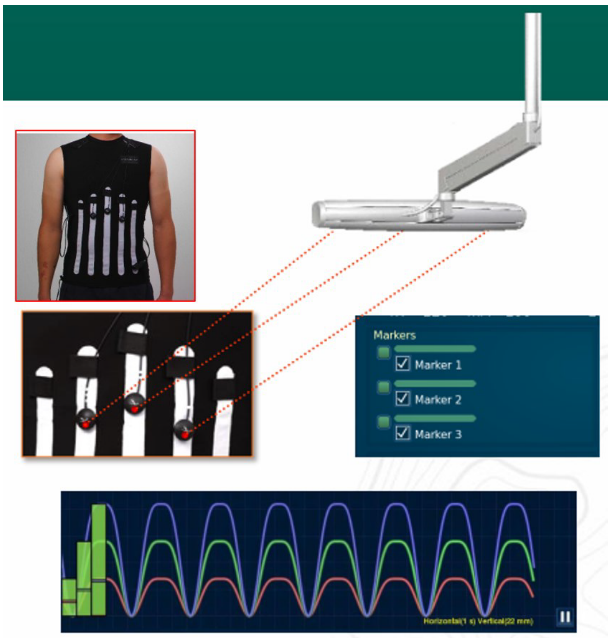

FIGURE 1.10 – Synchrony uses three optical markers to record the external breathing signal in real time. Synchrony camera array has three 1-dimensional CCD cameras (1, 2, 3), which are capable of determining the positions of LED markers attached to the patient's vest at a rate of 25 to 40 Hz.

The effectiveness of the RTRT system is influenced by multiple factors, including the system's identification time lag for the position of implanted fiducial markers, otherwise known as the delay period, as well as beam shaping speed and linear accelerator beam response time. The beam cannot be positioned instantaneously. Data processing, communication to the robotic controller, and the inertia of the robotic manipulator and the linear accelerator causes a time delay of 192.5 ms in their version of the system [63]. The delay period is one of the important factors, and if the delay period reaches 200 milliseconds, it may introduce significant dosimetric errors. Especially when using tumor tracking and prediction methods, some prediction algorithms do not consider the system's delay, which can lead to the system lagging behind the prediction of tumor position in practical situations, potentially leading to inaccuracies in radiation therapy [171]. Of course, there are also prediction algorithms that take the system's delay into account, which can more accurately quantify the geometric error of tumor position. These algorithms are able to better coordinate the system's delay and improve treatment accuracy [136][144].

In addition, the RTRT system relies on multiple fiducial markers being implanted within the tumor. The process of implanting these markers is sometimes likened to transthoracic needle biopsy for pulmonary nodules, which may result in up to 38% of patients requiring drainage for pneumothorax issues [178][65]. However, some viewpoints suggest that although implanting these tracking markers may cause some adverse events, it is worthwhile due to the increased treatment accuracy exceeding the potential morbidity [88]. In addition, the position of the markers may migrate, especially as the radiotherapy progresses and may be exacerbated by tumor shrinkage or changes in morphology. Although there have been reports of certain fiducial marker positions remaining relatively stable over time [154].

Among the disadvantages of implanted fiducial markers is the requirement for using ionizing radiation imaging equipment (such as kV or MV CT, or fluoroscopy) to view them. For example, 4DCT and other techniques are increasingly being used to correlate respiratory motion with CT scanning and assist in planning motion management treatment. This involves reconstructing multiple CT series images synchronized with the patient's respiratory waveform, typically at different stages of inspiration and expiration [52]. However, the radiation dose generated by these methods can accumulate to clinically significant levels, especially to the patient's skin dose [88][186]. As an example, 4DCT has been reported to have radiation doses as high as 4 times that of spiral CT scanning [113]. It should be noted that the Calypso system (Calypso Medical Technologies, Seattle, USA) is one of the few commercial devices that is unique in that it does not rely on ionizing radiation to generate images. Instead, it uses 4D electromagnetic array technology to monitor and track the position of implanted electromagnetic sensors in real-time. Although this system was initially mainly applied for prostate motion management [182][84][93], recent research has begun to explore its potential application in gated radiotherapy [157][158][118].

1.2.5 Optical surface guided radiotherapy technique

The Optical Surface Monitoring System (OSMS), also known as Surface Guided Radiation Therapy (SGRT), is a non-invasive, radiation-free IGRT technique. It utilizes the principles of three-dimensional surface imaging to acquire a three-dimensional point cloud of the patient's surface. This point cloud is then registered with a reference 3D image using elastic or rigid algorithms. The calculated deviations are employed to correct the patient's positioning, guiding the radiation therapy.

The primary advantage of SGRT lies in its non-ionizing nature, allowing its use throughout the entire radiation therapy process. Although initially motivated to replace lasers and skin markings for patient positioning [69], SGRT has found limited clinical applications. Its potential value has not been widely recognized in radiation therapy. SGRT has the capability to gather extensive data on position, surface, and respiratory status. This information can be utilized to predict patient conditions, guiding patient positioning, providing real-time imaging, monitoring respiratory motion, reducing overall treatment time, lowering doses to surrounding normal tissues, verifying the accuracy of generated displacements, or implementing breath-hold techniques to achieve respiratory-correlated treatment.

Generally, as illustrated in figure 1.11, surface-guided radiation therapy systems combine a projector and one or more cameras to real-time record the patient's three-dimensional surface. After registering with a reference image (typically centered), the system calculates offsets in the translational and rotational directions, providing information on the patient's positioning. Examples of such devices in the market include AlignRT™ (Vision, UK), Varian IDENTIFY™ (Palo Alto, CA, USA), and Sentinel™/Catalyst HD Monitoring and Position Verification System (C-RAD, Sweden).

One promising application of SGRT is in gated treatment, especially for tumors near the skin surface (e.g., breast cancer) using Deep Inspiration Breath-Hold (DIBH) techniques (see 1.2.2). DIBH requires patients to inhale to a specific threshold during each treatment, followed by breath-hold for positioning and treatment (as shown in figure 1.12).

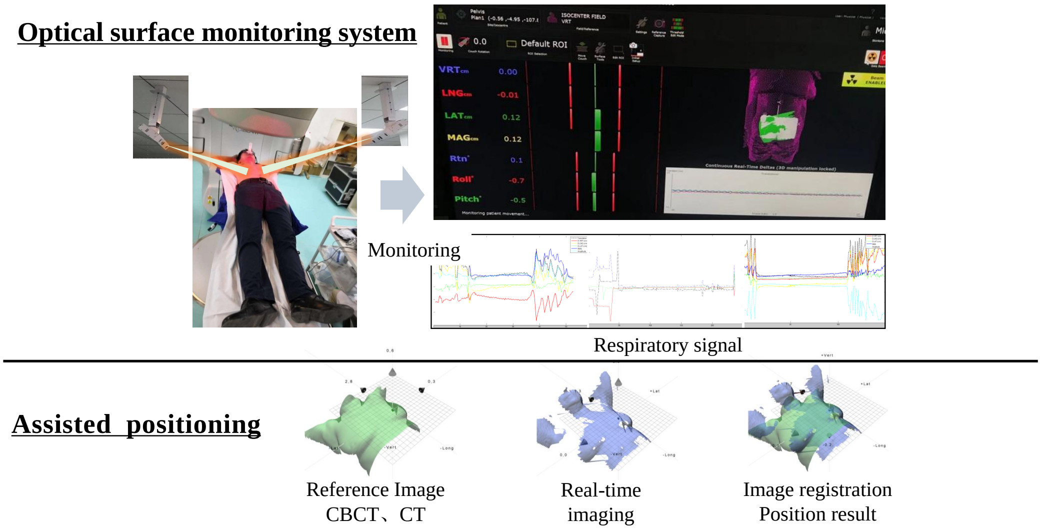

FIGURE 1.11 – The OSMS utilizes the principles of three-dimensional surface imaging to capture a patient's three-dimensional surface point cloud. It registers this point cloud with a reference 3D image using elastic or rigid algorithms, calculating deviations to correct the patient's positioning and guide radiation therapy.

When using optical surface systems for positioning, personalized gating window settings can be specified for each patient, ensuring sufficient inhalation while maintaining high comfort and repeatability. Patients can wear video training glasses, providing real-time feedback on inhalation volume and the position of the gating window, actively maintaining an accurate and stable breath-hold.

Throughout the DIBH treatment process guided by optical surface technology, respiratory motion management is crucial. Patients need to adopt diaphragmatic breathing, and practicing the technique at home before treatment is essential for better treatment outcomes. Studies indicate that pre-training and practicing DIBH methods can further reduce cardiac and pulmonary doses for breast cancer patients [76][70]. Additionally, effective communication between staff and patients during treatment is crucial to alleviate psychological stress caused by factors such as movement of the treatment bed, rotation of the gantry, extension of the imaging arm, and noise from air conditioning and dehumidifiers. Currently, the combination of optical surface guidance technology with DIBH for left-sided breast cancer irradiation has been widely adopted in multiple institutions, demonstrating significant reductions in doses to critical organs. It is recommended for

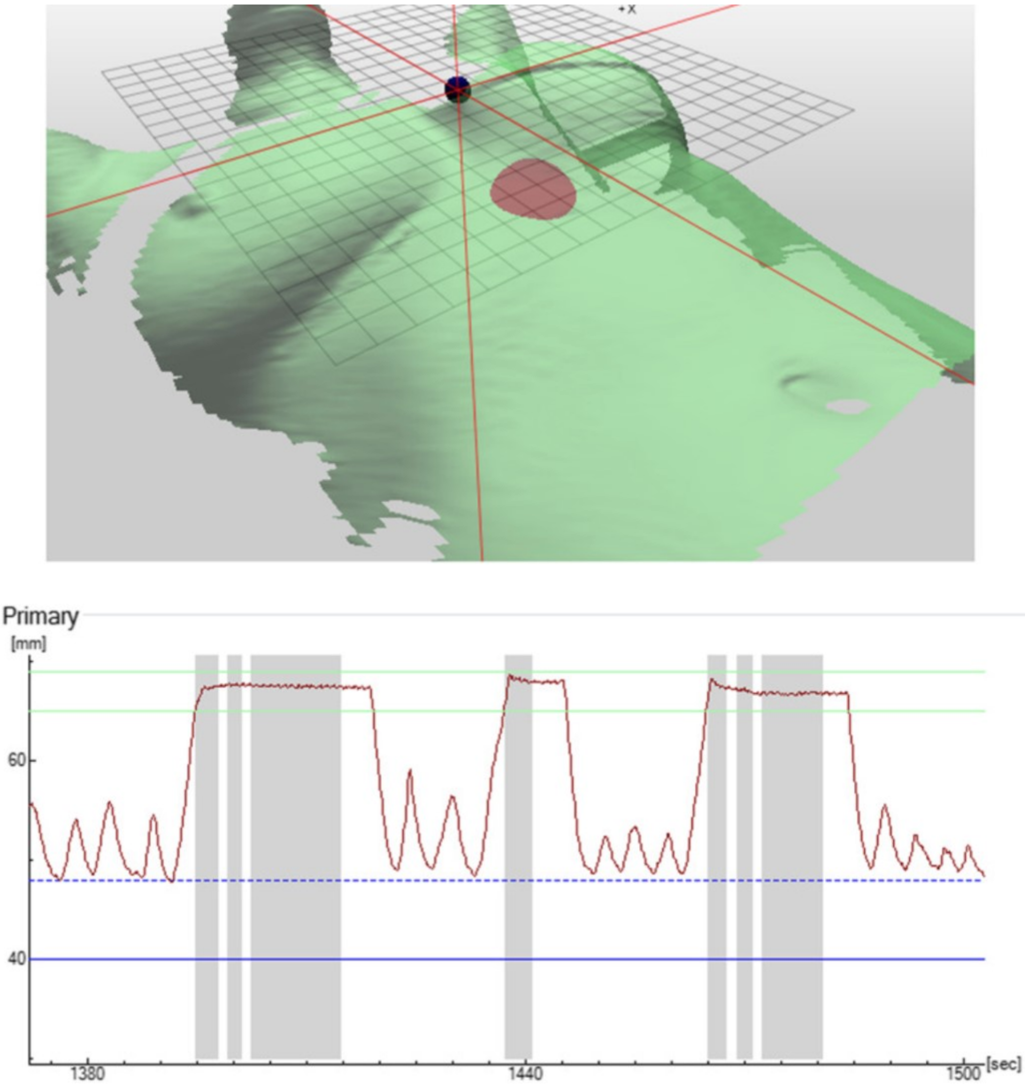

FIGURE 1.12 – DIBH Monitoring. Top Image : Monitoring a respiratory point (in red) on the patient's body surface (in green). Bottom : Respiratory curve with three breath-hold phases, covering seven individual beams (indicated by gray bars). Image provided by LMU University Hospital Munich, Germany.[**freislederer2020recent**]

all left-sided breast cancer patients undergoing radiation therapy [141][41][128]. However, caution should be exercised when using surface imaging for deeper tumors where there is no direct correlation between surface deviations and target tumor movement [124].

1.3 MRI-guided adaptive radiotherapy

In traditional radiotherapy, whether introducing concepts like 4D-CT and Internal Target Volume (ITV) or employing respiratory control techniques (ABC, DIBH), respiratory gating techniques, or tumor tracking, the goal is to address the adverse effects of tumor motion on treatment. However, the changes in the target area and surrounding organs during the treatment process necessitate further adaptation through the use of Adaptive Radiation Therapy (ART). With the emergence of onboard CT/CBCT with 4D imaging capabilities or real-time monitoring using MR-guided devices, online ART has made significant progress in the clinical treatment of chest and upper abdominal tumors such as lung and liver cancers. However, current research has mainly focused on pre-fractionation repositioning scans, delineation of target areas and organs at risk, and the redesigning or modification of ART plans. There is still a lack of comprehensive research on real-time adaptive strategies for the motion of thoracoabdominal tumors during fractionated treatments.

Magnetic Resonance Guided Radiation Therapy (MRgRT) has emerged as a focal point in the field of radiation therapy in recent years. With the clinical deployment of MRI-guided linear accelerators (MRI-Linac), there is widespread anticipation that MRgRT technology will usher in transformative changes in the realm of radiation therapy. In contrast to traditional X-ray-based Image-Guided Radiation Therapy (IGRT) techniques, MRI does not subject patients to additional imaging doses. Unlike CT, CBCT, and MV-CT, where daily imaging doses must be factored into the patient's total radiation dose, MRI circumvents this issue. Furthermore, MRI addresses the challenge of poor soft tissue resolution in kV X-ray imaging, offering outstanding soft tissue resolution and real-time imaging capabilities. It eliminates the need for surface or internal markers to substitute for tumor motion, thereby avoiding issues related to establishing marker-tumor correlations. This allows for direct real-time monitoring of moving target areas and opens up possibilities for real-time tracking during treatment.

1.3.1 Basic Structure and Treatment Workflow of MRI-Linac

Existing MRI-Linac systems can be broadly categorized into two types : the 0.35T MRI system combined with a cobalt-60 source or linear accelerator, exemplified by ViewRay, and the 1.5T MRI system combined with a linear accelerator, represented by Elekta Unity.

ViewRay, as the pioneering company in the development of MR-guided radiation therapy (MRgRT) in the United States, introduced the ViewRay MRIdian 60Co, the first commercially available integrated MRgRT system fusing MRI with radiation therapy equipment. It received FDA approval in 2012 and has been in clinical use [111][81]. The system comprises a 0.35T MRI scanning system and three 60Co sources spaced at 120° intervals. It features a maximum field of view scanning range of 27cm, extendable up to 50cm, with a source-axis distance of 105cm and a dose rate of up to 550 cGy/min. This system allows real-time MR imaging tracking during the radiation therapy process. Recently, ViewRay has designed the MRIdian Linac system, integrating a 0.345T dual-ring wide-bore superconducting magnet with a 6 MV FFF (flattening filter-free) linear accelerator. This system has a source-axis distance of 90cm and a dose rate of 600 cGy/min. Equipped with 69 pairs of dual-layer dual-focusing MLC (34 pairs in the upper layer and 35 pairs in the lower layer), with a projection width of 0.415cm at the isocenter, the system's minimum field size is 0.2×0.4cm, and the maximum field size is expanded to 27.4×24.1cm, further expanding possibilities in the medical field [46].

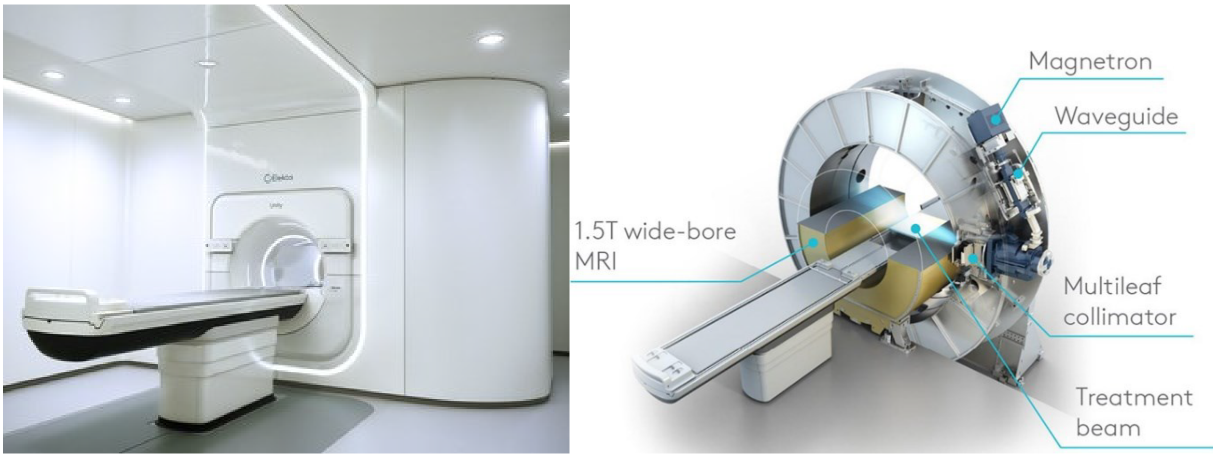

FIGURE 1.13 – Elekta Unity : The first MRI-Linac system to provide high-field MRI.

A prominent representative of MR-Linac is the "Atlantic System" developed through collaboration between Utrecht University in the Netherlands, Elekta, and Philips. Commonly known as the Utrecht model [131], this system, illustrated in Figure 1.12, integrates a 7MV FFF X-ray accelerator system from Elekta and a 1.5T MRI system from Philips Healthcare. Both the X-ray and MRI systems have been modified to ensure simultaneous and interference-free operation. The designers ingeniously mounted the accelerator's head on a 4-meter diameter, shielded slip ring gantry, rotating at a speed of six revolutions per minute, meeting the requirements for rotational intensity-modulated radiation therapy. A beam stopper is placed on the other side of the accelerator to prevent the primary radiation beam from directly hitting the walls, ceiling, and floor of the shielding room, ensuring radiation safety. It is essential to note that this system utilizes Monte Carlo simulation algorithms for field optimization, dose calculations, and dose distribution reconstruction inside the patient [79]. This system represents the first MR-Linac system to provide high-field MRI, with image quality comparable to MRI scanners used in diagnostic imaging [176]. Introduced at the 36th European Society for Radiotherapy and Oncology (ESTRO) meeting, it was officially named "Elekta Unity" [82].

Based on the specific needs of different medical institutions and patients, as well as the differences in MRgRT plans and treatment goals, the design of adaptive clinical processes may vary. The clinical workflow for Elekta Unity is divided into offline and online processes. The offline functionality allows physicians to prepare a plan template that complies with prescription requirements, referred to as a reference plan, in advance. This reference plan conveys the physician's intent to the clinical team involved in treatment delivery. This not only simplifies online decision-making but also facilitates the smooth progress of the entire adaptive workflow. The online process involves three sequential steps for each treatment fraction : Scan-Plan-Treat. The first step involves positioning the patient and performing a three-dimensional magnetic resonance localization image scan. In the second step, registration is completed between the magnetic resonance localization image and the simulated localization image on the Monaco planning system. The treatment tumor target and OAR positions are determined based on the online images, and an adaptive plan for the current treatment is formulated on the basis of the reference plan. Two adaptive modes, "Positional Correction" or "Shape Correction," can be selected. The third step involves executing the adaptive plan on the MR radiation therapy system. During treatment, three 2D cine-MRI planes can be used for real-time monitoring of the position and movement of the tumor and OAR, ensuring that there is no deviation of the target lesion during treatment.

Elekta Unity possesses unique advantages that can overcome many challenges currently limiting the continuous development of Image-Guided Radiation Therapy (IGRT). In comparison to CBCT images in IGRT, the high-field strength MR-Linac not only eliminates additional imaging doses, making in-room and real-time imaging more convenient, but also achieves significant progress in enhancing MRI soft tissue contrast and maintaining relatively low levels of artifacts[22][86][167][8][179][183]. Elekta Unity, with its high field strength, enables visualization of soft tissues according to diagnostic standards during treatment. It provides opportunities for direct motion monitoring and treatment adjustments based on daily real-time anatomy and biological information[49]. Elekta Unity reduces treatment uncertainties associated with existing radiotherapy techniques, achieving more precise Clinical Target Volume (CTV) coverage and better Organ at Risk (OAR) protection. This is expected to lower treatment toxicity and improve clinical efficacy [168].

During radiation therapy, tumors may move due to factors like breathing, heartbeat, and intestinal motion. Elekta Unity can monitor and track such movements in real-time, allowing for timely adjustments to the treatment plan. This capability aims to truly achieve the concept of "visible treated" [109][130]. Therefore, MRI-Linac is not only a new Image-Guided Radiation Therapy machine but also a revolutionary radiation therapy technology. It realizes genuine real-time MRI-guided radiation therapy, providing highly personalized treatment plans for each patient.

1.3.2 Clinical Research Status of MRI-Linac in Respiratory Motion Management

Currently, while MRI-Linac systems can adjust the target area and treatment plans between fractions to achieve precise radiation therapy, they still face challenges in addressing tumor and Organ at Risk (OAR) position changes caused by factors like respiratory motion during the radiation therapy process. Respiratory motion remains a primary concern for adaptive radiation therapy at this stage.

One of the most noteworthy features of MR-guided Radiation Therapy (MRgRT) is its radiation-free real-time imaging capability. This exceptional feature provides outstanding visualization of internal organs, enabling clinicians to monitor and respond to the movement of internal organs in real-time during the treatment process. This not only reduces off-target probabilities but also theoretically increases the target area dose with fewer radiation sessions, further protecting normal tissues. Elekta Unity, with its high-resolution soft tissue imaging and real-time adaptive motion capabilities, has the potential to revolutionize certain adaptive radiation therapy approaches.

The gating technology stands out as the preferred approach for MRgRT systems to adapt to real-time tumor motion. This technology involves capturing motion images (2D Cine-MR) continuously in a single sagittal plane during treatment, ensuring high temporal resolution [111]. This allows for precise tracking of the target area's position. Treatment is only initiated when the tumor reaches a specific position, ensuring both accuracy and safety. A research team from the Amsterdam University Medical Center employed the ViewRay MRIdian system in single-fractionated motion-gated lung stereotactic ablative radiotherapy for 10 patients. The results were impressive, showcasing MRI's capability in real-time tumor tracking.

However, a current limitation of the ViewRay MRIdian system is its reliance solely on the sagittal plane for real-time monitoring of tumors and OARs. Although most respiratory-related motion occurs primarily in the craniocaudal direction, organ deformation and other complex movements can mean that some targets may not follow a straightforward trajectory. This necessitates a careful evaluation of existing clinical systems and the consideration of incorporating ITV based on additional motion research results, depending on the circumstances[51].

Another consideration with gated radiotherapy using the MRIdian system is the significant increase in overall treatment time. This is due to the fact that irradiation is only performed during a specific portion of the entire motion cycle. For instance, the average time for single-fractionated treatment of lung cancer is approximately two hours, which is more than double the standard treatment time.

Another drawback of MRIdian system for gated therapy is a noticeable increase in the overall treatment time. This is due to irradiation being conducted during a part of the entire motion cycle, leading to a treatment time of over two hours on average for a single-segment treatment of lung cancer – more than doubling the treatment duration.

At the beginning of 2023, Elekta Unity MR-Linac's Comprehensive Motion Management (CMM) received 510(k) certification from the US FDA, introducing True Tracking and automatic gating capabilities, marking a significant advancement in radiation therapy. Elekta Unity became the first in the United States to enable automatic calculation and correction of continuous tumor motion, enabling clinicians to treat patients more precisely, especially when dealing with moving organs.

CMM supports four workflows, allowing users to manage the treatment of targets with periodic respiratory motion or random motion. A patient with pancreatic cancer was treated at the University Medical Center Utrecht (UMC) using Elekta Unity's CMM, which continuously calculates tumor motion and automatically corrects it. According to Dr. Martijn Intven, a radiation oncologist at UMC Utrecht, the first treatment using CMM proceeded smoothly. As the beam automatically turns on during the patient's exhalation phase, the patient doesn't need to hold their breath for a prolonged period, and the overall treatment time does not significantly increase. This breaks the traditional gating paradigm where treatment time would be increased.

Currently, the CMM system remains in the early stages of clinical research and has yet to be widely integrated into Elekta Unity systems across institutions. Consequently, a comprehensive evaluation of its tumor tracking accuracy and motion prediction precision in real-world clinical settings remains elusive. Despite theoretical advantages, the practical performance and feasibility of the CMM system require further validation through broader clinical trials.

An alternative solution that holds promising potential is MLC tracking. This technology offers the benefit of free breathing during treatment without prolonged beam-off time (100% duty cycle), which is particularly crucial for patients with significant tumor motion. Although MLC tracking and VMAT are not yet incorporated into current clinical MR-linac versions, Prescilla Uijtewaal et al. [168] have demonstrated the technical feasibility of implementing VMAT + MLC tracking on Elekta Unity. Notably, the delay from Elekta Unity MLC is minimal at approximately 20ms, yet further development is necessary to seamlessly integrate clinical workflows and hardware devices. Additionally, clinical treatment planning systems must offer full support for VMAT on Elekta Unity, particularly for daily plan adjustments.

1.4 Challenges

To improve the precision of treatment in thoracoabdominal tumor, dynamic dose delivery adjustments must be made based on real-time observations of respiratory motion. However, from a technical perspective, achieving safe and reliable real-time adaptive MRgRT through CMM still presents some scientific challenges that we here delve into in detail :

1. Fast and Accurate Tumor Tracking Algorithm : Rapid detection of tumor shape and position on Cine-MRI remains a major bottleneck, as current clinical practices, such as manual contouring by experts like radiation oncologists, are time-consuming

and negate the advantage of Unity's rapid MR imaging during the radiotherapy process. Template matching (TM) has been proven effective in tumor tracking and applied in the MRIdian gating treatment[149]. However, we have found that this method has significant computational time issues when dealing with large images or complex templates, thus deteriorating the overall delay. Therefore, a fast and reliable algorithm for automatic tumor contouring or tumor tracking is one of the necessary conditions for achieving precise CMM.

2. Prediction of Gating Signals Based on small dataset : There is a system latency between detecting target motion and delivering the dose to the target, during which the tumor might have moved, potentially causing misalignment and inaccurate radiation delivery. Studies indicate that Elekta Unity can control the overall system latency within 0.5 seconds [86], including processes like image acquisition, target motion trajectory extraction, and beam-on trigger. To compensate for Unity's system latency, real-time prediction of tumor and critical internal structure positions is necessary, posing a challenge in the accuracy of tumor motion prediction algorithms.

   In recent years, Recurrent Neural Networks (RNN) and their derivative versions demonstrate strong adaptability and nonlinear modeling capabilities in predicting patients' respiratory motion [7][110]. Recurrent Neural Networks (RNN) and their derivative versions demonstrate strong adaptability and nonlinear modeling capabilities in predicting patients' respiratory motion [92][99][177][190]. However, like other deep network models, training models require a substantial amount of annotated tumor motion data, which is often challenging to obtain or costly on the Unity. Additionally, the significant variability in respiratory motion patterns between patients makes training a patient-specific RNN model highly challenging.

3. Prediction of Gating Signals Based on Low-Frequency Motion Data : Recent reviews suggest that linear methods show sufficient effectiveness in predicting respiratory signals in CyberKnife treatment[68]. However, due to differences in imaging modes, acquisition frequencies (30Hz vs. 5Hz), and system latency between X-ray-guided and MRI-guided treatments, applying X-ray-guided prediction methods directly to MRgRT may face challenges. Therefore, validation of predictors for motion trajectories of tumor and OARs obtained from 2D cine MRI data is crucial.

Obtaining accurate gating signals for MRgRT is challenging, primarily due to the following factors : 1) The sampling frequency of 2D cine-MRI is typically between 4-8Hz[49], while the accuracy of gating signals relies on high-frequency monitoring of respiratory motion. Constrained by the lower sampling frequency, gating signals may not capture subtle variations in respiratory motion. 2) Predicting gating signals usually requires fixing a prediction window to determine cross-timing. The prediction task is defined as 1) whether or not crossing will occur in the next X ms and 2) if yes, when. However, fixing the prediction window is typically a trade-off between the prediction accuracy (the shorter the higher) and enough action time to compensate for the overall system delay (late predictions might reduce gating efficiencies). 3) Even at a 5Hz sampling frequency, predictive errors in gating signals may still exist, with errors of up to 0.2 seconds (sampling time), potentially reducing the accuracy of CMM in MRgRT.

Therefore, addressing these challenges and improving the accuracy of gating signals to ensure effective compensation of respiratory motion during radiation therapy is a critical topic in MRgRT research and practice.

4. Evaluation of Comprehensive Errors in Tumor Tracking and Prediction, and Dosimetric Validation : Tumor tracking algorithms aim to accurately detect and track tumor positions in medical imaging, while tumor motion prediction algorithms predict future positions and trajectories based on the tracked tumor position. As these two tasks are typically independent, calculating the comprehensive errors generated by them is a challenging task. Hence, establishing an end-to-end gating system for real-time motion compensation during Unity treatment and assessing its reliability holds practical significance.

1.5 Thesis aims

This thesis aims to develop an end-to-end gating system for real-time motion compensation during the treatment of lung and liver cancer patients on the Elekta Unity. The system will continuously monitor and automatically locate the 3D spatial positions of the tumor while predicting its motion trajectory in advance in all three dimensions. Based on predefined gating rules, a unique gating signal will be generated to control the beam-on and beam-off during MRgRT, thereby compensating for the inaccuracies in dose delivery caused by respiratory motion.

The specific objectives outlined in this paper to address the challenges mentioned in

Section 1.4 are as follows :

1. Tumor tracking algorithm based on KCF : Construct the Unity database, achieve rapid and accurate tracking of tumors in 2D cine-MR, and extract the tumor's motion trajectory in three dimensions. Further details will be provided in Chapter 2.
2. Transfer C-NLSTM tumor motion prediction algorithm : Validate the reliability of deep learning methods for predicting tumor motion and address the issue of insufficient Unity training data affecting prediction accuracy. Further details will be provided in Chapter 3.
3. Real-time gating for breath motion compensation based on prediction : Validate the effectiveness of linear regression for predicting internal organ or tumor motion in 2D cine-MRI. Propose an online gating signal prediction scheme to obtain real-time gating signals for controlling beam switching to compensate for respiratory motion, thereby improving the accuracy of MRgRT for liver and lung cancer. Further details will be provided in Chapter 4.
4. Efficient personalized gating scheme based on orthogonal Cine-MRI : Establish an end-to-end gating system for real-time motion compensation during Unity treatment. This system should meet real-time speed requirements, generate accurate gating signals, and minimize the volume of the PTV expansion while maximizing the duty cycle. Further details will be provided in Chapter 5.

Chapitre 2

TARGET TRACKING ALGORITHM BASED ON KERNEL CORRELATION FILTER

2.1 Introduction

Accurate localization of the tumor during the radiotherapy process is a crucial aspect of the successful application of real-time motion compensation in lung cancer patients. This chapter will focus on introducing algorithms for tumor automatic localization or tracking, and propose an online solution optimized for tumor tracking.

For tumor tracking, researchers have developed various methods to track structures of interest in 2D Cine-MRI [146]. The widely used Scale-Invariant Feature Transform (SIFT) method allows for the extraction and robust matching of corresponding points between two images [100]. Among its numerous applications, SIFT is employed not only for assessing the geometric accuracy of deformable image registration [125] but also for tracking liver and lung tumors in Cine-MR images [126][145]. Additionally, Liu [94] and Mazur et al. [106] proposed a "dense" variant of this method, which relies on pixel-based matching rather than sparse feature matching. In the latter work, Dense SIFT was utilized to track targets within regions of interest in sagittal Cine-MRI series acquired by the MRIdian® system. While this method reportedly requires computation time per frame comparable to the image acquisition time (approximately 250 ms), achieving true real-time capability may be possible through algorithm optimization and parallelization.

Seregni et al. [145] utilized an offline method based on the SIFT algorithm to extract tumor motion features from Cine-MRI slices. Dhont et al. introduced the Tracking-Learning-Detection (TLD) framework into the MRgRT workflow, evaluating and optimizing the tracking performance of anatomical structures on 2D Cine-MR. Despite the challenges of significant tumor deformation and periodic disappearance, this study achieved sub-pixel-level tracking accuracy, ensuring an accuracy and recall rate of over 95%. Seregni et al. [16] validated a hybrid tracking approach combining optical flow registration techniques with optimization through similarity matching and motion field computed during the initialization phase to enhance speed. In their analyzed trajectories, 64.3% of tracking errors reached sub-pixel accuracy, but this optimization is applicable only when the object's appearance remains stable. Although similar accuracy was achieved, the authors noted that out-of-plane motion might increase tracking errors. Bourque et al. [1] proposed a particle filter-based optimization tracking algorithm for Cine-MR tracking, also achieving sub-pixel-level tracking errors. However, accuracy degradation may occur, especially when there is off-plane motion, and reference images must be acquired and outlined before each treatment, particularly when candidate images differ from the reference images.

Cerviño et al.'s study [20] suggests that relatively simple techniques, such as template matching (TM)and surrogate tracking, exhibit higher accuracy compared to Artificial Neural Networks (ANN). Similarly, Shi et al. [149] employed template matching based on standardized cross-correlation to locate lung tumors in 2D Cine-MRI. They achieved results comparable to the errors introduced by manual tumor identification but found it to be time-consuming when dealing with large images or complex templates. In contrast, Bolme et al [11] introduced correlation filters, particularly the classic Minimum Output Sum of Squares Error (MOSSE) algorithm, for object tracking. The MOSSE algorithm leverages Fourier transforms to reduce computational complexity and improve speed. However, its performance is constrained by its reliance on grayscale features in different contexts. To address this limitation, Henriques et al. [58] proposed the Kernelized Correlation Filter (KCF) algorithm, which intelligently handles limited training samples by exploiting a circulant matrix structure. The inclusion of Histogram of Oriented Gradients (HOG) features enhanced accuracy and robustness. Furthermore, the use of kernel functions and circulant matrix diagonalization significantly reduced the computational complexity of object tracking. However, the effectiveness of MOSSE and KCF algorithms in tumor tracking on 2D Cine-MRI remains to be validated.

To address the issues of tumor shape changes and computational efficiency mentioned above, this chapter proposed a tumor tracking workflow based on KCF, as illustrated in Figure 2.1. This workflow aims to achieve real-time and accurate tracking of lung and liver tumors in MRgRT using 2D Cine-MRI. The innovations and main contributions of this chapter are as follows :

1. We have constructed a Unity database, which includes 2D cine-MRI data from a total of 20 cancer patients, comprising 10 liver cancer patients and 10 lung cancer

patients. Experienced radiologists outlined the Gross Tumor Volume (GTV) and Organs at Risk (OAR), allowing for the extraction of the tumor trajectories in the SI, AP, and LR directions.

2. We assessed three tumor tracking algorithms (the TM, KCF, and MOSSE), taking into consideration geometric accuracy and computational efficiency.

3. When the tracker returns the tracking target (a fixed-size rectangular box), we proposed an optimization method for centroid calculation. This method further calculates the centroids of lung and liver tumors, improving the accuracy of tracking by reducing errors caused by changes in tumor shape when using fixed-size templates.

4. We pay particular attention to tumor tracking in the SI direction. By calculating the correlation between templates and subsequent frames on coronal and sagittal planes, we selected the slice with higher correlation (either coronal or sagittal) to determine the motion in the SI direction. This approach enhances the accuracy of tumor localization in the SI direction.

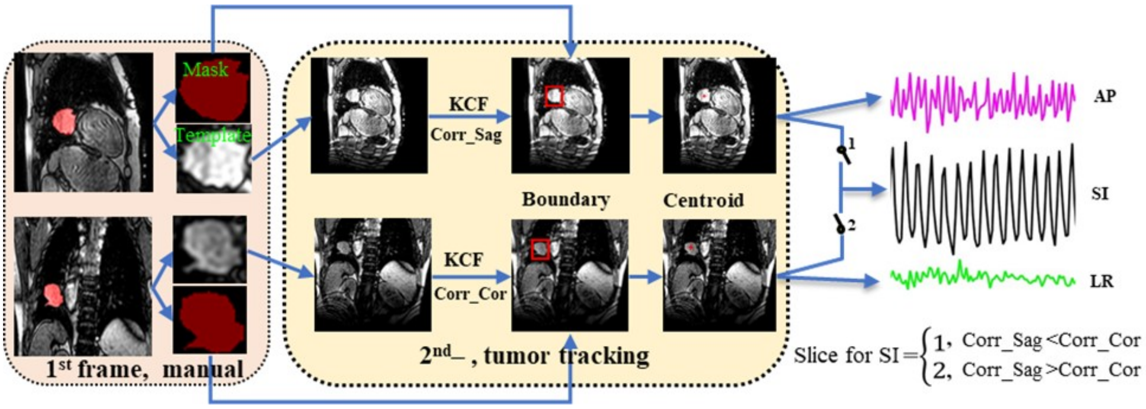

FIGURE 2.1 – KCF-based tumor tracking workflow proposed in this chapter.

2.2 Target tracking algorithms

Three correlation-based tracking algorithms are tested : TM in spatial domain, MOSSE in Fourier domain and the KCF also in Fourier domain without linear constraints.

2.2.1 Template Matching (TM)

TM is the process of sliding a template over the entire image and calculating the similarity between the template and the covered window in the image [149]. It involves a brute force search for a predefined template in a local region of the dynamic image by maximising an objective function to determine a good match. The objective function used in this study is the normalised cross-correlation, given by

$$\gamma(u,v) = \frac{\sum_{x=u+1}^{u+N_x}\sum_{y=v+1}^{v+N_y}(f(x,y)-\bar{f}_{u,v})(t(x-u,y-v)-\bar{t})}{\sqrt{\sum_{x=u+1}^{u+N_x}\sum_{y=v+1}^{v+N_y}(f(x,y)-\bar{f}_{u,v})^2\sum_{x=u+1}^{u+N_x}\sum_{y=v+1}^{v+N_y}(t(x-u,y-v)-\bar{t})^2}} \tag{2.1}$$

where $f(x,y)$ denotes the grayscale intensity value at the point (x,y) in the target image f of size $M_x \times M_y$, $x \in 1,...,M_x$, $y \in 1,...,M_y$, $t(x,y)$ denotes the grayscale intensity value at the point (x,y) in the template image t of size $N_x \times N_y$,$x \in 1,...,N_x$, $y \in 1,...,N_y$, and (u,v) is the shift of the template in the x and y directions, respectively. $\bar{f}_{u,v}$ denotes the mean value of $f(x,y)$ within the area of the template t when it is shifted to (u,v), $\bar{t}$ is the mean value of the template t.

The normalization ensures that $\gamma(u,v)$ is independent of changes in brightness or contrast of the image. These changes are related to the mean and standard deviation of the image intensity value. The maximization of $\gamma(u,v)$ determines the localization of the tumour given the fixed template by manual contouring.

2.2.2 Minimum Output Sum of Squared Error (MOSSE)

MOSSE was the first fast tracking algorithm to apply correlation filters to target tracking in the Fourier domain. A detailed description of the MOSSE formulation was given in [11]. Figure 2.2 shows its flowchart. The specific procedure in this experiment is as follows :

1. Target Template Creation : In the first frame, first select the target to be tracked and create a target template, typically a rectangular region containing the visual information of the target. For example, pixels in the red box on the first frame in Figure 2.2 is the target template.

2. Feature Extraction : Features are extracted from the target template. These features typically include pixel values, color histograms, gradient information, and more and are used to represent the target.

3. Correlation Filter : The MOSSE is then used as the Correlation Filter for producing

ASEF-like filters from fewer training images. The filter is learned from a set of training images f_i and training outputs g_i, the latter are 2D Gaussian functions ($\sigma = 2.0$) generated from ground truth locations of the target in training image f_i as the center. Training was performed in the Fourier domain to take advantage of the simple element-wise relationship between the input and the output as opposed to convolutions in the spatial domain. This process is used to compute the target's response map.

4. Target Location Determination : The location corresponding to the maximum value in the response map indicates the new position of the target. The target template is then updated to include the new set in the current frame.

5. Repeat Tracking : The above process was repeated to track the target in consecutive frames. In each frame, update the target template and compute the target's position.

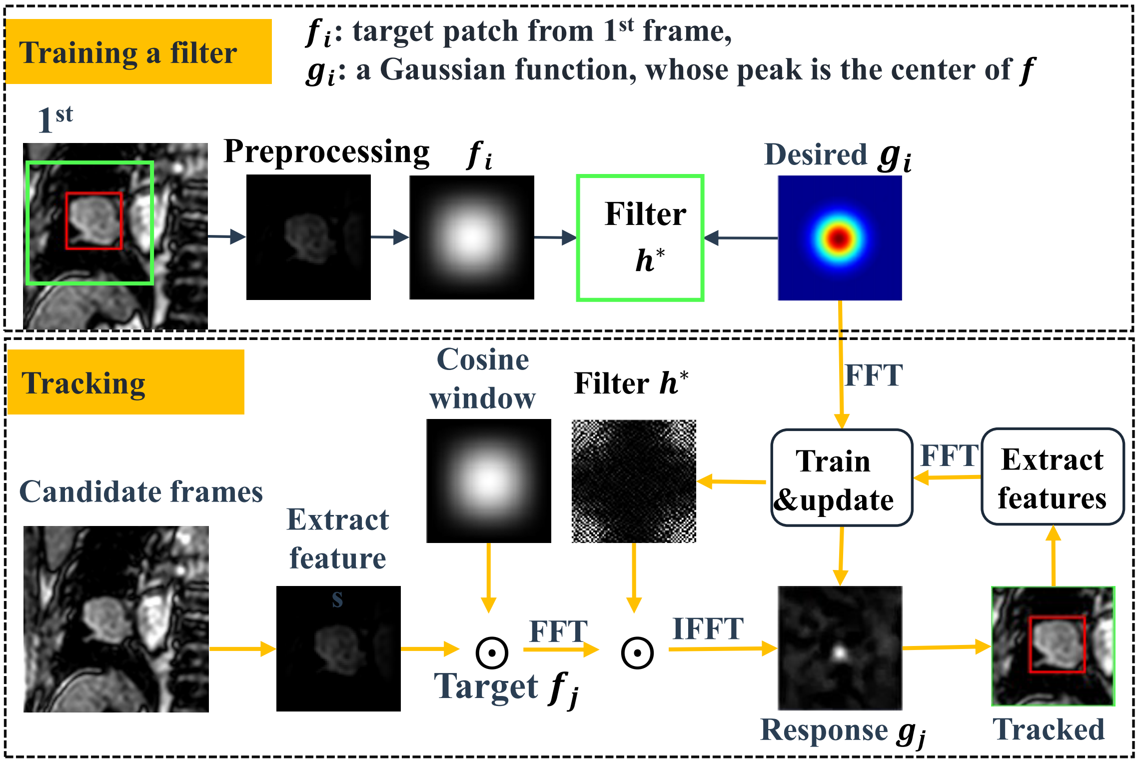

FIGURE 2.2 – Flowchart of tumour tracking using the MOSSE algorithm.

From the formula point of view, it is hoped to train a filter h that can satisfy :

$$g = f \otimes h \tag{2.2}$$

By Fourier transform convert to frequency domain :

$$G = F \bigodot H^* \tag{2.3}$$

where * stands for complex conjugation, $\odot$ for element-wise multiplication and $\otimes$ for spatial 2-D convolution. In order to increase the robustness of H^*, the target of the first frame image was transformed several times to obtain multiple versions of f_i by translation and rotations together with the corresponding g_i with ground truth locations, to constitute a data set. The MOSSE aims to determine a filter H to minimize the sum of squared errors between the actual output of the convolution and the desired output.

$$\sum{}_i |F_i \bigodot H^* - G_i|^2 \tag{2.4}$$

This minimization process determines the optimal filter that effectively maps the training inputs to their corresponding desired outputs, with the analytic form :

$$H^* = \frac{\sum{}_i G_i \odot F_i^*}{\sum{}_i F_i \odot F_i^*} \tag{2.5}$$

Note that the power of MOSSE lies in its simplicity of the analytic solution and its complexity ($\mathcal{O}(N \log N)$) due to the Fourier transform instead of $\mathcal{O}(N^2)$ with spatial correlations. An online adaptive version also exists to update the templates :

$$H^* = \frac{A_i}{B_i} \tag{2.6}$$

$$A_i = \eta G_i \bigodot F_i^* + (1 - \eta) A_{i-1} \tag{2.7}$$

$$B_i = \eta F_i \bigodot F_i^* + (1 - \eta) B_{i-1} \tag{2.8}$$

where η is the learning rate, and the larger η, the more information is retained for the current frame and the less is retained for historical information. The optimal value given in [149] is 0.125.

2.2.3 Kernel correlation filter (KCF)

The KCF was first proposed in [58] as a computationally efficient method used for object tracking, particularly suitable for visual tracking tasks. A detailed description of the KCF formulation was given in [58]. The KCF algorithm is similar to the MOSSE in

terms of process, with the following improvements :
1. Ridge regression : The KCF adds a regularization term to the objective function

$$min \sum_i (y_i - \omega^T x_i)^2 + \lambda \|\omega\|_2^2 \tag{2.9}$$

leading to an analytic regularized least-square solution :

$$\omega = (X^T X + \lambda I)^{-1} X^T y, \tag{2.10}$$

where X is the concatenated matrix formed by x_i, the training samples, y_i the response values, ω the filter template, and the λ the regularization coefficient. Note that the spatial convolution operation is replaced by the dot-product of vectors in this formulation.
2. Cyclic shifts and circulant matrices : The cyclic shift is used to produce a cyclic matrix of the training sample, which can be diagonalized by the Fourier transform to further reduce the amount of computation. The cyclic matrix approach expands the number of negative samples to enhance the performance of the tracker. Cyclic shifts refer to shifting the location of a sample within a track by a certain number of frames. Figure 2.3 shows examples of vertical cyclic shifts of a base sample. The image moves up or down several different pixels to generate new sample images to effectively increase the number of samples, which helps to improve the training accuracy of the classifier.

FIGURE 2.3 – Examples of vertical cyclic shifts of a base sample. Our Fourier domain formulation allows us to train a tracker with all possible cyclic shifts of a base sample, both vertical and horizontal, without iterating them explicitly. Artifacts from the wrapped-around edges can be seen (top of the left-most image), but are mitigated by the cosine window and padding.

An illustration of the resulting pattern of a circulant matrix is given in Figure 2.4. Notice that the pattern is deterministic, and fully specified by the generating vector x, which is the first row. All circulant matrices are made diagonal by the Discrete Fourier

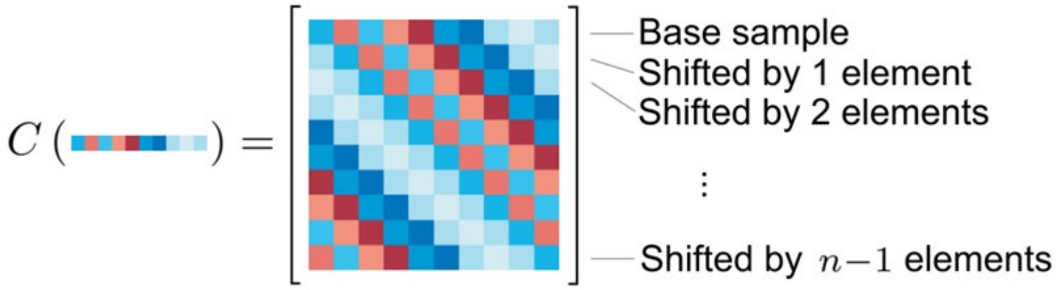

FIGURE 2.4 – Illustration of a circulant matrix. The rows are cyclic shifts of a vector image, or its translations in 1D. The same properties carry over to circulant matrices containing 2D images.

Transform (DFT), this can be expressed as

$$X = F\mathrm{diag}(\hat{x})F^H \tag{2.11}$$

where F is a constant matrix that does not depend on x ,and $\hat{x}$ denotes the DFT of the generating vector, $\hat{x} = F(x)$. From now on, we will always use a hat ˆ as shorthand for the DFT of a vector. The constant matrix F is known as the DFT matrix, and is the unique matrix that computes the DFT of any input vector, as $F(z) = \sqrt{n}Fz$. This is possible because the DFT is a linear operation. Eq.2.12 expresses the eigendecomposition of a general circulant matrix. The shared, deterministic eigenvectors F lie at the root of many uncommon features, such as commutativity or closed-form inversion. Diagonalization with circulant matrices allows to simplify the linear regression in Eq.2.10, when the training data is composed of cyclic shifts. Then the full expression for linear regression (Eq.2.10) is given by,

$$\hat{\omega} = \frac{\hat{x}^* \odot \hat{y}}{\hat{x}^* \odot \hat{x} + \lambda} \tag{2.12}$$

The fraction denotes element-wise division. We can easily recover ω in the spatial domain with the Inverse DFT ($\mathcal{O}(N \log N)$).

3. Kernelized Filtering : *The kernel trick* $\varphi^T(x)\varphi(x') = k(x, x')$ replaces further dot-products with the kernel function k, such that any pair of dot-product are stored in a $n \times n$ kernel matrix K, with elements $K_{i,j} = k(x_i, x_j)$.

A Gaussian kernel was utilized to map the input from the linear space (the original space) to the nonlinear feature-space $\varphi(x)$ (the dual space), while the vector ω in the original space is represented as a linear combination of the basis vectors in the dual space :

$$\omega = \sum_i \alpha_i \varphi(x_i) \tag{2.13}$$

The solution to the kernelized version of Ridge Regression is given by

$$\alpha = (K + \lambda I)^{-1} y, \tag{2.14}$$

where K is the kernel matrix, and α the vector containing coefficients α_i as the solution in the dual space. For the detection, a regression function is calculated for each image patch (candidate) z in the frame as follows :

$$\hat{f}(z) = (\hat{k}^{xz})^* \bigodot \hat{\alpha} \tag{2.15}$$

Here, $\hat{k}^{xz}$ represents the kernel correlation between the target x and the candidate z. Each $f(z)$ is a linear combination of the neighboring kernel values from $\hat{k}^{xz}$, weighted by the learned coefficients α in Fourier domain. The candidate with the highest response (kernelilzed correlation) corresponds to the tracked location.

2.2.4 Centroid of the tracked tumor

Due to factors such as irregular tumor shapes and deformations during the respiratory movement, the 2D cine-MRI over the time series are diverse, contain tumours of various shapes, potentially resulting in inaccurate tracking by looking for the optimal location of a bounding box of a fixed size. It is worth noting that the outputs of TM, MOSSE, and KCF are typically pixel boxes $I^{tracked}_{(J\times K)}$ containing the target position, but they may not accurately localize the target itself. Note that the outputs of the TM, MOSSE, and KCF are all matrices $I_{\text{tracked}}(J \times K)$ of either direct or kernelized correlation values calculated around the real target locations.

To achieve more accurate tracking, as shown in Figure 2.5, we first outline the tumor's shape from the template in the first frame, resulting in a binary mask matrix called $Mask_{(J\times K)}$, where m represents each element with $m \in 0, 1$. Then, this mask is applied to the subsequent tracked box, denoted as $I^{masked}_{(J\times K)}$, which is obtained by performing a bitwise AND operation between (Mask) and $I^{tracked}_{(J\times K)}$. The centroid of the masked region is calculated based on the grayscale values of the image using the following equation :

$$
\begin{aligned}
c_i &= \frac{\sum_{i=1}^{J}\sum_{j=1}^{K} I_{\text{masked}}(i,j)\cdot i}{\sum_{i=1}^{J}\sum_{j=1}^{K} I_{\text{masked}}(i,j)} \\
c_j &= \frac{\sum_{i=1}^{J}\sum_{j=1}^{K} I_{\text{masked}}(i,j)\cdot j}{\sum_{i=1}^{J}\sum_{j=1}^{K} I_{\text{masked}}(i,j)}
\end{aligned}
\tag{2.16}
$$

where $I_{\text{masked}}(i,j)$ represents the pixel value at the coordinates (i,j).

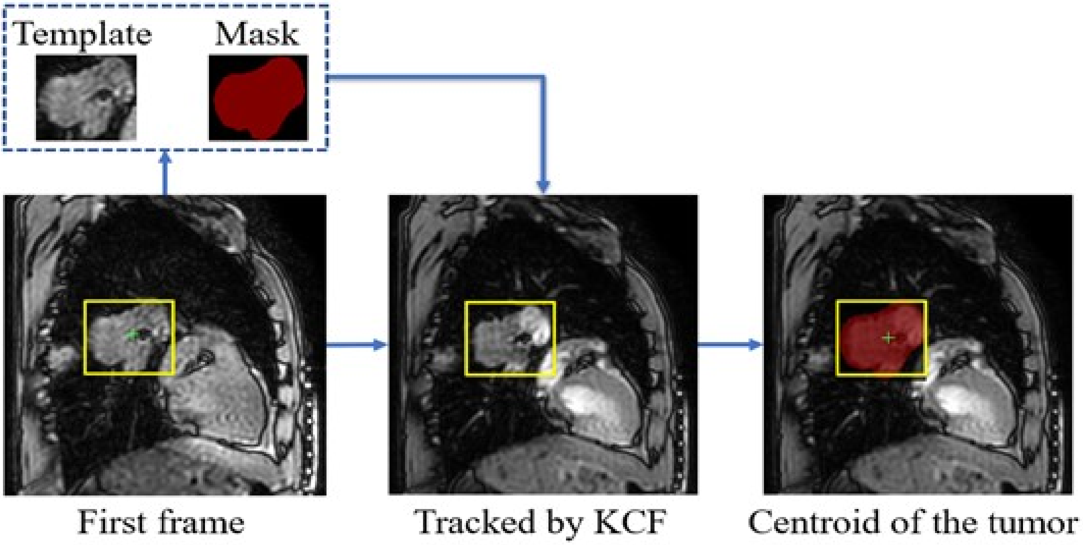

FIGURE 2.5 – Diagram of improved target tracking by calculating the center of mass. The yellow box represents the tumor boundary in the first or subsequent frames, and the green "+" indicates the centroid of the tumor in the first or subsequent frames.

Figure 2.6 shows four consecutive sagittal slices of the liver in the first row. Figure 2.6(a) represents the template, where the yellow box manually annotates the liver edge, and the red "+" indicates the centroid of the liver. Figures 2.6(b-d) represent the subsequent three frames of MRI, with the yellow boxes indicating the results of boundary tracking, and the red "+" indicating the results of liver centroid tracking. As shown in Figures 2.6(c-d), due to liver deformation, there is a significant error in tracking the upper edge of the liver. However, after calculating the centroid, the position of the centroid remains stable on the liver. Figures 2.6(e-f) show the motion curves of boundary tracking and centroid tracking in the corresponding SI and AP directions. The respiratory curve after centroid calculation exhibits better consistency in amplitude, especially in the AP direction.

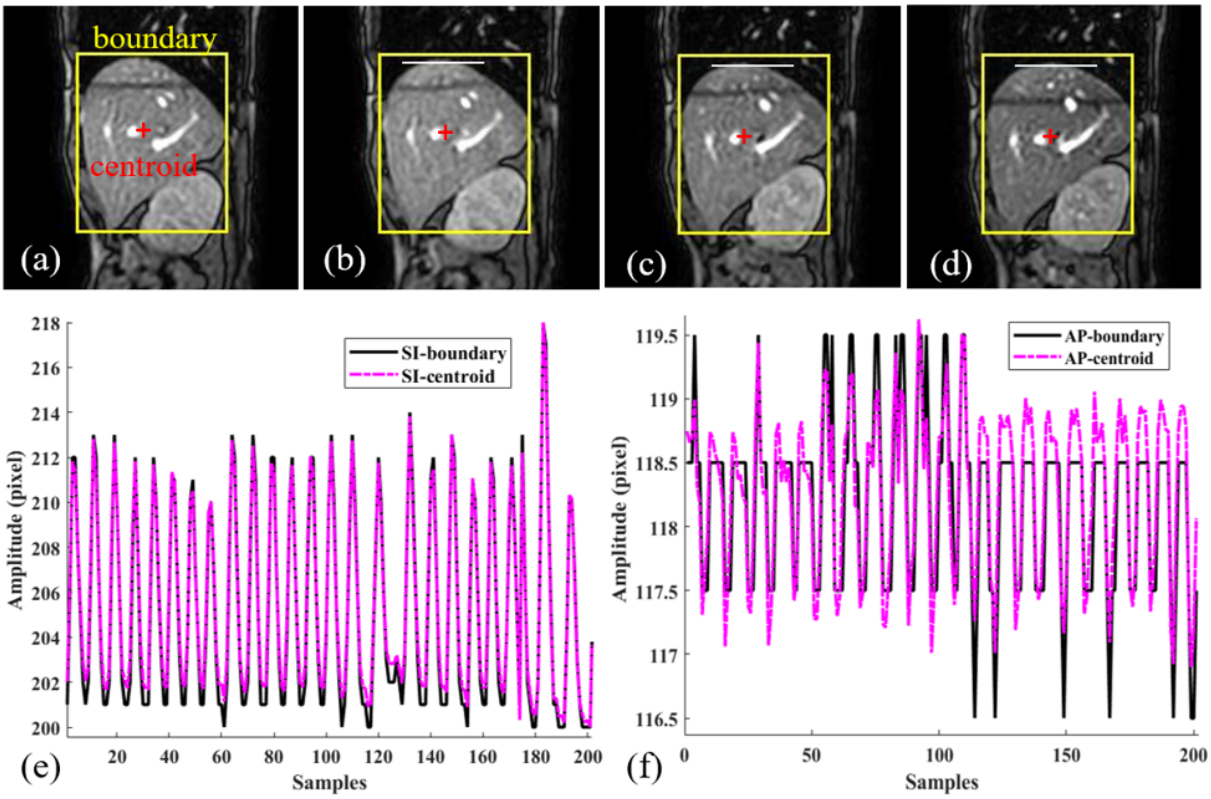

Figure 2.6 – Improvements in target tracking by centre-of-mass computation. In the first row of the cine-MRI sequence, the yellow box indicates the results of boundary tracking, and the red '+' indicates the results of centre-of-mass tracking in the liver ; the curves in the second row indicate the motion profiles of boundary and centre-of-mass tracking in the corresponding SI and AP directions.

2.3 Materials and methods

2.3.1 Data acquisition

The study included a total of 20 patients, with 10 diagnosed with lung cancer and 10 with liver cancer. The average age of the patients was 64.6 years, ranging from 47 to 83 years. All patients underwent radiation therapy between October 2020 and May 2022. 2D cine-MR were collected at the beginning of each radiotherapy session, with an acquisition duration ranging from 313 to 483 seconds and an average collection time of 414 seconds. Before participating in the study, all subjects provided informed consent and were provided with a detailed description of the research protocol.

2D cine-MRI with 5Hz imaging frequency were acquired by the Unity comprising an Achieva 1.5T MR scanner and a 7 MV flattening-filter-free linear accelerator. To strike a balance between acquisition time, signal-to-noise ratio, and resolution, we opted for an acquisition frequency of 5Hz, which is considered to be reasonable [74]. The spatial resolution of 2D cine-MRI is 3×3 mm^2. The MRI-Linac allows real-time acquisition of three orthogonal planes (coronal, sagittal, and transverse), with motion in the Left-Right (LR) and Superior-Inferior (SI) directions measured from coronal slices, and motion in the Anterior-Posterior (AP) direction derived from sagittal slices.

2.3.2 Coronal or sigattal selection for SI direction

From a general perspective, during irradiation, tracking should refer to the isocentric position defined in the treatment plan, ensuring consistent information regardless of the orientation of the detected slices [145]. On the one hand, movement measurements of the SI direction can be simultaneously obtained from both coronal and sagittal slices. On the other hand, due to the irregularity of malignant tumor margins, the shape of the tumour usually varies between these two slices, potentially leading to incoherent tracking results. To address this issue, we proposed a preselection of either coronal or sagittal sequences for the extraction of SI measurements by calculating the correlation between the template of the first frame and the subsequent 20 frames for both coronal and sagittal slices. Slices with higher spatial correlations were thus retained for the SI direction tracking for the treatment (as shown in figure 2.7).

To verify the pertinence of using only the first 20 frames, we also calculated the correlations between the template and all subsequent frames. Table 2.1 illustrates the consistance of spatial correlations for each patient in both coronal and sagittal slices : 1) inter-patient discrepancies are observed for both lung and liver cancer patients (coronal plans are preferred for 4 out of 10 for lung cancer, and 3 out of 10 for liver cancer) ; 2) fortunately higher correlations with a substantial margin for the first 20 frames is a clear sign of higher correlations all along the treatment. Figure 2.7 further demonstrated these observations for liver patient 1 and 8, from which we also noticed the pseudo-periodic nature of correlation coefficients in both plans suggesting the tumor shape deformation during different phases in the respiration process due to the fixed template used to calculate these coefficients. We could reasonably deduce that the minimum duration (number of frames) for plan selection should be one respiration cycle, also a variable parameter for different patients. Thus, this criterion can effectively help to select for each patient between the coronal or sagittal plans to be used to capture motion in the SI direction.

Table 2.1 – Correlation (%) comparison for SI direction slice choices between coronal and sagittal for 10 lung cancer patients and 10 liver cancer patients. Bold indicates the slices selected as determining SI directional motion

	Lung				Liver			
No.	Cor(20)[1]	Cor(all)[2]	Sag(20)	Sag(all)	Cor(20)	Cor(all)	Sag(20)	Sag(all)
1	95.5	94.7	**97.0**	**96.6**	91.9	91.3	**95.0**	**94.4**
2	**96.1**	**95.9**	94.8	94.3	91.7	91.3	**94.5**	**93.9**
3	92.2	91.3	**97.7**	**97.5**	94.2	93.2	**97.6**	**97.6**
4	91.2	90.8	**97.7**	**97.5**	**95.0**	**94.1**	92.9	91.7
5	96.0	95.4	**96.1**	**96.1**	94.3	92.7	**95.0**	**95.2**
6	**96.3**	**96.2**	91.2	90.6	92.2	89.2	**95.8**	**93.3**
7	93.5	93.3	**97.1**	**97.2**	**93.5**	**92.5**	92.0	89.7
8	97.4	97.3	**97.6**	**97.5**	**95.3**	**95.0**	91.0	89.7
9	**97.7**	**97.5**	92.4	92.2	94.7	93.9	**97.9**	**97.9**
10	**98.4**	**98.0**	94.6	93.8	94.4	93.9	**97.3**	**97.2**

[1] 20, correlation between template and the first 20 frames

[2] all,correlation between template and all the rest frames

2.3.3 Performance evaluation

We proposed to evaluate both the static performance (tracking error) within each frame and the dynamic performance (predicted gating) as compared with reference gating derived from future measurements.

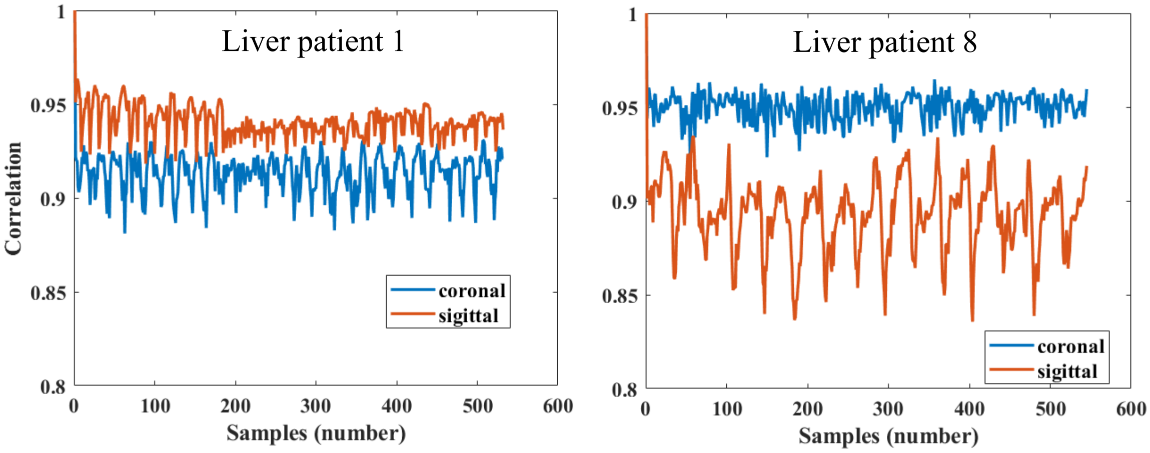

FIGURE 2.7 – Correlation between template and the subsequent slices of two liver cancer patients.

Tracking error

Tracking errors for the trackers were estimated as the absolute difference between the tumor position determined using the automated (auto) trackers and the ground truth (man) established by the radiation oncologist for each frame, as shown by

$$\begin{cases} \Delta SI & = |SI_{\text{auto}} - SI_{\text{man}}| \\ \Delta AP & = |AP_{\text{auto}} - AP_{\text{man}}| \\ \Delta LR & = |LR_{\text{auto}} - LR_{\text{man}}| \end{cases} \tag{2.17}$$

Here, ΔSI, ΔAP, and ΔLR represent the tracking errors in the SI, AP, and LR directions, respectively. The absolute difference between the automated and ground truth positions is taken to quantify the accuracy of the automated trackers in predicting the tumor position.

2.4 Results and Discussion

2.4.1 Tracking error

Table2.2 presents the average tracking results (errors measured in pixels) for both boundary and centroid (lung tumor and liver organ) using TM, KCF, and MOSSE algorithms, compared to the ground truth, for 10 lung cancer patients and 10 liver cancer patients. Across all 20 patients, when tracking the centroid of the target, the errors are significantly ($p < 0.05$) smaller compared to tracking the boundary of the tumor.

Among the 10 lung cancer patients, the KCF algorithm demonstrated the best performance, with average tracking errors of 0.32 and 0.25 pixels in the LR and SI directions for coronal slices, and 0.3 and 0.22 pixels in the AP and SI directions for sagittal slices. For the 10 liver cancer patients, only the TM algorithm performed best in the SI direction of coronal slices, achieving an average tracking error of 0.52 pixels. However, for all other cases, the KCF algorithm outperformed the others, with mean tracking errors of 0.47, 0.53, and 0.55 pixels in the LR, AP, and SI directions, respectively, as obtained from the sagittal plane.

Table 2.2 – Tracking results (errors measured in pixels) of both boundary and centroid (lung tumor and liver organ) using TM, KCF and MOSSE algorithms for 10 lung cancer patients and 10 liver cancer patients.

Orientation		Boundary			Centroid		
		TM	KCF	MOSSE	TM	KCF	MOSSE
lung	LR(Cor)	0.52±0.25	0.49±0.14	0.54±0.18	0.38±0.24	**0.32±0.14**	0.39± 0.22
	SI(Cor)[1]	0.52±0.18	0.48±0.12	0.47±0.14	0.28±0.08	0.25±0.07	0.31± 0.10
	AP(Sag)	0.65±0.22	0.50±0.06	0.59±0.14	0.37±0.15	**0.30±0.12**	0.37± 0.14
	SI(Sag)[2]	0.58±0.11	0.52±0.14	0.52±0.16	0.28±0.09	0.22±0.08	0.33± 0.21
	SI(optimal)[2]	0.45±0.12	0.42±0.10	0.44±0.12	0.25±0.07	**0.19±0.06**	0.29± 0.09
	Comp(ms)[3]	3.4±1.07	2.6±0.97	1.1±0.32	5.4±1.07	5.2±0.92	3.4±0.52
liver	LR(Cor)	1.10±0.3	0.86±0.19	1.17±0.6	0.52±0.18	**0.47±0.16**	0.60± 0.36
	SI(Cor)	1.30±0.69	1.4±0.45	1.45±0.35	0.52±0.15	0.59±0.16	0.71± 0.19
	AP(Sag)	1.11±0.89	0.86±0.29	0.91±0.27	0.58±0.35	**0.53±0.28**	0.61± 0.33
	SI(Sag)	1.21±0.36	1.09±0.33	1.19±0.37	0.61±0.43	0.55±0.30	0.67± 0.37
	SI(optimal)[2]	1.19±0.35	1.01±0.30	1.10±0.32	0.50±0.15	**0.50±0.14**	0.60± 0.16
	Comp(ms)	13.9±5.67	4.3±1.25	1.8±0.63	16.0±5.66	6.50±1.43	4.6±0.84

[1] SI(Cor), tumor motion in SI direction from coronal slice

[2] SI(Sag), tumor motion in SI direction from sagittal slice

[3] Com(ms), computational time.

Figure 2.8 illustrates the comparison between algorithm-based tracking trajectories and real motion trajectories using a motion curve of lung cancer as an example. In figure 2.8(a), the tracking results in the superior-inferior (SI) direction are compared between the real motion trajectory and three centroid-improved tracking algorithms. Figure 2.8(b) compares the tracking trajectories in three-dimensional space using the improved KCF algorithm with the real motion trajectory. It is evident from figure 2.8 that the improved KCF algorithm significantly outperforms the MOSSE and TM algorithms in the SI direction. In terms of the overall 3D tracking trajectory, the improved KCF algorithm closely aligns with the real motion range, meeting the accuracy requirements for real-time tumor tracking.

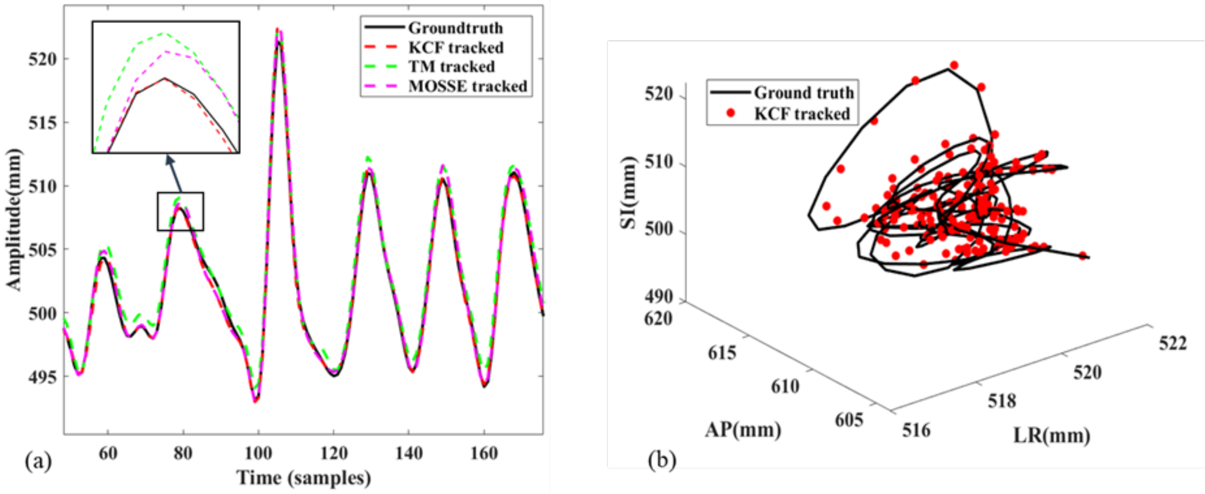

FIGURE 2.8 – Tracking trajectory of Patient 1 with lung cancer and comparison with the real motion trajectory. (a) Comparison of the real motion trajectory with the tracking results in the superior-inferior (SI) direction using three centroid-improved tracking algorithms, (b) Tracking trajectories in three-dimensional space using KCF with improvements and comparison with the real motion trajectory.

2.4.2 Complexity and computational time

All experiments were conducted using MATLAB (The MathWorks Inc, Natick, MA) on a machine equipped with an Intel 4-core 2.4-GHz CPU, NVIDIA GeForce GTX 1660 Ti GPU, 512 GB SSD, and 20 GB RAM. The computation cost was measured by the execution time required for tumor tracking, motion prediction, and generation of the 3D gating signal. Specifically, this experiment focused solely on comparing tumor localization among the three trackers, while other processes in the system remained unchanged. Therefore, any differences in computation cost were observed exclusively in the three trackers. As mentioned earlier, the primary goal of the trackers was to track the entire target region (lung tumor or liver organ) on cine-MRI.

Henriques et al. [58] reported that the KCF tracker achieves O(n log n) complexity by leveraging the fast Fourier transform, which reduces computing time compared to more computationally expensive matrix algebra. The speed of the KCF tracker is directly influenced by the size of the tracked region ($M \times N$).

2.4.3 Discussion

In this chapter, we primarily focused on algorithms and related issues for tumor tracking under 2D Cine-MRI guidance. Firstly, we introduced three main tracking algorithms : TM, MOSSE, and KCF, utilized for real-time tumor tracking. The application of these algorithms during 2D cine-MRI-guided therapy provides feasibility for compensating respiratory motion and forms the basis for the implementation of patient-specific gating schemes.

In the detailed discussion of the algorithms, we observed that the MOSSE algorithm is a rapid method applying correlation filters to target tracking, establishing a target response map through Fourier transform during the training process. In contrast, the KCF algorithm introduces improvements such as ridge regression, cyclic shifting, and kernelized filtering on the basis of the MOSSE algorithm, enhancing the tracking performance for tumor motion. Through comparisons of different algorithms in lung and liver cancer patients, we found that the KCF algorithm exhibits the best performance in terms of time cost and tracking accuracy, which is crucial for accurate monitoring of tumor position.

Additionally, we noted that the irregularity of tumor shape and respiratory motion during irradiation may lead to variations in 2D Cine-MR slice. To address this issue, we proposed a centroid-based method, outlining the tumor shape to obtain a binary mask matrix applied to the tracking frame. The introduction of this step effectively improves the accuracy of tumor position, especially in cases of deformation caused by respiratory motion.

Regarding the positioning issue in the SI direction, et al. [145] suggested that SI motion trajectories could be obtained equally well from both slice directions during cine MRI-guided therapy, and they demonstrated that the same information could be obtained regardless of which slice direction was detected. However, due to the irregularity of malignant tumor margins, the shape of the tumor often differs between these two planes, which can affect the accuracy of tumor localization.

To enhance the accuracy of tumor localization, we calculated the correlation between the first template frame in the coronal plane and the subsequent 20 frames, as well as the correlation in the sagittal plane, and selected the plane with the higher correlation as the location of the SI direction.Geometric uncertainty and computational cost in the prediction of automatic tumor tracking and gating signals were quantified by simulating beam gating. Three correlation-based tracking algorithms were tested : TM, MOSSE, and KCF. Based on these algorithms, we calculated the tumor center of mass to improve tracking accuracy. KCF performed best in terms of both time cost and tracking accuracy for both liver and lung cancer patients. This confirms the superiority of the KCF algorithm in patient-specific gating schemes for thoracoabdominal tumors.

2.5 Conclusion

This chapter first constructed a Unity database and evaluated the geometric accuracy and computational efficiency of three tumor tracking algorithms (TM, KCF, and MOSSE) using 2D cine-MRI data from 20 patients. The KCF algorithm was chosen as the tracker, and the region returned by it with the maximum response is considered as the position of the tracked target. The tracking accuracy is further improved by computing the centroid of pixels covered by the template. To determine the optimal position of the tumor in the superior-inferior (SI) direction, coronal or sagittal slices with stronger template correlation were selected. In summary, the proposed workflow for tumor tracking based on KCF proves to be efficient and accurate on 2D Cine-MRI, offering robust support for respiratory motion compensation in radiotherapy for thoracic and abdominal cancer patients. This experience contributes valuable insights for precise radiotherapy.

CHAPITRE 3

TUMOR MOTION PREDICTION USING TRANSFER C-NLSTM

3.1 Introduction

The emergence of MR-Linac systems such as the Elekta Unity has opened up new possibilities for providing higher-precision gating signals. These systems can directly visualize tumors and internal structures without relying on implanted fiducial markers or external respiratory signals to locate the treatment target. However, there exists always a certain system delay between the tracking of target and delivery of radiation. Consequently the tumor may have moved, potentially leading to misalignment and inaccurate radiation delivery. Some studies [86][9] have revealed that the Unity system can limit the system delay to within 0.5 seconds, including processes such as image acquisition, trajectory extraction, and beam trigger activation. To compensate for the delay, real-time prediction of the gating structure (either tumor or surrounding organs) is essential in assuring the synchronization of dosage delivery.

We first investigated the problem from the respiration trace prediction point of view, in the hope of benefiting from the massively available open-source databases of respiration traces [36][66]. Various methods have been investigated for trajectory prediction with respiration motions. One simple method was based on a sinusoidal model containing a few sinusoidal components of different frequency and amplitudes. Fitting with the least square criterium was applied to predict the future respiration motion traces. However, this approach is not suitable for irregular respiratory trajectories [173]. Lee et al. [87] introduced a prediction algorithm based on the Extended Kalman Filter (EKF) for continuous tracking and updating of the model's frequency and amplitude, allowing for variations in the frequency and amplitude of breathing patterns. Bukhari et al. [17] combined Kalman filtering with Gaussian process regression for respiratory motion prediction. Ruan et al. [137] used Kernel Density Estimation (KDE) for respiratory motion prediction, weighted and summed target samples from training data for prediction. Ernst et al. [37] proposed a multiscale autoregressive approach, which is a self-regressive analysis-based method for predicting respiratory motion. Ernst et al. [38] demonstrated the superior prediction accuracy of adaptive Support Vector Regression (SVR) predictors over wavelet-based linear prediction. Autoregressive Integrated Moving Average (ARIMA) is another commonly used time series analysis model, reported to have higher accuracy in respiratory prediction [151][75][4]. These studies found that all methods could reduce position errors, but these traditional methods have certain limitations. For instance, in case of significant noise or jitter affecting the respiratory motion signal, traditional methods such as sinusoidal-based and regression-based methods often struggle to provide effective predictions. Furthermore, most traditional models are confined to predicting respiratory signals in a single direction.

Compared to traditional methods, learning-based approaches employ more complex neural networks or adaptive filters, thereby providing greater adaptability and non-linearity in predicting a patient's respiratory motion, especially in cases of irregular breathing patterns. RNNs possess shared memory, parameters, and Turing completeness [7][110]. Two variants of RNNs are Long Short-Term Memory (LSTM) [60][101] and Gated Recurrent Unit (GRU) [165]. They inherit most of the characteristics of RNNs and address the issues of gradient vanishing and exploding gradients that arise during training on long sequences, overcoming the difficulties faced by RNNs in capturing long-distance dependencies. Lin et al. [92] proposed a deep LSTM model for predicting external respiratory signals during radiation therapy and demonstrated the potential of deep LSTM models in respiratory motion prediction. Wang et al. [177] introduced a seven-layer bidirectional LSTM and a deep neural network with a 0.4-second output layer, showing significantly improved prediction accuracy over traditional autoregressive integrated moving average models. Yu et al. [191] presented a rapid prediction model based on bidirectional GRU, achieving fast network updates and completing prediction model updates within one cycle of X-ray acquisition.

While the above-mentioned deep learning methods convincing predictive performances in capturing surface respiratory signals during the CyberKnife treatments[92][177], it is important to note that applying these methods directly to MRgRT may present some difficulties, due to differences in imaging patterns.While merely 30 ms is required for X-ray fluoroscopy, the 2D cine-MRI has acquisition cycles ranging from 150 to 380 ms, as compared with the Elekta Unity's overall gating system delay of up to 500 ms. Therefore, it is crucial to validate the effectiveness of prediction models in the context of 2D cine-MRI with low sampling frequency and important system delays. Additionally, training a robust deep learning model requires a substantial amount of annotated tumor motion data, for example, Lin et al[92] used 1187 traces (more than 20 hours) for model development. However, obtaining such data on the Unity is often challenging or costly. Moreover, considering the significant inter-patient variabilities in respiratory motion patterns, training a patient-specific RNN model would be a pertinent solution but faced with even less available data.

To address the aforementioned challenges, this study proposes a transfer C-NLSTM framework for real-time prediction of respiratory motion in tumors based on 2D cine-MRI. The process is illustrated in figure 3.1. The main contributions are summarized as follows :

1. C-NLSTM model : The truncated respiratory signal was initially passed through a Convolutional Neural Network (1D-CNN), which effectively extracts internal structural features of the respiratory signal. Subsequently, the output of the CNN model underwent max-pooling to reduce parameter dimensions, and the features learned by the CNN were used as inputs for the NLSTM. Next, a time-distributed fully connected (FC) layer was employed to take the outputs from all time steps of the NLSTM as input, and a one-dimensional average pooling layer, less prone to overfitting than traditional fully connected layers, was applied. Finally, an FC layer was used to output the predicted respiratory signal. The C-NLSTM model was tested and pretrained on two publicly available databases, CyberKnife and Fantasia.

2. Transfer C-NLSTM : This framework consisted of a pretrained C-NLSTM model and a target C-NLSTM model. The former was trained using a large amount of historical data to extract and simulate patterns and characteristics similar to tumor motion. The parameters, structure, and hyperparameters of this pretrained model were then used to initialize the target C-NLSTM model. The target model was further optimized using 2 minutes of the Unity data, and the remaining data was used to evaluate the proposed transfer model. This approach effectively reduced training time and computational resources while improving the model's performance on new data. The effectiveness of transfer learning for short-term training was also validated on the Fantasia database.

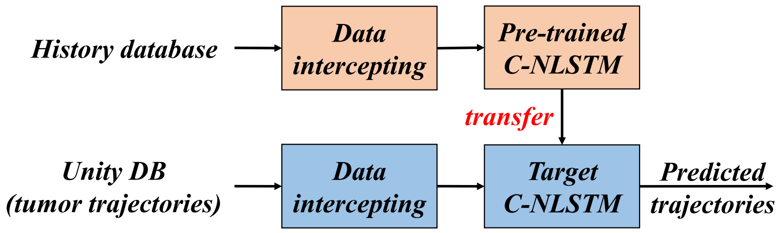

FIGURE 3.1 – Workflow of proposed transfer C-NLSTM model for respiration motion prediction.

3.2 A transfer C-NLSTM framework

Due to the insufficient labeled data, transfer learning technology was applied in this paper to improve the training accuracy of the C-NLSTM model with limited amount of labeled data. It has been proven in several previous studies that 1) network-based deep transfer learning, which always transfer the partial structure and parameters of a pre-trained deep neural network in source domain to another network in target domain, is effective with reduced size of labeled data in the target domain [162], 2) the temporal convolutional network is used as a feature extraction module is an effective method for time series analysis [90][108] and 3) the LSTM model has the potential to predict respiratory signals [92].

Drawing upon the aforementioned research, we have combined the full convolutional neural network with the nested LSTM model to develop the C-NLSTM model. Furthermore, by incorporating transfer learning techniques, we have proposed the Transfer C-NLSTM framework.

3.2.1 Fully Convolutional Network

1D-CNN can effectively extract features from temporal data and has been proven to be an effective method for time series analysis [71]. To prevent overfitting to noise in the training data, the simplicity and shallow structure of the CNN model are maintained in this study, consisting of a convolutional block with a single convolutional layer and a Rectified Linear Unit (ReLU) activation function. The convolutional layer in this block has 32 convolutional kernels with a receptive field of 8 (i.e., 1×8). The lower layers of the CNN model can capture numerous microstructure patterns in the respiratory signal, which are then processed by higher-level layers into discriminative features relevant to respiratory trajectories. The output of the CNN is fed to max pooling layer to reduce the number of model parameters.

3.2.2 Nested long short-term memory

In order to encode an additional implicit prior of temporal hierarchy, Moniz and Krueger proposed a novel Nested LSTM architecture, which constructs temporal hierarchies in memory by selectively accessing memory via nesting [90]. As shown in fig 3.2, the NLSTM architecture increases depth to LSTMs via nesting rather than stacking. The operation for calculating the value of a memory cell in NLSTM is replaced with an LSTM memory cell. Also the longer-term information related to the current respiratory signals epoch can be selected by the LSTM gates.

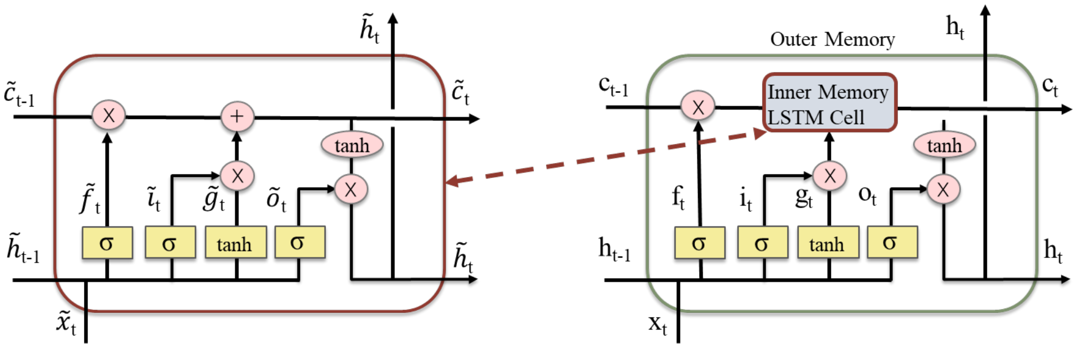

(a) LSTM Cell (b) NLSTM Cell

FIGURE 3.2 – Detailed schematic of the NLSTM architecture.

A common LSTM unit shown in fig 3.2(a) is composed of an input gate, an output gate and a forget gate. The cell remembers values over arbitrary time intervals and the three gates regulate the flow of information into and out of the cell. The compact forms of the equations for the forward pass of an LSTM cell with a forget gate are :

$$\begin{cases} \tilde{i}_t = \tilde{\sigma}_i(\tilde{x}_t\tilde{W}_{\tilde{x}i} + \tilde{h}_{t-1}\tilde{W}_{\tilde{h}i} + \tilde{b}_i) \\ \tilde{f}_t = \tilde{\sigma}_f(\tilde{x}_t\tilde{W}_{xf} + \tilde{h}_{t-1}\tilde{W}_{hf} + \tilde{b}_f) \\ \tilde{g}_t = \tilde{\sigma}_c(\tilde{x}_c\tilde{W}_{xc} + \tilde{h}_{t-1}\tilde{W}_{hc} + \tilde{b}_c) \\ \tilde{c}_t = \tilde{f}_t \odot \tilde{c}_{t-1} + \tilde{i}_t \odot \tilde{g}_t \\ \tilde{o}_t = \tilde{\sigma}_o(\tilde{x}_t\tilde{W}_{xo} + \tilde{h}_{t-1}\tilde{W}_{ho} + \tilde{b}_o) \\ \tilde{h}_t = \tilde{o}_t \odot \tilde{\sigma}_h(\tilde{c}_t) \end{cases} \tag{3.1}$$

where $\tilde{x}_t$ and $\tilde{h}_{t-1}$ denote the inputs of the inner LSTM unit and can be computed based on the parameters of the outer unit :

$$\begin{cases} \tilde{x}_t = i_t \odot \sigma_c(x_t W_x c + h_{t-1} W_h c + b_c) \\ \tilde{h}_{t-1} = f_t \odot \tilde{c}_{t-1} \end{cases} \tag{3.2}$$

where $\tilde{i}_t$,$\tilde{f}_t$, and $\tilde{o}_t$ represent the states of the three gates ; $\tilde{c}_t$ represents the cell input state ; $\tilde{W}_{xi}$, $\tilde{W}_{xf}$, $\tilde{W}_{xo}$, and $\tilde{W}_{xc}$ represent the weight vectors that connect $\tilde{x}_t$, to the three gates and cell input ; $\tilde{W}_{hi}$, $\tilde{W}_{hf}$, $\tilde{W}_{ho}$, and $\tilde{W}_{hc}$ represent the weight vectors that connect $\tilde{h}_{t-1}$ to the three gates and cell input ; $\tilde{b}_i$, $\tilde{b}_f$, $\tilde{b}_o$, and $\tilde{b}_c$ represent the biases of the three gates and cell input ; σ denotes the sigmoid function, and $\odot$ denotes the scalar product of two vectors. The cell state of the outer LSTM changes with the output of the inner LSTM unit, which is expressed as

$$c_t = \tilde{h}_t \tag{3.3}$$

In this study, the NLSTM was used to extract the temporal dependencies in respiratory signals in the output of the feature extraction module.

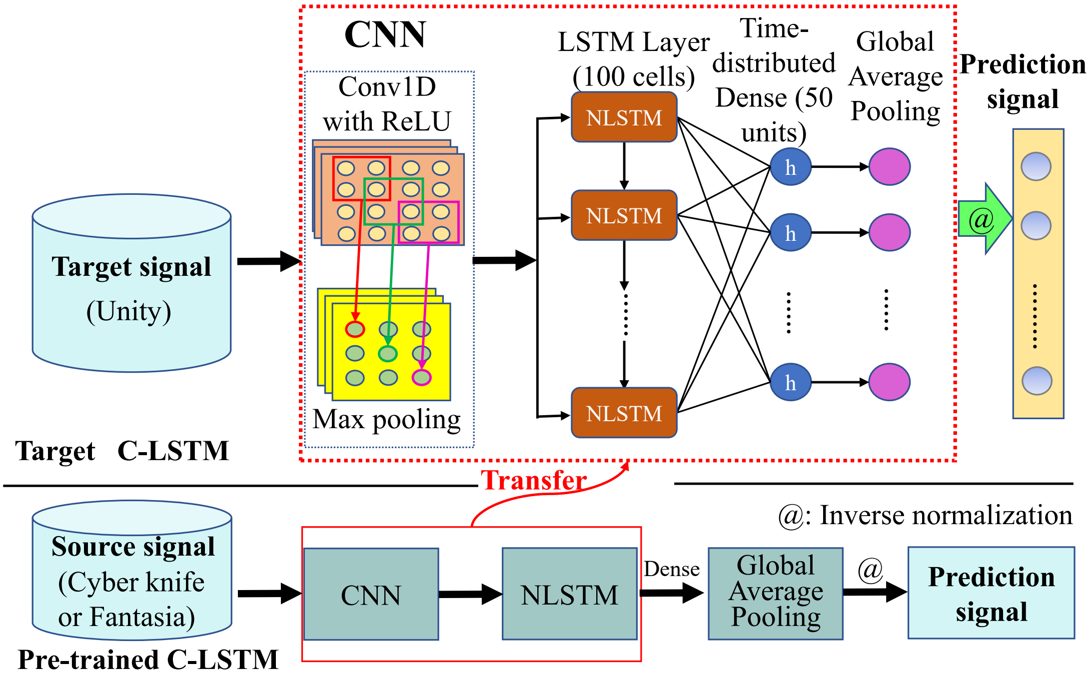

FIGURE 3.3 – Architecture of proposed transfer C-NLSTM framework.

3.2.3 Proposed transfer C-NLSTM framework

The architecture of our transfer C-NLSTM framework is shown in figure 3.3 containing two parts : the pre-trained and target C-NLSTM. The Cyberknife and Fatasia databases were used to evaluate the stability and robustness of the pre-trained C-NLSTM. Its structure and parameters were saved and transferred to the target C-NLSTM network for real-time prediction of tumor movements. The detailed information about the pre-trained C-NLSTM, the target C-NLSTM and the training procedure of the proposed framework is as follows.

1) Pre-trained C-NLSTM : the detailed configurations of C-NLSTM were illustrated in the red dotted box in figure 3.3. The pre-processed data was passed into a 1D-CNN, which effectively extracted the internal structure features of respiration signals. Its output was fed a max pooling to reduce the parameter dimensions and the features learned by the CNN were used as input to the NLSTM. The time-distributed FC layer was connected to the outputs of the NLSTM and a one-dimensional average pooling layer less prone to overfitting than the traditional FC layers.

The detailed structure of C-NLSTM is outlined in Table 3.1. The convolutional layers contain 32 convolution kernels and their receptive fields were 1×8. The NLSTM architecture consisted of 100 cells and its parameter named 'return sequence' was set to 'True', to allow the outputs of all timesteps to be passed into the time-distributed FC layer with 50 units. Lastly, an FC layer was used to predict the respiratory signal. Note that an inverse normalization step was needed to reverse the effects from the aforementioned (figure 3.3) normalization. The C-NLSTM model was pre-trained on the CyberKnife and Fantasia databases.

2) Target C-LSTM : it had the same structure as the pre-trained C-NLSTM. The hyper-parameters, parameters and structures of the pre-trained C-NLSTM model were transferred to the target C-LSTM, whose parameters were then fine-tuned using the Unity database for the specific tumor motion predictions without training the whole network from scratch.

3.2.4 Training procedure

To monitor the risk of overfitting during the training phase, 20% of the training samples were randomly selected from each class of training samples as a validation set. After each training epoch, the accuracy and loss of the validation set were calculated to monitor if the model begins to overfit the training data.

During the training phase, the Adaptive Moment Estimation (Adam)[78] optimizer was used to optimize the loss function due to its adaptability to varying learning rates, effective handling of sparse gradients, robustness to noisy data, and efficient parameter updates [177]. A validation set was used to cross validation to monitor the performance of training and search the optimal hyper-parameters. The following hyperparameters were chosen based on a search conducted by Lombardo et al. [99] : the number of layers from 1, 3, 5, 10, dropout rates from 0, 0.1, 0.2, learning rates from 0.0001, 0.0005, 0.001, 0.005, 0.01, and batch sizes from 16, 32, 64, 128. The optimal hyperparameter settings obtained through cross-validation are presented in Table 3.2.

Table 3.1 – Model structure of FC-NLSTM

Name of the Layer	Parameters
Conv1D	Filters number=32, Kernel size =1×8, Kernel initializer="he uniform", Strides = 1
Maxpooling1D	—
NLSTM	Hidden unit=100, return sequence="True"
Time distributed fully connected	Neurons number = 50
Global Average Pooling1D	—
Fully connected	Neurons number = 2 or 3, Activation = "softmax"

3.2.5 RNN Models

RNNs capture temporal dependencies in data by processing sequences, making them useful for predicting respiratory motion. Gradient vanishing and explosion caused RNNs to lose their grasp on nonlinear relationships. Solutions include Long Short-Term Memory (LSTM), Bidirectional LSTM (Bi-LSTM), and Gated Recurrent Unit Networks (GRUs). A detailed description of the LSTM, Bi-LSTM and GRU and their performance for predicting respiratory motion can be found elsewhere [92][177][190]. The training procedure and hyperparameter selection for these three RNN models are consistent with the C-NLSTM model, as described in Table 3.2.

TABLE 3.2 – Hyper-parameter configuration

Configuration	Value
Optimization function	Adam
Epoch	100
Batch size	64
Learning rate	0.001
Loss function	categorical crossentropy
ReduceLROnPlateau	monitor = “val loss”, factor = 0.1, patient = 3, min delta = 0.0001
EarlyStopping	monitor = “val loss”, patient = 10
ModelCheckpoint	monitor = “val loss”, mode = “auto”, period = 1

3.3 Materials and methods

3.3.1 Public respiratory databases

The first public database used in the study was the CyberKnife at Georgetown University Hospital by Dr. Kevin Cleary and Dr. Sonja Dieterich [36]. It contained breathing recordings of 103 patients with a total of 306 respiratory motion traces. All patients had malignant tumor manifestations in the lung. Respiratory data for each patient were recorded with three fiducial markers (optical tracking devices with a 26Hz sampling rate) to track chest movements. The recording time varied from 25 to 132 minutes. The data used in this study were the selected 137 traces from the database (all patients were included) with the best respiration patterns. This database was used to both verify the prediction ability of the C-NLSTM model, and initialize the transfer-C-NLSTM model. The CyberKnife database can be downloaded from the site [1].

The second database was the Fantasia database from the Hebrew Rehabilitation Center for Aged (Boston 02131, USA) [66]. Twenty young (21-34 years old) and twenty elderly (68-85 years old) rigorously-screened healthy subjects underwent 120 minutes of continuous supine resting while continuous electrocardiographic (ECG), and respiration signals were collected. All subjects remained in a resting state in sinus rhythm while wat-

---

[1] `https://signals.rob.uni-luebeck.de/index.php/Signals_@_ROB`

ching the movie Fantasia (Disney, 1940) to help maintain wakefulness. The continuous respiration signals were digitized at 250 Hz. This database was used to : 1) validate the C-NLSTM model again (training and testing), 2) validate the Transfer-C-NLSTM model initialized with the Cyber-Knife database, 3) initialize the Transfer-C-NLSTM model to be tested on the Unity database. The Fantasia database can be downloaded from the site[2].

3.3.2 Unity database

A Unity database was established in Section 2.3.1, which included the orthogonal 2D cine-MRI with 5Hz sampling frequency of 10 lung cancer and 10 liver cancer patients in both coronal and sagittal slices. The MRI-Linac allows real-time acquisition of three orthogonal planes (coronal, sagittal, and transverse), with motion in the Left-Right (LR) and Superior-Inferior (SI) directions measured from coronal slices, and motion in the Anterior-Posterior (AP) direction derived from sagittal slices. Experienced radiologists delineated the Gross Tumor Volume (GTV) and Organs at Risk (OAR), enabling the extraction of tumor trajectories in the SI, AP, and LR directions.

Unlike for lung cancer patients, the movements of the liver centroid were used instead of those of the tumor, since the liver is not highly compressible but a solid organ while the tumor borders are extremely difficult to identify. The gross tumor volumes (GTVs) of lung patients (Figure 3.4(a)) and liver organ of liver patients (Figure 3.4(c)) were outlined by an experienced radiologist, and then their trajectories (Figure 3.4(b) and Figure 3.4(d)) in three directions of the tumor/liver boundary were extracted from the MRI cine.

3.3.3 Data interception

The data intercepting is outlined in figure 3.5. Raw respiratory signals and trajectories of each patient were divided into training set (70%) and testing set (30%), and 20% of training set were used as the validation set to cross validate and monitor the performance of training and the optimization of the hyper-parameters for RNN models. The inputs and outputs of the predictor were segmented with a sliding window consisting of one pair of input and output data, which were denoted as x_i and y_i. The successive input $x_{(i+1)}$ was generated by moving the sliding window by 1 sample forward, and the sliding window was moved forward until the last available observation in the training part was hit. The length

---

[2] `https://physionet.org/content/fantasia/1.0.0/`

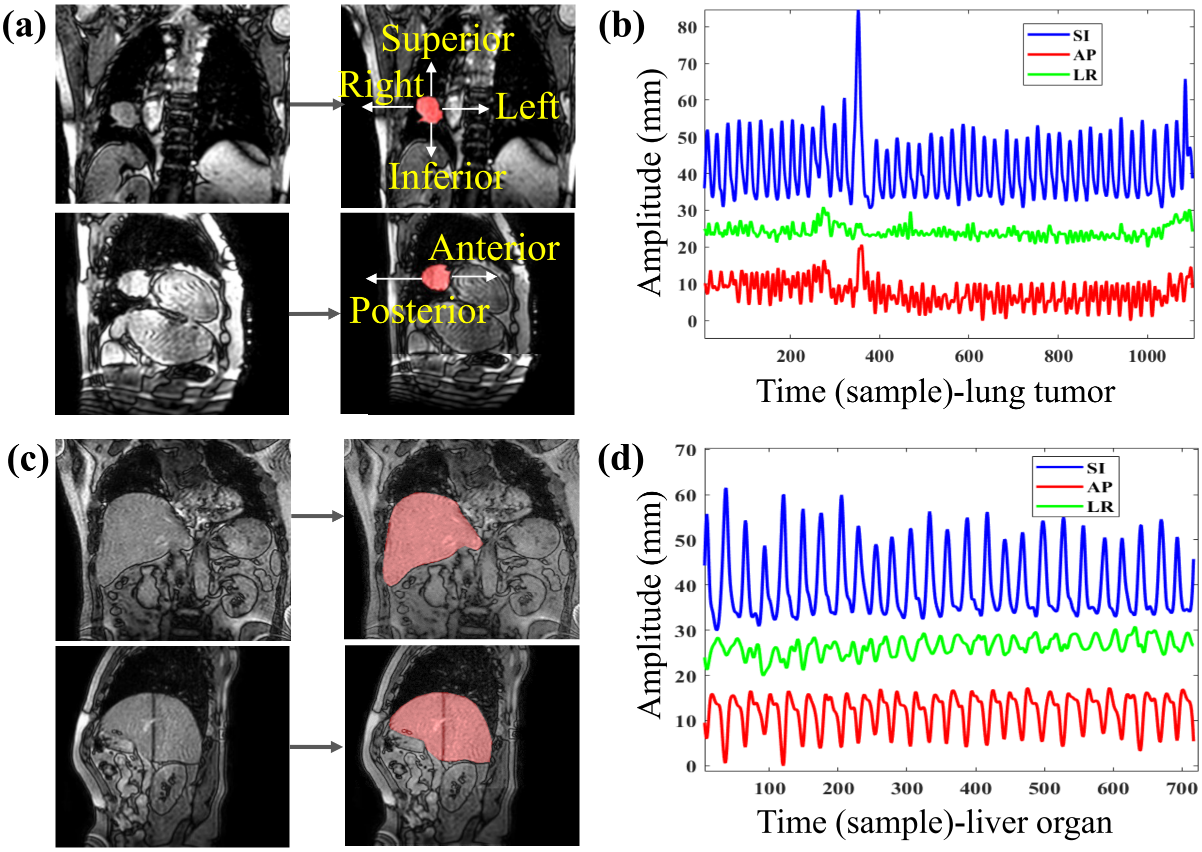

FIGURE 3.4 – (a) Labeled lung tumor in coronal and sagittal slices. (b) Tumor centroid trajectories in three directions. (c) Labeled liver organ in coronal and sagittal slices. (d) Liver centroid trajectories in three directions.

of each x_i represents the number of samples used to make prediction, this parameter may lead to different prediction results. To match pre-training and target training data, traces from the Cyberknife database and Fantasia database were down-sampled to 5Hz. For these three database, we fixed m=15 samples (about 3 seconds) in this study. The length of y_i was determined by the prediction window. Since the sampling period was 0.2 s, each $\mathrm{y}_i = [\mathrm{y}_{((i,1))}, \mathrm{y}_{((i,2))}, \mathrm{y}_{((i,3))}]$ contained future samples of 0.2, 0.4 and 0.6 s respectively, and their estimations were noted as $\widehat{y}_i = [\widehat{y}_{(i,1)}, \widehat{y}_{(i,2)}, \widehat{y}_{(i,3)}]$. In this study, since the system delay was 0.5 seconds while the MRI sampling period was 0.2 seconds, we fixed the prediction window length to be 0.6 seconds.

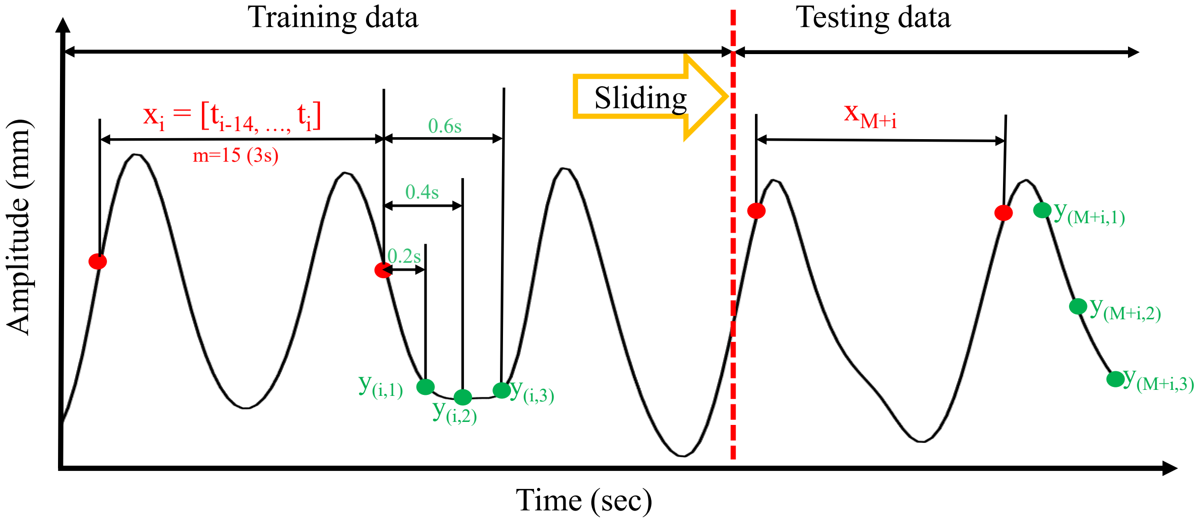

FIGURE 3.5 – Data intercepting of the respiratory signal. The breathing curves in the training.

3.3.4 Performance evaluation

The mean absolute error (MAE) [181] is the mean absolute difference between the predicted and observed values defined by :

$$\mathrm{MAE} = \frac{1}{N} \sum_{i=1}^{N} |y_i - \widehat{y}_i|, \tag{3.4}$$

where y_i and $\widehat{y}_i$ are the actual and predicted respiration data respectively, and N the number of total points.

The root mean square error (RMSE) [25] [64]is a measure of accuracy, to compare forecasting errors of different models for a particular dataset and not between datasets, as it is scale-dependent. RMSE is the most commonly used accuracy measure and is defined as :

$$\mathrm{RMSE} = \sqrt{\frac{1}{N}\sum_{i=1}^{N}(y_i - \widehat{y_i})^2} \tag{3.5}$$

Normalizing the RMSE (nRMSE) [115] facilitates the comparison between datasets or models with different scales. Though there are no consistent means of normalization in the literature, common choices are the mean or the range (defined as the maximum value minus the minimum value) of the measured data. This value is commonly referred to as the nRMSE, and often expressed as a percentage, where lower values indicate less residual variance. In many cases, especially for smaller samples, the sample range is likely to be affected by the size of the sample which would hamper comparisons. nRMSE is defined as :

$$\mathrm{nRMSE} = \frac{\mathrm{RMSE}}{\sigma} = \frac{\mathrm{RMSE}}{\sqrt{\frac{1}{N}\sum_{i=1}^{N}(y_i - \overline{y})^2}}, \tag{3.6}$$

where the $\overline{y}$ is the mean of the actual data points.

3.3.5 Experiment

Firstly, the accuracy and robustness of the proposed C-NLSTM model was validated with the CyberKnife database and Fantasia database, and compared with traditional methods (ARIMA and RFR) as well as RNN models that without CNN. Then, the proposed transfer C-NLSTM model was used to predict the tumor motion curves from the Unity database. In addition, to compensate for the lack of patients in the Unity, we intercepted the first two minutes of respiratory signals of each patient from Fantasia database as a training set and the rest as a test set to verify the performance of Transfer C-NLSTM. The MAE, RMSE, and nRMSE were the amplitude metrics used to evaluate and compare the performance of models. All experiments were conducted using Keras API with the TensorFlow backend and were executed on an Intel 4-core 2.4-GHz CPU, a NVIDIA GeForce GTX1660 Ti GPU, 512 GB SSD and 20 GB RAM machine.

3.4 Results and Discussion

3.4.1 Results from CyberKnife and Fatasia

The average MAE, RMSE, and nRMSE results of 10 different models on the 137 traces from CyberKnife were shown in Table1 3.3 with the prediction window set to 0.6 seconds. In general, the performance of the RNN with CNN models were better than those without. The C-NLSTM model achieved the best performances in predicting the movement of external signals with an MAE of 0.178mm, an RMSE of 0.262mm, and an nRMSE of 0.036 (no unit).

Table 3.3 – Comparison of various methods for 103 patients from CyberKnife

Model	MAE(mm)	RMSE(mm)	nRMSE(no unit)
ARIMA	0.309	0.393	0.062
RFR	0.284	0.388	0.058
GRU	0.263	0.364	0.050
LSTM	0.266	0.366	0.050
Bi-LSTM	0.276	0.377	0.053
NLSTM	0.245	0.341	0.047
C-GRU	0.186	0.270	0.038
C-LSTM	0.191	0.280	0.039
C-Bi-LSTM	0.189	0.276	0.039
C-NLSTM	0.178	0.262	0.036

For the Fantasia database, we utilized 70% of the data for training and 30% for testing to reconfirm the performance of the C-NLSTM model. When the prediction window was set to 0.6 seconds, the average MAE, RMSE, and nRMSE results for 40 patients across various models are presented in Table3.4. Consistent with our observations, the RNN model with CNN outperformed those without CNN, and the C-LSTM model exhibited the best performance in predicting respiratory motion. Specifically, its MAE, RMSE, and nRMSE were 0.085 adu/mV, 0.233 adu/mV, and 0.024 (no units), respectively.

Again, using the Fantasia database, when only 2 minutes of data were used for training, the Cyberknife-based Transfer-C-RNN model significantly outperformed the non-transferred model, as shown in Table3.5. Compared to the C-NLSTM model, the Transfer-C-NLSTM achieved average reductions of 22.1%, 21.9%, and 28.9% in MAE, RMSE, and nRMSE, respectively.

Table 3.4 – Comparison of various methods for 40 patients from Fantasia

Model	MAE(adu/mV)	RMSE(adu/mV)	nRMSE(no unit)
ARIMA	0.159	0.419	0.059
RFR	0.120	0.324	0.032
GRU	0.109	0.217	0.029
LSTM	0.104	0.213	0.028
Bi-LSTM	0.109	0.222	0.029
NLSTM	0.105	0.249	0.029
C-GRU	0.087	0.234	0.025
C-LSTM	0.089	0.239	0.025
C-Bi-LSTM	0.090	0.235	0.025
C-NLSTM	0.085	0.233	0.024

Table 3.5 – Comparison of model w/o transfer learning for 40 patients from Fantasia

Model	MAE(adu/mV)	RMSE(adu/mV)	nRMSE(no unit)
C-GRU	0.143	0.399	0.053
C-LSTM	0.131	0.352	0.045
C-Bi-LSTM	0.130	0.337	0.043
C-NLSTM	0.146	0.350	0.045
Transfer-C-GRU	0.105	0.274	0.032
Transfer-C-LSTM	0.110	0.308	0.039
Transfer-C-Bi-LSTM	0.107	0.292	0.036
Transfer-C-NLSTM	0.102	0.275	0.032

3.4.2 Results from the Unity

Figure 3.6 shows the comparison of 4 RNN models w/o the transfer learning for the Unity database. For the 10 lung cancer patients, the transfer-C-NLSTM based on trained parameters from history database achieved the best performances, with average MAE, RMSE, and nRMSE of 0.85mm, 1.18mm, and 0.21 (no unit) in the SI directions, with average MAE, RMSE, and nRMSE of 0.45mm, 0.59mm, and 0.29 (no unit) in the AP directions, with average MAE, RMSE, and nRMSE of 0.36mm, 0.48mm, and 0.34 (no unit) in the LR directions, respectively. Comparing with the transfer-C-NLSTM and C-NLSTM, the average nRMSE decreased by 54.3%, 42.0%, and 30.6% in the SI, AP and LR direction, respectively. Those figures demonstrated the benefits of transfer learning paradigm, particularly efficient with moderate target database volumes.

The same can be observed on the transfer-C-NLSTM for the 10 liver cancer patients, with average MAE, RMSE, and nRMSE of 0.88mm, 1.22mm, and 0.16(no unit) in the SI directions, with average MAE, RMSE, and nRMSE of 0.47mm, 0.66mm, and 0.23 (no unit) in the AP directions, with average MAE, RMSE, and nRMSE of 0.54mm, 0.75mm, and 0.23 (no unit) in the LR directions, respectively. Comparing the transfer-C-NLSTM to C-NLSTM, the average nRMSE decreased by 48.4%, 41.0%, and 43.9% in the SI, AP and LR direction, respectively. Those figures demonstrated the benefits of transfer learning paradigm, particularly efficient with moderate target database volumes.

3.4.3 Discussion

This chapter introduces a Transfer-C-NLSTM framework designed for real-time prediction of tumor respiratory motion trajectories based on 2D Cine-MRI. Experimental results on the CyberKnife and Fantasia databases demonstrate that the C-NLSTM model excels in predicting the motion of external signals. Its relatively low average MAE, RMSE, and nRMSE scores indicate high accuracy and robustness in handling respiratory motion prediction. Furthermore, the RNN model with CNN consistently outperforms other models, highlighting the advantage of convolutional neural networks in extracting internal structural features from respiratory signals. This provides strong support for the application of deep learning models in predicting tumor motion trajectories.

Additionally, the introduction of transfer learning techniques has played a crucial role in enhancing the model's performance. Experiments conducted on the Fantasia database demonstrate that the Cyberknife-based transfer C-RNN model outperforms the

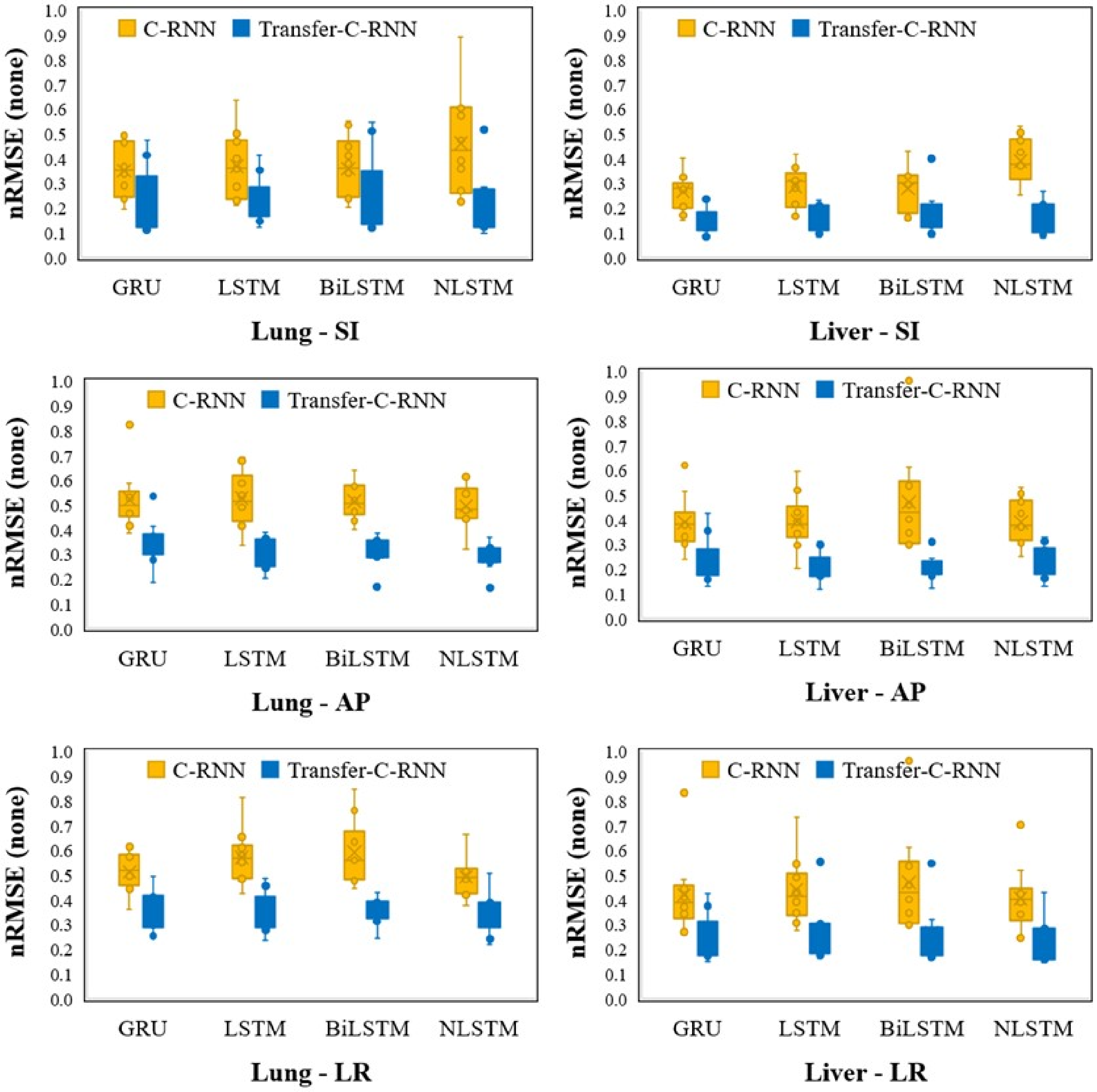

FIGURE 3.6 – Comparison of model w/o transfer learning for 10 lung cancer patients and 10 liver cancer patients.

non-transfer model, reducing average MAE, RMSE, and nRMSE. This indicates that pre-training on one database and then transferring the learned knowledge to another can effectively shorten model training time, improve performance, and exhibit significant advantages when training data are limited.

The experimental results on the Unity database further validate the benefits of transfer learning. Among the four RNN models compared w/o transfer learning, the transfer C-NLSTM performs the best, enhancing predictive capability. For lung and liver cancer patients, the average nRMSE of transfer C-NLSTM in the SI, AP, and LR directions decreased by 54.3%, 42.0%, and 30.6%, as well as 48.4%, 41.0%, and 43.9%, respectively, demonstrating the significant advantage of transfer learning in addressing limited target data issues.

The ultimate goal of this paper is to real-time predict and compensate for motion induced by respiratory activity during tumor radiotherapy to guide the implementation of gating schemes. There are two limitations in this chapter's research : 1) For deep learning methods, the Unity database containing 2D cine-MRI with tumor motion trajectories still lacks in terms of patient quantity and data collection duration. 2) This chapter aims to evaluate the accuracy of Recurrent Neural Networks (RNN) and its extended models in respiratory motion prediction tasks. However, the proposal of tumor motion trajectories involves manual delineation and extraction based on manually outlined GTV and OARs. Manual labeling of GTV and OAR on motion monitoring images is time-consuming and only applicable for current concept validation studies, not suitable for real-time clinical applications.

To address these issues, in Chapter 4, we will explore the predictive capabilities and efficiency of linear regression, a simpler and more effective method than deep learning, for predicting tumor motion based on specific patient data. We will propose a method for precise prediction of gating signals. In Chapter 5, we will integrate tumor tracking and prediction, constructing an end-to-end gating signal prediction system to enhance the accuracy of MR-guided Radiotherapy (MRgRT) in liver and lung cancer.

3.5 Conclusion

This chapter proposed a transfer C-NLSTM framework for real-time prediction of tumor respiratory motion in 2D cine-MRI. First, a novel C-NLSTM model was constructed, utilizing convolutional neural networks to extract internal structural features of respiratory signals and exploring temporal dependencies within NLSTM. The effectiveness of deep learning in predicting respiratory signals at a 5Hz sampling rate was assessed. Secondly, we introduced the transfer C-NLSTM framework, training the pre-trained model using historical data and optimizing it with 2 minutes of the Unity data, confirming the framework's effectiveness. The study results demonstrated that transfer learning significantly improves model performance when training data is limited. Therefore, our approach offers a viable solution for real-time respiratory motion prediction in MRgRT, crucial for achieving automatic gating, especially in the case of patient free-breathing, which is essential for enhancing the accuracy of thoracoabdominal tumor treatment.

Chapitre 4

REAL-TIME GATING CONTROL FOR RESPIRATORY MOVEMENT COMPENSATION WITH PREDICTION

4.1 Introduction

The gating signal is a binary control signal to allow radiation delivery only when the target moves into a predefined range, known as the 'gating window', specific to each patient. The gating scheme is an algorithm that generates the gating signal and it relies typically on the monitoring of patients' respiration, either with external markers or imaging modalities. Therefore, the accuracy of gating signals plays a crucial role in compensating for respiratory motion during radiotherapy [44][126]. The Elekta Unity provides an unprecedented opportunity for the development of gating schemes with its direct imaging of tumors and internal structures without the need for implanted fiducial markers and/or external respiratory signals for target localization [129][49].

However, achieving real-time acquisition of the 3D target volume remains an unsolved problem due to the balance spatial and temporal resolutions. Research reports indicated [145] that by acquiring interleaved orthogonal slices (sagittal and coronal) at a sufficiently high frequency (4-8 Hz), it becomes possible to reconstruct the 3D tumor trajectory. The retrospective division of raw data according to a quasi-periodic respiratory signal can be done in two fundamentally different ways : either based on the actual respiratory phase (also known as time-based gating) or based on the actual amplitude. In the former, each respiratory cycle is divided into a fixed number of gates from one inspiration maximum to the next, while in the latter, the gates are defined by the absolute amplitude of the respiration signal. It was shown that amplitude-based gating performed superior to phase-based gating, as irregularities in breathing depth are better resolved when analyzing amplitudes instead of phases [18]. In this study, we adopted an amplitude-based gating signals.

To compensate for the system latency in the Elekta Unity, real-time prediction of the tumor's position and critical internal structures is crucial [89]. Klüter et al. [80] reported a latency range of 300 milliseconds to 436 milliseconds for the Co60 version of MRIdian when using gating, while Uijtewaal et al. [169] reported a latency of 330 milliseconds for MLC tracking on the Elekta Unity. However, Lamb et al. [86] reported an overall system latency of within 0.5 seconds for gating, including image acquisition time, contour-based target motion tracking highly variable, and beam on/off trigger time. In this study, we have fixed the total system latency of the Unity gating scheme at 0.5 seconds, although this may not necessarily represent the latest technological advancements in MRgRT under ideal conditions.

There are a number of alternative methods for predicting the trajectory of respiratory movements. Linear filters and their generalization have been largely used [83][116][134]. Probabilistic frameworks, including Bayesian inference [133], Kalman filters [148] and particle filters have also been widely proposed in several studies. More innovative and complex techniques such as support vector regression [83][38], neural networks [116][117][103] and Recurrent neural networks (RNN) [92][177] have been explored for respiratory motion prediction and have demonstrated their effectiveness. In a recent review focusing on the primary prediction filters mentioned above, linear approaches were found to be sufficiently effective in prediction compared to more complex methods when using respiratory signals collected during Cyber-knife treatment [68].

However, it should be noted that directly applying prediction methods developed for respiratory signals to MRI-derived respiratory signals might have some pitfalls due to the differences in imaging modalities (i.e., interleaved orthogonal slices instead of stereo X-ray images) and longer acquisition periods (e.g., $150 - 380$ ms instead of 30 ms for X-ray fluoroscopy [151]), as well as overall system latencies (up to 500 ms [86]) to compensate for. Hence, it is crucial to validate the suitability of these prediction filters for internal organ or tumor position obtained from the 2D MRI cine data, extending beyond just abdominal or thoracic superficial amplitudes.

To address the aforementioned challenges, this study proposes an online gating signal prediction scheme to enhance the accuracy of MRgRT for both liver and lung cancer. Figure 4.1 illustrates the workflow for optimal gating signal prediction.

The key contributions can be summarized as follows :

1. We proposed an online gate signal prediction scheme and validated the effectiveness

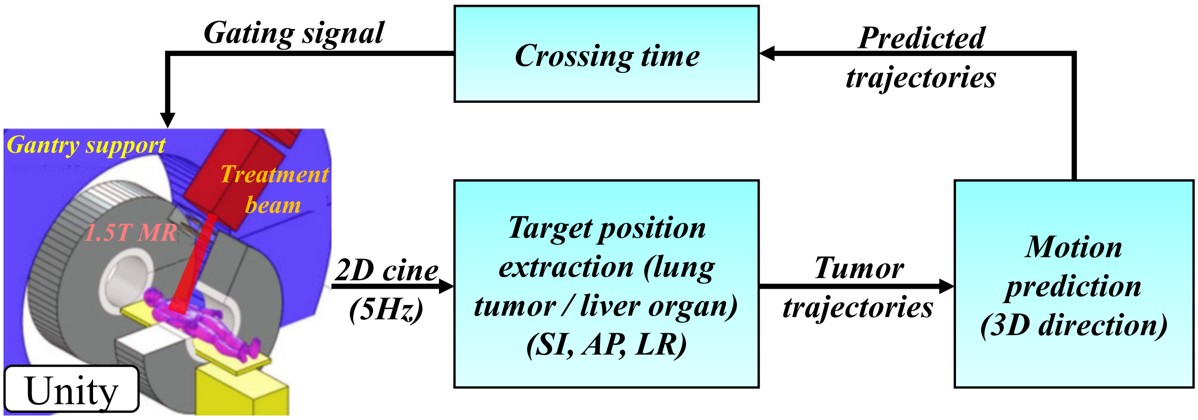

FIGURE 4.1 – Flow chart of gating signals prediction for radiotherapy.

of linear regression for predicting internal organ or tumor motions with 2D MR cine. We compared the linear regression model to three state-of-the-art RNN models, using temporal metrics to assess the accuracy of the generated binary gate signals.

2. We verified the ALR model for patient-specific model training, using the data from the first 30 seconds of each patient as the training set, and updating the model parameters during online prediction.

3. We proved that under the assumption of a 0.5-second system latency, a 0.6-second prediction window (over-prediction) is more suitable than that of a 0.4-second (under-prediction).

4.2 Proposed gating signals prediction algorithm

4.2.1 Linear predictors

The intercepted data is used to predict the motion trajectory of the tumour. The linear regression (Linear) models assume the linear relationship between the future data ($\widehat{y}_{(i,j-1)}$ and $\widehat{y}_{(i,j)}$) and the past available data x_i :

$$\begin{cases} \widehat{y}_{(i,j-1)} & = x_i^T \beta_{j-1} \\ \widehat{y}_{(i,j)} & = x_i^T \beta_j \end{cases} \tag{4.1}$$

where ^{T} denotes the transpose, the coefficient vector defined as $\beta_j = (\beta_{j1}, ..., \beta_{jm})$ for $m = 15$ and $j = 2$ for prediction window of 0.4s or $j = 3$ for prediction window of 0.6s, note that this rule applies to all j in the following.

The loss function of linear regression is the sum of the squares residuals :

$$\begin{cases} L(\beta_{j-1}) = \sum_{i=1}^{N}(y_{(i,j-1)} - x_i^T\beta_{j-1})^2 \\ L(\beta_j) = \sum_{i=1}^{N}(y_{(i,j)} - x_i^T\beta_j)^2 \end{cases} \tag{4.2}$$

For RidgeCV regression, the loss function to be minimized is the penalized residual sum of squares [61] :

$$\begin{cases} L(\beta_{j-1}) = \sum_{i=1}^{N}(y_{(i,j-1)} - x_i^T\beta_{j-1})^2 + \lambda\|\beta_{j-1}\|_2^2 \\ L(\beta_j) = \sum_{i=1}^{N}(y_{(i,j)} - x_i^T\beta_j)^2 + \lambda\|\beta_j\|_2^2 \end{cases} \tag{4.3}$$

where the optimal parameter λ is found by the Leave-One-Out cross-validation (LOOCV). The regularization term shrinks the magnitude of the coefficient vector β, which leads to a reduction of the noise level of the prediction signal [57]. $L(\beta)$ is minimized by

$$\begin{cases} \beta_{j-1} = (X^TX + \lambda I)^{-1}X^TY_{j-1} \\ \beta_j = (X^TX + \lambda I)^{-1}X^TY_j \end{cases} \tag{4.4}$$

where X=$[x_1, ..., x_N]^T$, $Y_j = [y_{(1,j)}, ..., y_{(N,j)}]^T$. Note that the calculations of these coefficients are straight forward without an iterative process and its convergence criterion to fix.

For the L2-L1 regression, the L1-norm of the parameters is used as the penalty term in the loss function [164] :

$$\begin{cases} L(\beta_{j-1}) = \sum_{i=1}^{N}(y_{(i,j-1)} - x_i^T\beta_{j-1})^2 + \lambda\|\beta_{j-1}\|_1 \\ L(\beta_j) = \sum_{i=1}^{N}(y_{(i,j)} - x_i^T\beta_j)^2 + \lambda\|\beta_j\|_1 \end{cases} \tag{4.5}$$

where the optimal λ is chosen by the generalized cross-validation (GCV) [50], and the optimal solution $\beta(\lambda)$ is obtained by the alternating direction method of multipliers (ADMM) [14].

Due to the lower complexity of linear regression methods, we also implemented and evaluated the *adaptive linear regression* with a burn-in period of the first 30 s (150 samples) for each patient. The minimization of $L(\beta)$ is performed continuously to update the model parameters (β_{j-1} and β_j) with the incoming data of the same patient. Recursive update expressions for the inverse matrix $[X^TX]^{-1}$ are derived from Woodbury's constant equation, eliminating the need to recompute existing information to improve the speed of the algorithm [59]. The algorithm table 1 describes in detail the process of the adaptive linear regression for the gating signal generation.

4.2.2 Crossing time

The "Crossing time" refers to the time instant (either by prediction or by interpolation) that tumor crosses a predefined threshold. When the tumor crosses below the predefined threshold, the radiation beam is activated and it is referred to as 'crossing-on'. Conversely, when the tumor crosses above the threshold, the radiation beam is deactivated and it is termed as 'crossing-off'.

Since the sampling frequency of MR images is 5Hz, it is reasonable to assume that the shape of the respiratory curve can be restored by connecting each frame of the continuous images. Therefore, we proposed a linear interpolation to predict the threshold crossing time :

$$\widehat{T}_{\text{cross}} = \frac{\text{Th} - \widehat{y}_{(i,j)}}{\widehat{y}_{(i,j)} - \widehat{y}_{(i,j-1)}} \times \triangle T + T_i + j \times \triangle T, \tag{4.6}$$

where T_i is the current sample time, $\widehat{y}_{(i,j-1)}$ and $\widehat{y}_{(i,j)}$ the predictions by Eq.(4.1), $\triangle T = 0.2$s the MRI sampling period, and Th the threshold, set as the average of the respiratory trajectory in the SI direction during the burn-in period for simplicity. Note that a lower threshold means beaming during the more stagnant phase of exhalation and thus ensures better treatment margins while increasing the overall treatment time. The optimal trade-off between radiation precision and efficiency is beyond the scope of the present study. The reference crossing time (gold standard) could be calculated in a similar manner with Eq.4.6, using $y_{(i,j-1)}$ and $y_{(i,j)}$ instead of their predictions.

4.2.3 Gating signals generation

Figure 4.2 shows the gating control scheme by thresholding the predicted tumor trajectory for prediction window of 0.6 s. The black and red curves are true and predicted breathing curves, respectively. The green line is threshold that was set according to the range of tumor motion and dutycycle. The system latency was 0.5 s in this study, thus ideal gating signal should be 0.5 s earlier than that the exact crossing time. In the experiment, taking the 0.6 s prediction window ($j = 3$) as an example, there are two conditions

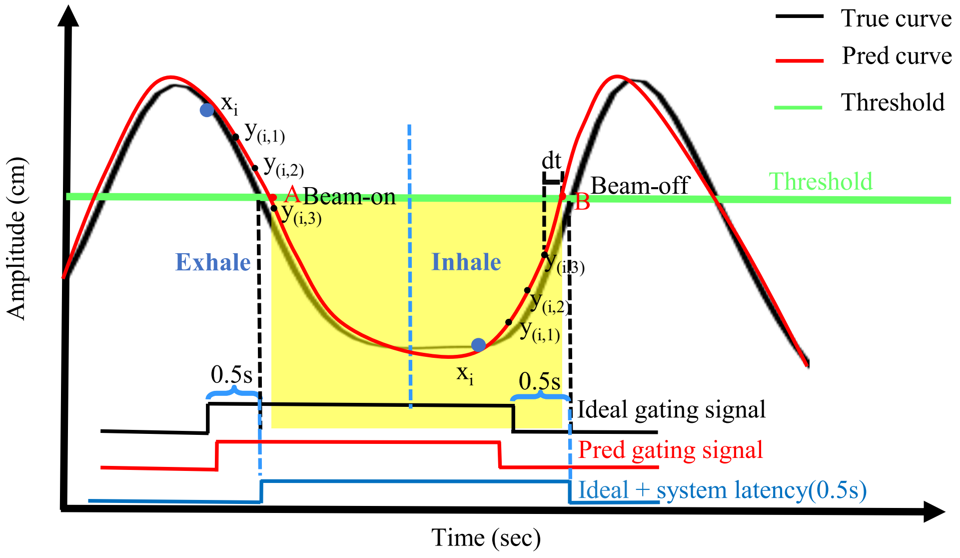

FIGURE 4.2 – Gating control scheme by thresholding the predicted tumor trajectory for prediction window of 0.6 s.

for triggering gating : 1) when the motion curve crosses the threshold between $\widehat{y}_{(i,2)}$ and $\widehat{y}_{(i,3)}$ (point A in Figure 4.2), or 2) when the time difference (dt) between $\widehat{y}_{(i,3)}$ and the predicted cross time is less than 0.1s (point B in Figure 4.2). For the prediction window of 0.4s ($j = 2$), the same decision rules apply except that $\widehat{y}_{(i,2)}$ and $\widehat{y}_{(i,3)}$ are replaced by $\widehat{y}_{(i,1)}$ and $\widehat{y}_{(i,2)}$. The black and red binary control signals were generated by the reference and predicted crossing time respectively, while the blue one can be generated without prediction thus giving the worst-case scenario in gating schemes. The algorithm table 1 describes in detail the above gating signal generation rules as well as idea of adaptive (and patient-specific) gating signal generation with an ever-increasing training data set.

Moreover, for the evaluation of gating schemes, we also studied some temporal metrics. The best performance is reached when the predicted gating signal coincides perfectly with the ideal one. Note that it is quite different from the amplitude measure for respiration trace prediction errors. On the other hand, the worst performance is given by ideal gating delayed by the latency (0.5 s), as can be determined after the exact crossing time without the prediction at all. Figure 4.2 also illustrates the ideal (in black) and dummy (in blue) gating signals, the former is generated by the exact threshold crossing instants less the system delay (best scenario supposing perfect prediction of the future motions), while the latter simply its delayed version (0.5s) and can be achieved without prediction in practice. We thus considered any meaningful gating signal to be constrained within the

0.5 s temporal interval.

4.3 Materials and methods

4.3.1 Data acquisition

We utilized the Unity database constructed in Section 2.3.1, collecting 2D cine-MRI data from a total of 20 cancer patients, including 10 liver cancer patients and 10 lung cancer patients. The GTVs of lung patients (Figure 4.3(a)) and liver organ of liver patients (Figure 4.3(c)) were outlined by an experienced radiologist, and then their trajectories (Figure 4.3(b) and Figure 4.3(d)) in three directions of the tumor/liver boundary were extracted from the MRI cine. In amplitude-based gated radiotherapy, we combined the motion from these three different directions into a 3D vector called "total motion". This approach computed SI, AP, and LR displacements as the length of a 3D vector, ensuring a holistic consideration of motion. And it allowed specific gating thresholds to be set based on the amplitude of total tumor motion for each patient, helping to simplify treatment planning and reduce motion-related complexity. Table 4.1 shows the mean amplitude of motion and the min-max range (in millimeters), along with the mean respiratory cycle and the min-max range (in seconds) for liver organ and lung tumors.

Table 4.1 – Movement characteristics of liver organs and lung tumors. Mean amplitude of motion and (min-max) range in millimeters, and mean respiratory cycle and (min-max) range in seconds.

	SI (mm)	AP (mm)	LR (mm)	3D motion (mm)	Period (s)
Liver organ	21.3 (5.6-40.1)	7.9 (3.2-13.1)	9.3 (4.3-15.9)	25.5 (14.5-43.2)	4.6 (2.9-7.4)
Lung tumor	16.2 (3.1-25.2)	4.2 (2.8-5.9)	2.8 (0.9-4.5)	17.2 (5.1-25.5)	3.4 (2.4-5.4)

4.3.2 Data interception

Trajectory of each patient was divided into training set (70%) and testing set (30%), and 20% of training set was used as the validation set to cross-validate and monitor the performance of training and the optimize of the hyper-parameters for Ridge regression, L2-L1 regression and RNN models. The inputs and outputs of the predictor were segmented with a sliding window consisting of one pair of input and output data, denoted as x_i and

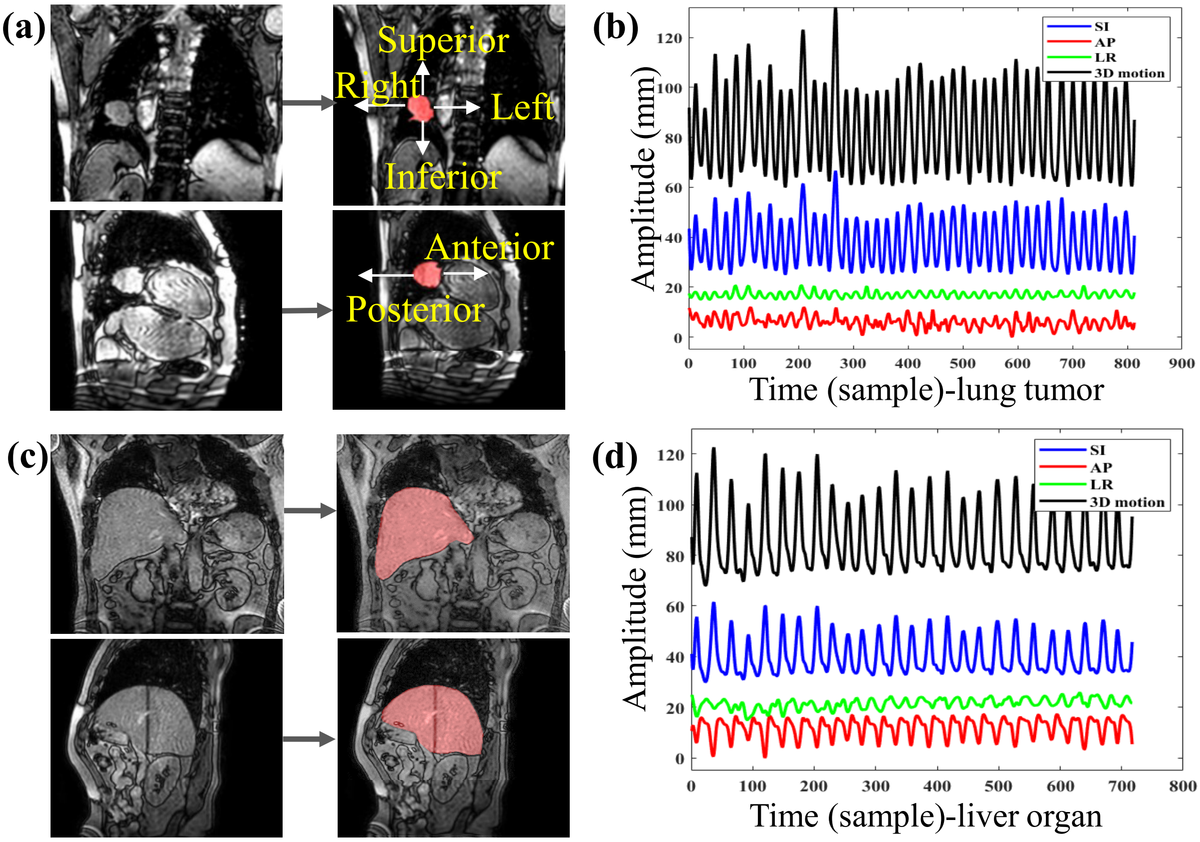

FIGURE 4.3 – (a) Labeled lung tumor in coronal and sagittal slices. (b) Tumor centroid trajectories in three directions and 3D motion. (c) Labeled liver organ in coronal and sagittal slices. (d) Liver centroid trajectories in three directions and 3D motion.

y_i. The successive input $x_{(i+1)}$ was generated by moving the sliding window by 1 sample forward, and the this was repeated until the last available sample in the training part. The length of each x_i represents the number of samples used to make prediction, we fixed m=15 (about 3 s) in this study. The length of y_i was determined by the prediction window. Since the sampling period was 0.2 s, each $y_i = [y_{(i,1)}, y_{(i,2)}, y_{(i,3)}]$ contained future samples of 0.2, 0.4 and 0.6 s respectively, and their estimations were noted as $\widehat{y_i} = [\widehat{y}_{(i,1)}, \widehat{y}_{(i,2)}, \widehat{y}_{(i,3)}]$. In this study, since the system delay is 0.5 s while the MRI sampling period is 0.2 s, we are confronted with the choice of either 0.4 s (under prediction) or 0.6 s (over prediction) for the prediction window.

4.3.3 Performance evaluation

Amplitude metrics

Amplitude indicators (MAE, RMSE, NRMSE) are introduced in detail in section 2.3.4.

Temporal metrics

For gated radiotherapy, it is essential in predicting accurately the beam on/off control when the target crosses threshold position rather than predicting the respiratory curve itself. We thus propose in this paper two temporal metrics, namely the gating on/off error and gating accuracy in comparison with the ideal gating signal.

We first defined the crossing on/off error as the temporal differences threshold-crossing between the true and predicted curves in both directions. The gating on/off error, on the other hand, denoted the temporal difference of beam-on/off control between the ideal (0.5s in advance of the real threshold-crossing) and the predicted gating signals.

The gating accuracy is the ratio of overlapped duration (of the ideal and predicted gating signal) over the entire therapy :

$$\text{Gating accuracy} = \left[1 - \frac{\sum_{i=1}^{N}(\text{Tgaterr})}{\text{Total time of irradiation}}\right] \times 100\% \tag{4.7}$$

where N is the number of breathing cycle during therapy of each patient and Tgaterr the non-overlapping period of the ideal and predicted gating signal.

4.4 Results and Discussion

4.4.1 Linear vs RNN regression

Predictive performance of linear regression and its regularized variants (Ridge and L2-L1) were compared with three classical RNN models and the transferC-NLSTM model proposed in Chapter Three (abbreviated as Ch3). Since RNN requires a large amount of training data, we first use 70% of the data (more than 4 minutes) in these six models for training and the rest for testing.

Table 4.2 shows the mean and standard deviation of amplitude errors (MAE, RMSE, and nRMSE) for different methods with 0.4 s and 0.6 s prediction window for 10 liver cancer patients and 10 lung cancer patients. No matter the choice of prediction length, linear regression without regularization performed the best, followed by the Ridge, and linear methods have significantly smaller amplitude errors than those of the RNNs ($P<0.05$), not to mention the unrealistic $70\% - 30\%$ data partition adopted in favor of the RNNs. Overall, the magnitude-based results demonstrated the excellent predictive power of the linear regression for motion prediction of both liver organ and lung tumors. Note also that as expected in terms of amplitude metrics a shorter prediction window (0.4 s) yields lower prediction errors (MAE, RMSE) and higher correlation (nRMSE) compared with a longer prediction window (0.6 s). However, this phenomenon is not observed when it comes to the temporal metrics for the gating signal errors.

Table 4.3 shows the mean and standard deviation of gating errors with prediction length of 0.4 s and 0.6 s for the same liver cancer patients and lung cancer patients, as well as the calculation time for each model. Indeed, we observed identical crossing and gating errors in the case of over-prediction whereas in the case of under-prediction crossing errors seem to be reduced thanks to its higher precision, gating errors are getting worse since the gating decisions are made typically between 0.2 s and 0.4 s in advance with a system delay of 0.5 s. We thus conclude that over-prediction is a preferable choice compared to under-prediction when system delay is not a multiple of the MRI sampling period.

For the gating accuracy, choosing over-prediction (0.6 s) is significantly better ($P<0.05$) than under-prediction (0.4 s), all factors being equal otherwise. When the prediction window is 0.6 s, the linear regression achieved the best performance with an average gating accuracy of 98.3% and 98.0%, a gating error of 56 ms and 45 ms, for liver cancer and lung cancer patients respectively, as to measured by the dummy performer of 500 ms

TABLE 4.2 – Mean and std deviation of amplitude errors with 0.4 s and 0.6 s prediction window for 10 liver cancer patients and 10 lung cancer patients.

		Liver organs			Lung tumors		
PW	Model	MAE (mm)	RMSE (mm)	nRMSE (None)	MAE (mm)	RMSE (mm)	nRMSE (None)
	Linear	0.86±0.56	1.84±0.84	0.14±0.06	0.60±0.15	1.61±0.64	0.17±0.09
	Ridge	0.90±0.60	1.87±0.87	0.14±0.06	0.60±0.15	1.61±0.64	0.17±0.09
0.4 s	L2-L1	1.41±0.38	2.35±0.66	0.17±0.05	1.26±0.33	2.16±0.54	0.22±0.09
	LSTM	2.51±1.39	3.93±1.67	0.27±0.04	1.87±0.38	2.94±0.56	0.31±0.15
(j=2)	Bi-LSTM	2.26±0.99	3.57±1.09	0.25±0.05	1.70±0.63	2.85±0.75	0.30±0.14
	GRU	2.18±0.92	3.46±1.04	0.24±0.04	1.58±0.46	2.69±0.60	0.28±0.12
	Ch3	1.34±0.83	2.07±0.95	0.19±0.03	1.07±0.28	1.66±0.62	0.23±0.10
	Linear	1.65±0.87	2.11±1.06	0.15±0.07	1.19±0.40	1.55±0.51	0.15±0.05
	Ridge	1.69±0.92	2.16±1.12	0.15±0.07	1.20±0.39	1.56±0.50	0.15±0.06
0.6 s	L2-L1	2.52±0.71	3.29±0.96	0.24±0.05	2.23±0.71	2.85±0.90	0.27±0.09
	LSTM	3.32±1.40	4.36±1.97	0.29±0.06	1.87±0.38	2.94±0.56	0.31±0.15
(j=3)	Bi-LSTM	3.39±1.64	4.56±2.27	0.31±0.10	1.70±0.63	2.85±0.75	0.30±0.14
	GRU	3.50±1.48	4.62±1.98	0.32±0.09	1.58±0.46	2.69±0.60	0.28±0.12
	Ch3	2.29±1.13	2.60±1.32	0.20±0.06	1.55±0.49	2.41±1.21	0.21±0.11

TABLE 4.3 – Mean and std deviation of gating errors with prediction length of 0.4 s and 0.6 s for 10 liver cancer patients and 10 lung cancer patients, as well as calculation time for each model.

		Liver organs			Lung tumors			
PW	Model	Crossing (ms)	Gating (ms)	Gat-acc (%)	Crossing (ms)	Gating (ms)	Gat-acc (%)	Time (ms)
	Linear	30±25	190±27	93.9±2.1	25±28	183±65	91.6±3.3	0.06
	Ridge	32±27	190±30	93.8±2.1	25±29	184±66	91.4±3.3	0.07
0.4 s	L2-L1	58±24	184±46	93.3±2.3	44±29	191±76	90.1±3.9	0.03
	LSTM	75±64	232±141	93.0±4.2	75±52	233±111	90.5±4.7	3.71
(j=2)	Bi-LSTM	73±53	285±261	90.6±9.9	70±52	267±101	90.0±4.8	5.43
	GRU	71±69	283±250	90.5±6.1	47±44	249±107	90.2±4.7	3.36
	Ch3	58±24	184±46	93.3±2.3	44±29	191±76	90.1±3.9	3.21
	Linear	56±33	56±33	98.3±1.0	45±30	45±30	98.0±1.8	0.07
	Ridge	58±33	58±33	98.2±1.1	47±31	47±31	97.8±2.5	0.06
0.6 s	L2-L1	80±50	80±50	97.2±1.2	80±47	80±47	96.4±2.5	0.02
	LSTM	112±85	112±85	96.1±2.6	138±74	138±74	94.7±3.3	4.36
(j=3)	Bi-LSTM	130±101	130±101	96.0±2.7	131±73	131±73	94.7±4.0	7.25
	GRU	112±72	112±72	96.5±2.3	125±80	125±80	95.1±3.4	4.32
	Ch3	75±45	75±45	97.5±1.2	62±47	62±47	97.1±2.5	4.24
	AL (30 s)	44±23	44±23	98.3±0.6	45±31	45±31	98.0±1.7	0.99

Table 4.4 – P-values (Wilcoxon signed-rank test) for prediction window of 0.6 s between different models. $P<0.05$ was considered significant.

Model 1	Model 2	nRMSE	Gat-acc
Linear	Ridge	0.0001	0.0005
	L2-L1	0.0001	0.0001
	LSTM	0.0001	0.0001
	Bi-LSTM	0.0001	0.0001
	GRU	0.0001	0.0001
Adaptive Linear (30 s)	Linear	0.5663	0.5200
	Ridge	0.0013	0.0580
	L2-L1	0.0010	0.0009
	LSTM	0.0010	0.0001
	Bi-LSTM	0.0010	0.0001
	GRU	0.0010	0.0001

without the prediction. Table 4.4 shows the p-values obtained from Wilcoxon signed-rank test pairwise model comparisons with prediction length of 0.6 s.

Performances of the linear regression are significantly higher than those of RNNs in both amplitude metrics (nRMSE) and temporal metrics (Gating accuracy) ($P<0.05$). To address the potential for overfitting in linear regression and ridge regression, we performed cross-validation on each respiratory curve. In cross-validation, the original dataset is divided into two subsets, each of approximately the same size. The model was then trained on one subset and validated on the remaining subset. This process was repeated 2 times, with each subset being used as a validation set once. The performance metrics obtained from each validation were eventually averaged to obtain a final performance evaluation. Although the temporal correlations within the time series data could potentially affect the cross-validation results, it is noteworthy that linear model achieved an average gating accuracy of 98.2% and 97.7% for liver cancer and lung cancer patients, respectively.

4.4.2 Adaptive regression

Due to the lower complexity of linear regression methods, we also implemented and evaluated the idea of training the model with the first 30 s (150 samples) for each patient as the burn-in period and keep adapting the model parameters with the incoming data during the prediction and gating signals generation process. As shown in Table 4.3, the proposed framework with adaptive linear regression achieved convincing performances in real clinical scenarios with an average gating accuracy of 98.3% and 98.0%, a gating error of 44 ms and 45 ms, for liver cancer and lung cancer patients, respectively. The predictive performance of adaptive linear regression is not significantly different from that of non-adaptive linear regression using more than 4 minutes of training data (P>0.05, see in Table 4.4).

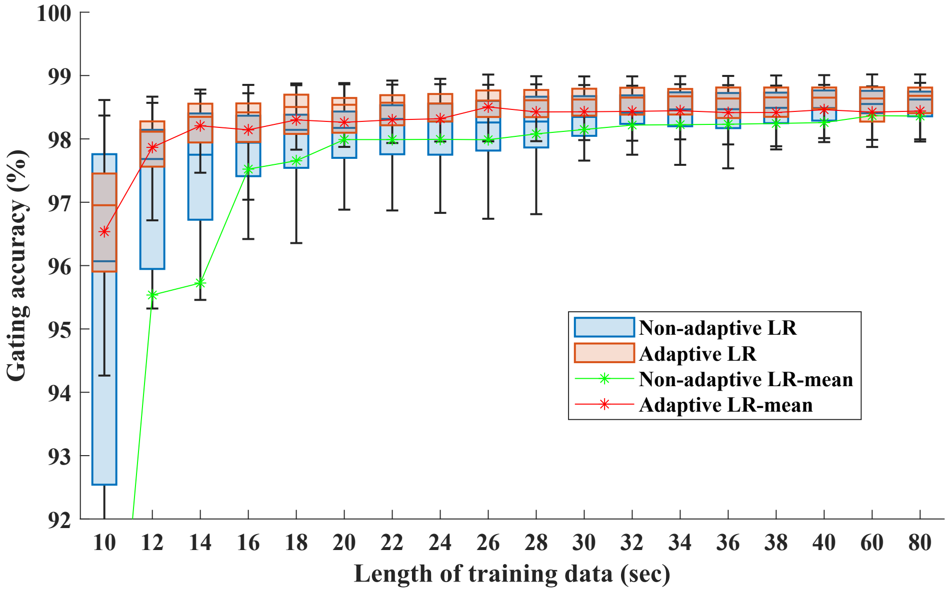

FIGURE 4.4 – Gating accuracy using adaptive/non-adaptive linear regression with different burn-in period.

To verify the minimum number of training data required to train a stable linear regression model, we tested the adaptive and non-adaptive versions with different lengths of training data. The latter had simply fixed model parameters after the training period. Figure 4.4 shows both gating accuracy with different sizes of training data. At the beginning, the gating accuracy increased with the increase of training data, the average gating accuracy of the adaptive version reached 98% at 14 s and tended to increase slowly, while the non-adaptive version reached the stable prediction ability at 32 s. When the training data reached 80 s, the prediction ability of both methods become identical. According to the box plot, when the training data is less than 40 s, the adaptive version is obviously better than the non-adaptive version. For the patient-specific prediction model, the adaptive version can significantly reduce the burn-in time.

4.4.3 Calculation time

All experiments were conducted using the Keras API with the TensorFlow backend and were executed on an Intel 4-core 2.4-GHz CPU, a NVIDIA GeForce GTX1660 Ti GPU, 512 GB SSD and 20 GB RAM machine. The time required to predict the gating signals was calculated for all methods mentioned above (see Table 4.3). For the non-adaptive mode, the calculation time of linear models are less than 0.1 ms and the calculation time of RNN models are between 3 ms and 8 ms. For the adaptive mode, the most time-consuming part was the update of the linear regression predictor, requiring an average of 1 ms, the rest being identical to the non-adaptive mode, i.e. less than 0.1 ms.

Regarding the motion prediction using ALR, the most time-consuming step in Eq. 4.4 is the matrix inverse operation, with a time complexity of $O(mN^2)$. Consequently, the computation time are increasing with the training samples m. To address this, this study derived a recursive update expression for the inverse matrix $[X^T X]^{-1}$ of the matrix $X^T X$ using Woodbury's constant equation [59] without recomputing existing information, significantly improving the speed of the algorithm. As a result, the calculation time for motion prediction takes an average of 1 ms, and the remaining process of generating the 3D gating signal requires less than 1 ms.

4.4.4 Discussion

As observed in several studies [145][169][148][177], the predictive performance decreased with increasing forecasted time span. However, for the 0.4 s and 0.6 s prediction windows, linear regression still achieved sub-resolution accuracy (RMSE < 2.5 mm). The good performance of the linear regression for the 0.6 s prediction window shows that it can successfully account for the system latency found by Glitzner et al. [2] when performing MLC tracking on the Elekta Unity MR linac. As shown in Table 1, the range of respiratory cycles for the 10 lung cancer patients was 2.4 – 5.4 s and the range of 3D movement amplitudes was 5.1 – 25.5 mm ; the range of respiratory cycles for the 21 liver cancer patients was 2.9 – 7.4 s and the range of 3D movement amplitudes was 14.5 – 43 mm. These large ranges show that there are large differences in respiratory movements between each patient and that respiratory movements are patient-specific. Therefore, we proposed to use the first 30 s (burn-in period) of treatment for each patient to train a patient-specific adaptive linear model, which is used for real-time prediction of tumor location during subsequent radiotherapy for that patient and for gating signal generation.

Based on the excellent experimental results, the patient-specific online gating signal prediction scheme based on the linear regression model proposed in this study can be widely applied in MRI-guided radiotherapy for lung and liver cancer.

A recent review study by Jöhl et al. [68] found that a continuously re-optimized (i.e., online) linear regression model performed best on average compared to other motion predictors such as artificial neural networks or Kalman filters. Sharp et al. [148] note the relatively worse performance of the Kalman filter predictor when compared with linear and ANN predictors. In this study, we also compared the traditional methods represented by Kalman filtering with linear regression. Interestingly, our findings consistently indicate that linear regression outperforms Kalman filtering. This may reflect the difficulty in estimating the state transition matrix from such a small amount of data.

Our experimental results on small sample sets verified the excellent performance of linear regression, considerably superior to that of the RNN. The major drawback of classic RNNs is that they are notoriously difficult to train. One important consideration that we addressed within this study is the effect of the non-stationary nature of breathing. Anetai et al. [188] clearly illustrated that the movement and pattern of breathing can easily change individually various. They developed and verified novel respiratory criteria for selecting optimal breathing for gating radiation treatment and defining numerical targets for respiratory gating. For the adaptive linear regression in the study, the predictive parameters were adjusted in real time based on the most recent tumor motion, which may address the issue of respiratory pattern variability. In the current experiment, despite the adaptive regression model continuously increasing its training samples, the average calculation speed is still less than 1ms, as patients' radiotherapy time on the Unity is between $15 - 20$ minutes.

The study in this chapter has three limitations : 1) The analysis of liver tumor motion is complex and diverse, involving challenges related to free-breathing, tissue compressibility, and various types of motion. Currently, using liver centroid motion to represent tumor motion is a challenge, and achieving more precise ROI selection and automatic tumor tracking remain challenging ; 2) This chapter combines motion in the SI, AP, and LR directions into a single Euclidean distance termed "3D total motion". While this approach ensures a comprehensive consideration of motion, allowing the setting of specific gating thresholds based on the amplitude of each patient's 3D total tumor motion, it simplifies treatment planning and reduces the complexity associated with motion. However, during actual radiotherapy, it is essential to consider the motion amplitude separately in each direction rather than just the sum in three directions ; 3) The choice of gating windows significantly impacts the duration and effectiveness of radiotherapy. Further research is needed to develop optimal gating windows for each patient. To achieve effective motion-compensated radiotherapy through gating strategies in Unity, striking a better balance between protection of Organs at Risk (OAR) and dose coverage, Chapter Five will focus on introducing an optimization algorithm for gating thresholds. It will also propose an integrated online solution that combines tumor tracking and motion prediction.

4.5 Conclusion

This study proposed an online gating signal prediction scheme and verified the effectiveness of LR for predicting internal organ or tumor motions derived from 2D cine-MR data. The study introduced a linear interpolation for the prediction of the threshold-crossing time and achieved better temporal accuracies for the subsequent gating signals. The study compared linear models with three latest RNN models (LSTM, Bi-LSTM, and GRU), and evaluated the accuracy of the generated binary gating signal using temporal metrics. Additionally, the study also proposed and evaluated an ALR model, initialized by the data of the first 30 seconds of each patient and updated sequentially during online prediction.

In conclusion, the proposed online gating signal prediction scheme could offset the system delays in beaming on/off switching and thus deliver the dose with better temporal accuracy. The Elekta Unity is potentially capable of performing more accurate radiotherapy procedures if coupled with the proposed gating scheme.

Algorithm 1 Adaptive gating signal prediction

```
Training part (for burn-in) :
Get X,Y ∈ training data
Initialize $\beta_{j-1}, \beta_j$                                  ▷ see in Eq.4.4

Testing part :
Require: tumor traces $[x_1, \ldots, x_N]$
Ensure: gating signal $[T_{\text{on}}, T_{\text{off}}]$

lookforbeamon ← 1
for $i \leftarrow 1$ to $N$ do
    $[\widehat{y}_{j-1}, \widehat{y}_j] \leftarrow \text{pred}(x_i, \beta_{j-1}, \beta_j)$        ▷ see in Eq.4.1
    $dt \leftarrow T_{\text{cross}} - (T_i + j \times \triangle T)$              ▷ $T_{\text{cross}}$ see in Eq.??
    if lookforbeamon=1 then
        if condition 1 == true then
            push ($T_{\text{cross}}$ - latency) into $T_{\text{on}}$                  ▷ $latency = 0.5sec$
            lookforbeamon ← 0
        end if
    else if lookforbeamon=0 then
        if condition 2 == true then
            push ($T_{\text{cross}}$ - latency) into $T_{\text{off}}$
            lookforbeamon ← 1
        end if
    end if
    Update training data
    Update $\beta_{j-1}, \beta_j$                                  ▷ see in Eq.4.3
end for
return $T_{\text{on}}$, $T_{\text{off}}$
```

▷ condition 1 : $(\widehat{y}_j > \text{Th}$ **and** $dt \leq 0.5\Delta T)$ **or** $(\widehat{y}_{j-1} > \text{Th} \geq \widehat{y}_j)$

▷ condition 2 : $(\widehat{y}_j < \text{Th}$ **and** $dt \leq 0.5\Delta T)$ **or** $(\widehat{y}_{j-1} < \text{Th} \leq \widehat{y}_j)$

Chapitre 5

AN EFFICIENT PATIENT-SPECIFIC GATING SCHEME WITH ORTHOGONAL CINE-MRI

5.1 Introduction

Chapter 2 refined the KCF algorithm to enable real-time tracking of tumors, extracting their motion trajectories in three dimensions. Chapter 3 and Chapter 4 meticulously elucidated and proposed effective algorithms for predicting tumor motion and forecasting gating signals, specifically tailored for 2D cine-MRI. Building upon the groundwork laid out earlier, this chapter introduces a comprehensive online solution that seamlessly integrates tumor tracking and motion prediction. Furthermore, it presents an optimization algorithm for 3D gating thresholds, with a keen focus on analyzing how the selection of gating windows impacts both dose coverage and gating accuracy. To conclude, this chapter conducts a thorough dosimetric validation of the proposed gating scheme within the framework of this thesis.

Respiratory gating is one of the most effective methods to reduce radiation dose to normal tissues and maximize the delivery of radiation dose to tumors, especially during patient motion caused by breathing. In the planning of gating schemes, the selection of gating windows is crucial, and the criteria for choosing gating windows should comprehensively consider factors such as tumor motion amplitude, positional error, time intervals, normal tissue protection, and the accuracy and stability of radiation therapy equipment. This chapter primarily explores the balance between window size and duty cycle (the ratio of beam-on time to overall treatment time). While maintaining a certain duty cycle, it is still necessary to determine the optimal respiratory phase to obtain an appropriate gating window. If the gating window is too short, the treatment time may be excessively long, causing discomfort to patients ; conversely, if the gating window is too long, the gating scheme may be ineffective. The optimal gating window depends on the respiratory motion of the patient's tumor and surrounding normal tissues.

Currently, widely used in clinical practice is a phase-based respiratory gating technology called Real Position Management (RPM), which is based on surface signals [104][114]. This technique is applicable to respiratory-gated radiotherapy for lung and liver cancers. In the workflow of the RPM system, window selection is based on the Respiratory Amplitude Distribution (RAD) tool embedded in the Eclipse treatment planning system.

However, to ensure the efficiency of gating plans, gating windows often include several phases. In such cases, because RAD does not directly provide the respiratory motion stability for individual windows, the selection of windows based on the RAD tool inevitably relies on the subjective experience and visual accuracy of decision-making physicians or physicists. Se An Oh and colleagues [122] conducted an analysis of 52 liver cancer patients who underwent real-time position management and respiratory guidance training. Their research indicated that the patients exhibited the lowest respiratory variability during the phases of 30-60% and 30-70%. Therefore, these two respiratory phases can be considered suitable windows for liver cancer radiotherapy gating plans.

Due to the capability of 2D Cine-MRI to directly monitor and locate tumors without relying on surrogates, employing a position-based gating strategy in MRgRT is more precise. Seregni et al. [145] proposed a spherical window, determining the trade-off between window size and duty cycle by analyzing the probability distribution functions of each patient's motion trajectory. The window size was set to 30% of the 3D motion range of the tumor, and the optimal irradiation position was chosen by maximizing the duty cycle. This implies that the gating window is of the same size in all three directions.

However, by analyzing the patients' respiratory motion curves, we found that the tumor's motion in the SI direction is significantly larger than in the AP and LR directions. Therefore, the spherical gating window proposed by Seregni et al. cannot fit the tumor's motion curve well. Consequently, the shape of the gating window is also one of the crucial factors influencing the efficacy of radiotherapy. Different window shapes have certain effects on radiation dose distribution and tumor control effectiveness.

Seregni et al. [145] developed a tumor motion prediction interpolation framework specifically designed for MRI guidance. However, they utilized an offline approach based on the SIFT algorithm to extract tumor motion features from Cine-MRI slices. While their study reported a prediction framework for generating three-dimensional gate signals, they transformed tumor motion in three directions into Euclidean distance and did not individually respond to gate switching based on motion in each direction.

To address the aforementioned challenges, this chapter proposes an integrated online solution that combines tumor tracking and motion prediction. The key contributions are summarized as follows :

1. We consolidate previous work and introduce an end-to-end respiratory motion online solution based on orthogonal Cine-MRI. This solution is designed for real-time monitoring and automatic localization of the three-dimensional spatial position of tumors during Elekta Unity MR-Linac and similar magnetic resonance imaging-guided radiotherapy. It predicts the tumor's motion trajectories in three directions.

2. We simultaneously consider the tumor's motion in three directions and fit an optimal rectangular cuboid based on the motion range of each patient's tumor. The optimal gating window for each patient is obtained by solving for this optimal cuboid.

3. We explore various schemes for deriving three-dimensional gating signals based on the tumor's motion in one, two, or three directions, catering to the treatment needs of different patients.

4. We conduct dosimetric validation of the gating scheme proposed in this thesis.

5.2 Materials and methods

5.2.1 Optimization and Selection of Gating Windows

Considering gating technology, and given that 2D Cine-MRI can directly locate tumors without relying on surrogates, we simulated a position-based gating approach. In this approach, the beam is activated when the tumor is within a fixed range (gating window) around the planned irradiation position. Once the tumor motion exceeds the gating window, the radiation beam is deactivated. The selection of the gating window is crucial, as finding the optimal balance between protecting OARs and achieving the best duty cycle for each patient is challenging and can be viewed as an optimization problem. Next, we will introduce two models for fitting tumor motion and use them as gating windows, evaluating them based on the comparison of duty cycle and gating window volume.

We first employed the spherical window proposed by Seregni et al. [145]. We collected tumor motion data for each patient during the initial 30 seconds (150 frames) of radiotherapy, representing the distribution of tumor centroids as the set . By analyzing the probability distribution function of the dataset G for each patient, they determined the trade-off between window size and duty cycle (the ratio of beam-on time to the overall treatment time) to define the size of the irradiation position and gating window. Specifically, the window size (w) was set to 30% of the 3D motion range of the tumor and the optimal irradiation position was selected by maximizing the duty cycle :

$$\bar{x}^{\text{opt}} = [\bar{LR}, \bar{AP}, \bar{SI}] = \arg\max_{\bar{x}}(\frac{\#\sqrt{\|x-\bar{x}\|} \leq w}{\#x}) \tag{5.1}$$

Where x is the tumor position, $\bar{x}$ is the irradiation position to be optimized, and $\#\{.\}$ denotes the sample quantity. The volume of the spherical gating window is given by :

$$V_{\text{sphere}} = \frac{4}{3}\pi w^3 \tag{5.2}$$

, where w is the radius of the sphere (see Tables 5.1 and 5.2 for details).

By analyzing the respiratory motion curves of patients, we observed that the tumor's motion in the SI direction is significantly greater than in the AP and LR directions. Therefore, the spherical gating window proposed by Seregni et al. does not fit the tumor's motion curve well. Additionally, during treatment planning, the PTV can only be expanded in fixed sizes in three directions based on CTV or GTV, resulting in the gating window having a rectangular shape.

We set gating thresholds in each of the three directions based on the motion amplitudes in the first 30 seconds for each patient, forming a rectangular window.The internal region of this rectangular prism, denoted as E_Ω, is defined as :

$$E_\Omega = \begin{Bmatrix} |x - x_0| < a \\ |y - y_0| < b \\ |z - z_0| < c \end{Bmatrix} \tag{5.3}$$

Our goal is to find the optimal parameters for the rectangular prism, minimizing the volume of the prism ($vol(E_\Omega)$) as it expands outside the PTV, while maximizing the duty cycle (the number of tumor centroids within E_Ω). The duty cycle is defined as the ratio of the time the beam is on during gated radiation therapy to the total treatment time. The precise duty cycle for the rectangular prism window can be obtained from Eq.4.6 and is expressed as :

$$\text{Duty cycle} = \frac{\text{Time of beam on}}{\text{Total time of therapy}} \times 100\% \tag{5.4}$$

By traversing in search of the optimal solution, we have established the rule for setting the gating thresholds as follows : the thresholds in the left-right and anterior-posterior directions are set at 95% of the maximum values, while the threshold in the superior-inferior direction is set to the average of the motion amplitudes. The outward expansion sizes in all three directions are approximated to integers (in mm) to meet the requirements of the planning system. The volume of the rectangular gating window is given by : $V_{\text{cuboid}} = 2a \times 2b \times 2c$, where $2a$, $2b$, and $2c$ are the thresholds in the three directions, respectively (details can be found in Table 5.1 and Table 5.2).

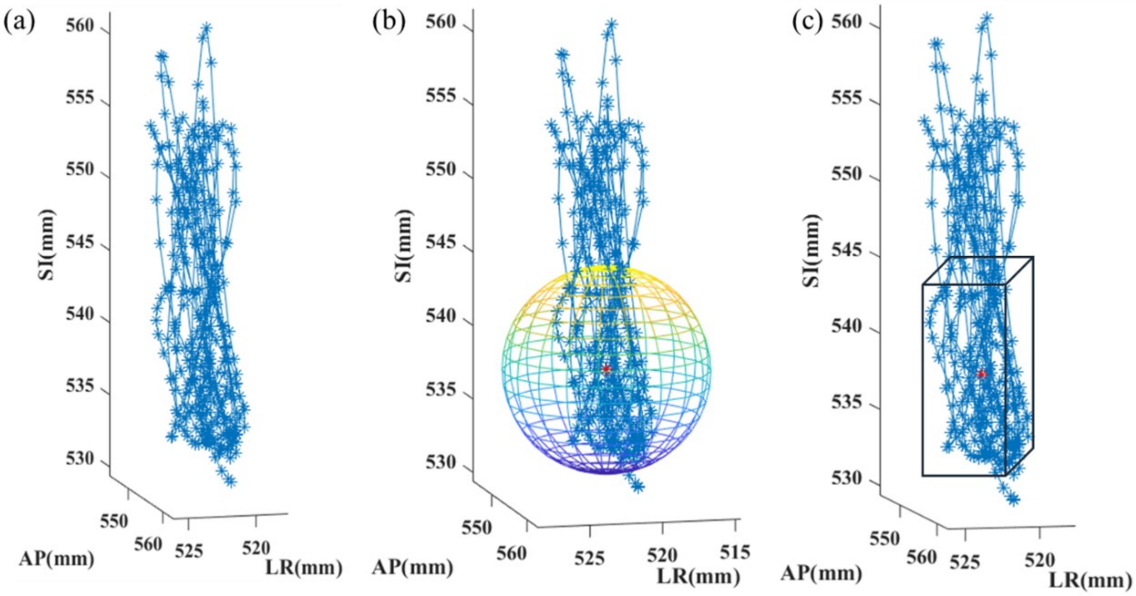

FIGURE 5.1 – Tumor Centroid Motion Trajectory and Gating Window Selection in 3D Space.(a)Motion trajectory of the tumor centroid for a lung cancer patient.(b)Selection of a spherical gating window, indicated by a red asterisk denoting the center of the sphere.(c)Selection of a cuboidal gating window, indicated by a red asterisk denoting the center of the sphere.

Figure 5.1 illustrates the motion trajectory of the tumor centroid in 3D space for a lung cancer patient, along with diagrams showing the selection of both spherical and cuboidal gating windows. It can be observed from Figure 5.1 that the tumor centroid motion in the SI direction is significantly greater than that in the AP and LR directions. Furthermore, compared to the cuboidal optimization window proposed in our study, the volume of the spherical gating window proposed is noticeably larger.

Table 5.1 and Table 5.2 respectively record the comparison of gating window size, gating window volume, and duty cycle for spherical and cuboid gating windows for 10 lung cancer and 10 liver cancer patients. Our proposed cuboidal gating window significantly reduces the volume of the gating window while increasing the duty cycle. The volume

Table 5.1 – comparison of gating window size, gating window volume, and duty cycle for spherical and cuboid gating windows in 10 lung cancer patients

patient	Cuboid					Sphere		
	D(%)	LR(a) (mm)	AP(b) (mm)	SI(c) (mm)	Volue (mm3)	D (%)	Radius (mm)	Volue (mm3)
1	60.1	3	3	7	504	56.2	7	1436.8
2	51.4	3	3	6	432	43.1	5	523.6
3	64.4	3	4	6	576	64.5	6	904.8
4	52.0	3	4	4	384	47.0	5	523.6
5	55.9	3	3	7	504	54.4	7	1436.8
6	90.8	3	3	3	216	84.1	3	113.1
7	49.0	4	3	8	768	52.4	7	1436.8
8	73.8	3	3	8	576	60.4	6	904.8
9	87.1	3	3	8	576	84.1	7	1436.8
10	55.3	3	3	7	504	54.2	7	1436.8
mean	64.0	3.1	3.2	6.4	452.2	60.0	6.0	1117.2

of the spherical gating window is even twice the volume of the cuboidal gating window, leading to a significant increase in the volume of the Planning Target Volume (PTV) in radiotherapy plans. Consequently, this increases the radiation dose to Organs at Risk (OARs), resulting in more severe side effects. Therefore, this study opts for the cuboidal shape as the gating window. Specific gating thresholds for each direction can be found in Table 5.1 and Table 5.2.

5.2.2 Workflow of the proposed online system

The proposed solution for patient-specific 3D gating follows a workflow illustrated in figure 5.2. For each patient, the initial step involves manual outlining of the tumor on the first frame using the Labelme tool [138], resulting in a binary mask of the tumor and a template for subsequent tracking. The KCF algorithm is utilized as the tracker, which returns the region of maximum response. To improve tracking accuracy, a center of mass calculation is performed on the pixels covered by the mask within that region, enabling the precise localization of the tumor centroid. The trajectory of the tumor in the superior-inferior (SI) direction is determined by identifying the highly correlated slice, which can be either the coronal or sagittal slice. The motion trajectories obtained from the first 150 slices (equivalent to 30 seconds) are used to initialize the predictor for online prediction of motion trajectories during subsequent radiotherapy sessions. Concurrently,

TABLE 5.2 – comparison of gating window size, gating window volume, and duty cycle for spherical and cuboid gating windows in 10 liver cancer patients

liver			Cuboid				Sphere	
	D(%)	LR(a) (mm)	AP(b) (mm)	SI(c) (mm)	Volue (mm3)	D (%)	Radius (mm)	Volue (mm3)
1	66.1	3	5	7	840	68.4	6	904.8
2	53.0	3	3	7	504	50.4	6	904.8
3	54.5	4	4	5	640	50.9	5	523.6
4	64.0	3	3	7	504	60.2	7	1436.8
5	48.0	3	3	8	576	50.4	6	904.8
6	50.1	3	3	6	432	49.5	7	1436.8
7	58.1	5	5	8	1600	45.5	8	2144.7
8	84.4	3	3	8	576	79.2	8	2144.7
9	42.4	5	3	8	960	37.0	7	1436.8
10	45.3	5	3	8	960	43.8	7	1436.8
mean	56.6	3.7	3.5	7.5	759	53.5	6.7	1327.5

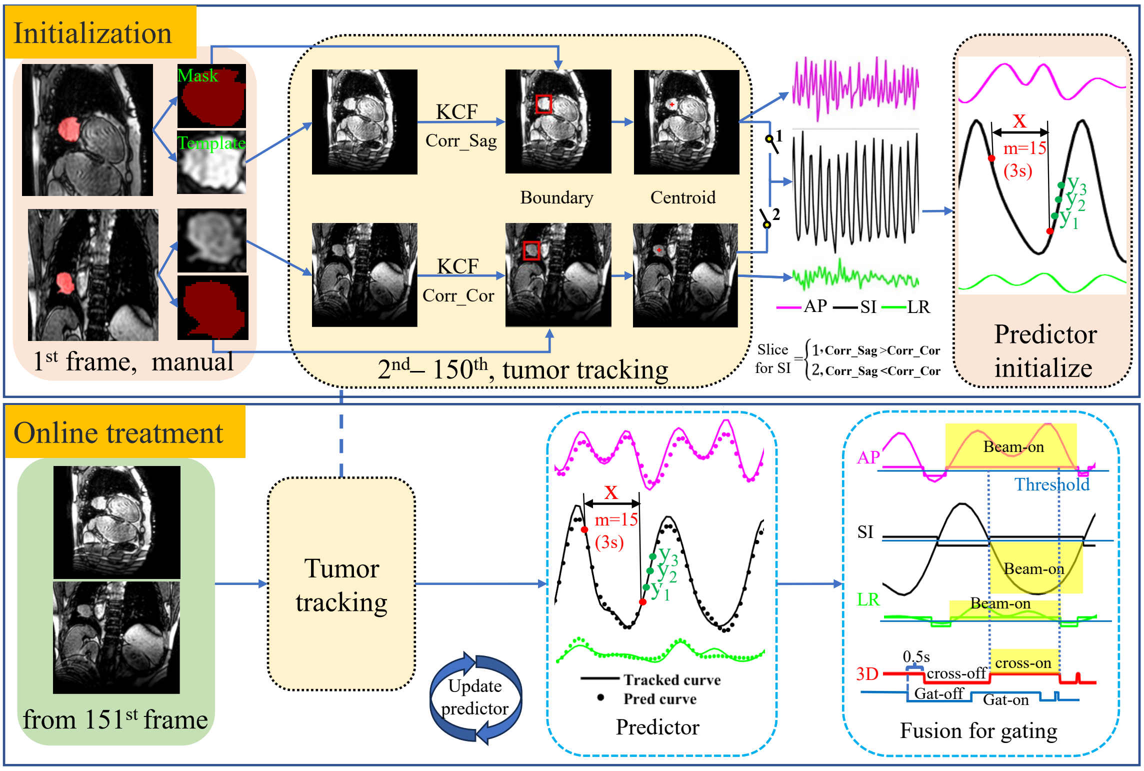

FIGURE 5.2 – Flow chart of the end-to-end online solution for patient-specific 3D gating in MRI-guided radiotherapy.

gating thresholds are specified based on the amplitude of motion in the three directions. As the radiation treatment begins from the 151st frame, the following steps are cyclically executed : 1) The tumor tracking is performed to obtain the current tumor position. 2) The predictor estimates the tumor's position after 0.6 seconds. 3) The tracked tumor position is added to the training set, updating the predictor in real-time. 4) The system evaluates whether the tumor is projected to cross the gating thresholds in three directions. 5) Based on the evaluation, the corresponding gating signal is calculated. 6) A unique gating signal is generated according to the set gating rules to control beam-on or beam-off during the radiotherapy. This workflow enables real-time adaptation to the patient's tumor motion and ensures accurate 3D gating during MRI-guided radiotherapy sessions.

5.2.3 Performance evaluation for gating

The description of gating accuracy is given by Eq.4.7, and it is applied separately in the SI, AP, and LR directions.

The ideal gating thresholds are set based on the amplitude of tumor motion in three directions, i.e., the cuboid gating window. By comparing the gating signals obtained from the proposed system with the true tumor motion trajectory, the corresponding true tumor motion amplitude when triggering the gating switch can be calculated. This is defined as the predicted threshold of the system, denoted as :

$$\text{Th\_pred} = \frac{\sum_{i=1}^{N}(T_{\text{off},i} - T_{\text{on},i}) \cdot \left(\frac{y_{\text{on},i} - y_{\text{off},i}}{2}\right)}{\sum_{i=1}^{N}(T_{\text{off},i} - T_{\text{on},i})} \tag{5.5}$$

where $T_{\text{on},i}$ and $T_{\text{off},i}$ are the times of triggering on/off during the i^{th} respiratory cycle, and $y_{\text{on},i}$ and $y_{\text{off},i}$ are the amplitudes at triggering on/off during the i^{th} respiratory cycle.

Gating threshold error is a measure of uncertainty in the gating process and is defined as the difference between the ideal threshold and the predicted threshold. This predicted threshold can be used as an expansion criterion for the PTV in radiotherapy planning. The proposed system is designed to obtain dose-volume histograms (DVH) for PTV and OAR in the radiotherapy plan and is compared with the original plan without the gating system to verify the improvement of the proposed system in clinical dosages.

5.2.4 Dose Verification

To visually validate the clinical significance of the proposed gating system, in addition to evaluating the accuracy of the gating signals (as detailed in Section 4.3.3), we simulated the dose delivery treatment results using this gating system based on these predictions. A dose comparison was made with treatments without the gating scheme. We simulated the scenario of dose delivery under free-breathing conditions using a 7 MV linear accelerator with Agility MLC configuration (Elekta AB, Stockholm, Sweden) and no flattening filter. The gating threshold was set to the cuboid gating window proposed in this chapter. The beam was open when the centroid of the tumor was within the threshold window, and treatment stopped once the centroid of the tumor moved beyond the threshold window.

We also calculated the volume of the PTV used for radiotherapy based on the above gating scheme and compared it with the PTV without the gating scheme. PTV_{8mm} was defined by expanding the GTV from the planning CT in various directions by 8 mm, a common practice for setting PTV in lung cancer patients without further motion information [170]. PTV_{indiv} was individually defined as a personalized PTV, also expanded from the planning CT's GTV, with expansion sizes in each direction determined by the predicted threshold (cuboid gating window), represented by the red dots in Figure 5.3 for 10 lung cancer and 10 liver cancer patients.

Taking the first lung cancer patient as an example, due to the constraints of the monacle planning system, the expansion edges could only be in integer millimeters. PTVindiv was approximately expanded by 7 mm, 5 mm, and 3 mm in the SI, AP, and LR directions, respectively. Table 5.4 shows the volumes of GTV, PTV_{8mm}, and PTV_{indiv} for 10 lung cancer and 10 liver cancer patients, as well as the percentage reduction in volume of PTV_{indiv} compared to PTV_{8mm}. On average across 10 lung cancer and 10 liver cancer patients, PTV_{indiv} reduced by 33.6% and 25%, respectively.

One of the main contributions of this chapter is the quantitative assessment of our proposed tracking and prediction-based gating system in terms of dose delivery. Two static (Step and Shoot) IMRT plans were created for each patient based on PTV8mm and PTVindiv on the planning CT. The dose volume histograms (DVH) of the two sets of plans were compared. IMRT plans were generated using the TPS (Monaco, v5.40.01, Elekta AB, Stockholm, Sweden) with a 1.5 T transverse magnetic field. Beam angles were manually selected, and the same angles were used for the same patient. The prescription dose for lung cancer was set at 54 Gy in 30 fractions, and for liver cancer, it was set at 50 Gy in 25 fractions. The system utilized a GPU-based fast Monte Carlo (GPU-MC)

TABLE 5.3 – Volumes of GTV, PTV8mm, and PTVindiv for 10 lung cancer and 10 liver cancer patients, along with the percentage reduction in volume of PTVindiv compared to PTV8mm.

	Lung				Liver			
Patients	GTV	PTV8mm	PTVindiv	Reduce(%)	GTV	PTV8mm	PTVindiv	Reduce(%)
1	3.2	23.1	12.5	45.9	24.8	80.9	52.8	34.7
2	42.4	119.5	78.6	34.2	80.6	220.6	168.7	23.5
3	69.2	189.5	147.9	22.0	20.5	78.6	59.4	24.4
4	20.6	93.0	54.2	41.7	140.4	286.3	251.3	12.2
5	26.0	84.9	56.2	33.8	33.9	101.5	78.8	22.4
6	29.5	105.4	66.4	37.0	78.4	211.8	199.1	6.0
7	22.0	84.6	65.8	22.2	4.7	28.6	16.0	44.1
8	64.9	166.0	121.9	26.6	8.3	38.4	23.7	38.3
9	2.7	21.3	12.4	41.8	12.5	32.8	25.8	21.3
10	7.2	38.8	26.7	31.2	32.1	98.2	75.2	23.4
Mean	28.8	92.6	64.3	33.6	43.6	117.8	95.1	25.0

dose calculation platform, with uniform magnetic field input for strength and direction. For effective plan comparison, all plans were normalized to the average dose of PTV (95% isodose line set to the prescription dose). Plan results were compared based on target coverage and OAR protection. Target coverage metrics included : (1) Homogeneity Index (HI) calculated for PTV, where

$$HI = \frac{D2\% - D98\%}{Dp \times 100\%} \tag{5.6}$$

with Dp being the prescription dose. Lower HI values indicate more uniform dose coverage [165] ; (2) Conformity Index (CI) :

$$CI = \frac{(V^2_{(PTV,ref)})}{V_{PTV}\dot{V}_{ref}} \tag{5.7}$$

where $V_{(PTV,ref)}$ is the volume covered by the prescription dose, V_{PTV} is the PTV volume, and V_{ref} is the volume of the prescription isodose. Higher CI values indicate better dose coverage and consistency. Normal tissue protection for lung cancer was based on the average doses received by OARs : whole lung (V5, V10, Dmean), left lung (V10, V20, Dmean), right lung (V5, V10, Dmean), heart (V30, V40, Dmean), and spinal cord (Dmax). Normal tissue protection for liver cancer was based on the average doses received by OARs : normal liver (V30, V40, Dmean), right kidney (V5, V10, V15, Dmean), and

Table 5.4 – Acceptable dose limits for PTV and OARs

Liver cancer		Lung cancer	
Structures	Acceptable criteria	Structures	Acceptable criteria
PTV	V95% >95%	PTV	V95% >95%
	D98% >47.50 Gy		D98% >51.30 Gy
	D2% <55.02 Gy		D2% <59.40 Gy
	HI		HI
	CI		CI
Normal liver	Dmean <23 Gy	Whole lung	Dmean <17 Gy
	V30Gy <28%		V5Gy <70%
	V40Gy <24%		V10Gy <55%
Spinal cord	Dmax <40 Gy		V20Gy<30%
Right kidney	Dmean <18 Gy	Heart	Dmean <20 Gy
	V5Gy <70%		V40Gy <70%
	V10Gy <55%		V30Gy <55%
	V15Gy <35%	Spinal cord	Dmax <40 Gy

spinal cord (Dmax). Table 5.4 shows the acceptable dose limits for PTV and OARs.

5.3 Results and Discussion

5.3.1 Gating accuracy

According to the analysis of the tumor motion trajectory, the average movement amplitude and signal-to-noise ratio of the tumor in the SI direction are significantly higher than those in the AP and LR directions. Therefore, the tumor exhibits dominant motion in the SI direction, leading to better tracking and predictive performance. We have designed two decision mechanisms for gating signals : 1). The first mechanism focuses solely on the motion in the SI direction, using the maximum values of motion in the AP and LR directions as their respective thresholds. In this case, the 3D gating signal is equal to the gating signal in the SI direction. 2). The second mechanism considers the comprehensive motion of the tumor in all three directions. If the motion in any direction exceeds its threshold, the beam is closed. In this case, the ideal 3D beam gating signal is the intersection of the beam gating signals in all three directions.

Table 5.5 presents the gating accuracy of tracking with and without (w/o) prediction for 10 lung cancer and 10 liver cancer patients. When considering motion in all three directions simultaneously and using KCF and ALR together, the average gating accuracy reached 93.6% for lung patients and 91.3% for liver patients, respectively. However, when considering motion only in the SI direction, the average gating accuracy improved to 97.4% for lung patients and 97.2% for liver patients.

When using only automatic tracking without prediction, the gating accuracy reported in Table 5.5 varied between 77% and 85%. However, when applying linear regression prediction, the gating accuracy increased to above 91%. This result demonstrates the significant role of motion prediction in compensating for system latency and improving the overall gating accuracy. Additionally, we assessed the impact of optimizing tumor selection in the SI direction on gating accuracy. The results indicate that when utilizing SI direction localization with optimized selection proposed in Chapter 1, gating accuracy is superior to relying solely on the coronal or sagittal planes to determine SI direction motion.

TABLE 5.5 – Gating accuracy of tracking w/o prediction for 10 lung cancer patients and 10 liver cancer patients.

Gating methods		Ground truth Dutycycle(%)	Accuracy without prediction		Accuracy with prediction	
			TM(%)	KCF(%)	TM(%)	KCF(%)
lung	SI(Cor)[1]	71.8±13.9	83.1±5.4	83.1±5.7	97.4±1.0	97.1±0.9
	SI(Sag)[1]	70.9±14.5	81.2±6.8	81.5±6.8	96.5±1.9	96.8±1.7
	SI(optimal)[1]	72.9±14.7	83.5±5.6	83.6±6.1	97.4±0.9	97.4±0.7
	SI[2]	66.6±15.3	79.1±7.1	79.2±8.0	91.5±8.4	91.8±8.2
	SI+AP[2]		78.8±7.6	79.4±6.7	93.3±4.2	93.6±4.1
	SI+AP+LR[2]		78.8±7.6	79.2±7	93.4±3.8	93.5±4.4
liver	SI(Cor)[1]	69.8±17.8	84.7±6.4	84.0±6.4	96.7±1.7	96.1±2.4
	SI(Sag)[1]	69.9±9.8	84.4±5.3	84.2±5.1	95.0±3.6	95.7±2.9
	SI(optimal)[1]	69.1±13.5	84.9±6.3	85.1±6.1	96.6±2.8	97.2±1.5
	SI[2]	56.1±12.4	76.9±6.6	77.7±6.8	84.8±8.5	85.5±8.0
	SI+AP[2]		78.1±5.8	77.6±7.3	86.0±8.0	85.5±9.2
	SI+AP+LR[2]		80.0±5.1	80.3±5.6	91.0±4.8	91.3±4.7

[1] Ground truth of gating signal is obtained from SI direction only

[2] Ground truth of 3D gating signal is obtained from the SI, AP and LR directions.

Figure 5.3 illustrates the ideal thresholds in three directions for specific patients, along with the corresponding predicted thresholds obtained using KCF and TM trackers. As the predicted thresholds approach the ideal thresholds, the gating threshold error becomes smaller. It can be observed that the predicted thresholds achieved with the KCF tracker outperform those obtained with the TM tracker.

Furthermore, for lung cancer cases, the average gating threshold errors based on KCF are 0.54 mm, 0.21 mm, and 0.38 mm in the SI, LR, and AP directions, respectively.

Similarly, for liver cancer, the averages are 0.65 mm, 0.5 mm, and 0.89 mm in the SI, LR, and AP directions, respectively. These results indicate that the KCF tracker provides more accurate predictions of the gating thresholds compared to the TM tracker.

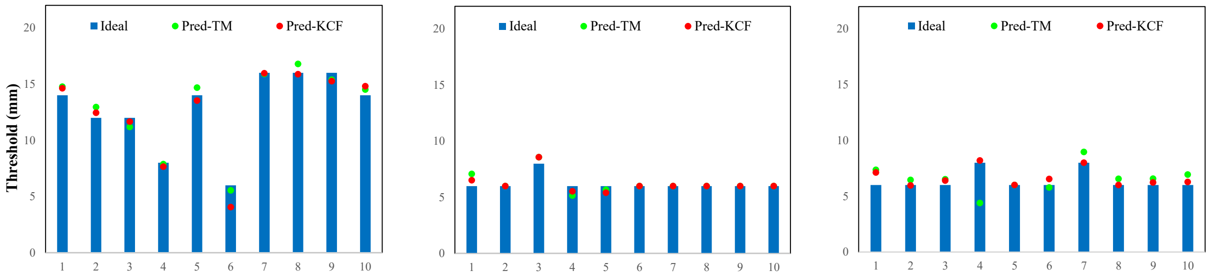

(a) Lung patients - SI (b) Lung patients-LR (c) Lung patients-AP

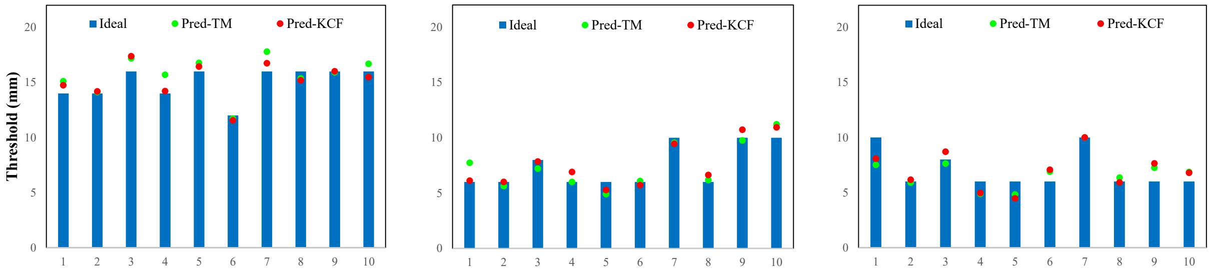

(d) Liver patients-SI (e) Liver patients-LR (f) Liver patients-AP

FIGURE 5.3 – Ideal and predicted thresholds in the case of radiotherapy guided by gated signals generated by the proposed system.

5.3.2 Complexity and computational time

All experiments were conducted using MATLAB (The MathWorks Inc, Natick, MA) on a machine equipped with an Intel 4-core 2.4-GHz CPU, NVIDIA GeForce GTX 1660 Ti GPU, 512 GB SSD, and 20 GB RAM. The computation cost was measured by the execution time required for tumor tracking, motion prediction, and generation of the 3D gating signal. Specifically, this experiment focused solely on comparing tumor localization among the three trackers, while other processes in the system remained unchanged. Therefore, any differences in computation cost were observed exclusively in the three trackers. As mentioned earlier, the primary goal of the trackers was to track the entire target region (lung tumor or liver organ) on cine-MRI.

Henriques et al. [58] reported that the KCF tracker achieves O(n log n) complexity by leveraging the fast Fourier transform, which reduces computing time compared to more computationally expensive matrix algebra. The speed of the KCF tracker is directly influenced by the size of the tracked region ($M \times N$).

Table 2.2 presents the time required to track either boundary or centroid (lung tumor and liver organ) using TM, KCF, and MOSSE algorithms. For tracking lung tumor boundaries, TM takes 3.4 ± 1.07 ms, KCF takes 2.6 ± 0.97 ms, and MOSSE takes 1.1 ± 0.32 ms. For liver boundaries, TM takes 13.9 ± 5.67 ms, KCF takes 4.3 ± 1.25 ms, and MOSSE takes 1.8 ± 0.63 ms. To improve tracking accuracy, the centroid of the target region was calculated, resulting in an additional approximate 3 ms of computation time for centroid calculation. Section 3.4.3 reports that the average computation time for motion prediction using ALR is 1 ms, while the remaining process for generating the 3D gating signal takes less than 1 ms.

Table 5.6 presents the system latency (ms) of the Unity for the gating scheme and the delay (ms) of the proposed system. The online system combining KCF and ALR achieves computation times within 10 ms. For our study, we set a fixed delay of 0.5 s to account for the end-to-end system delay in the specific case of MRI-guided gating applications, although this delay might not necessarily represent the state-of-the-art in MRI-guided precision radiotherapy under ideal circumstances. As the MRI image sampling frequency increases, the overall system latency decreases, which subsequently leads to higher accuracy in predicting gating signals using the proposed system.

TABLE 5.6 – The system latency (ms) of the Unity for gating scheme and the delay (ms) of the proposed system.

	MRI acquisition	Tumor tracking	Centroid position	Motion prediction	Gating signal	Trigger ON/OFF	Total	Prediction window
Lung	250±100	2.6±0.9	2.6±0.9	1	1	10	<500	600
Liver	250±100	4.3±1.3	2.9±1.4	1	1	10	<500	600

5.3.3 Dose validation result

To validate the clinical improvements of the proposed system in gated radiotherapy for liver and lung cancer, we calculated the actual gating window thresholds generated by the proposed system. Based on these real gating window expansions, we generated new Planning Target Volumes (PTV_new) and redesigned radiotherapy plans (Plan2) for

TABLE 5.7 – Dosimetric comparison of 10 lung cancer patients (mean and std).

structure	Plan1	Plan2	Improve [%]	p-value
PTV D98% [cGy]	5366.6±54.5	5402.4±24.0	-	NS
PTV D2% [cGy]	5802.4±15.5	5818.9±66.2	-	NS
PTV CI	0.92±0.02	0.96±0.02	4.3	NS
PTV HI (%)	7.8±1.1	7.4±1.5	5.1	NS
Lung_All V5 [%]	19.4±5.9	17.1±5.8	12	<0.05
Lung_All V10 [%]	13.5±3.6	13.5±4	11.2	<0.05
Lung_All Dmean [cGy]	579.9±174.9	536.9±166.5	7.4	<0.05
LungL V10 [%]	28.5±6.5	26.8±6.6	5.7	<0.05
LungL V20 [%]	19±6.7	18.3±6.1	3.4	NS
LungL Dmean [cGy]	967.6±266.7	919.6±253.2	5	<0.05
LungR V5 [%]	4.9±3.7	3.8±3	22.2	<0.01
LungR V10 [%]	0.1±0.2	0.1±0.1	25.9	<0.01
LungR Dmean [cGy]	162.2±44.8	145.9±48.6	10.1	<0.05
Heart V30 [%]	7.4±6.6	6.2±5.8	15.6	<0.05
Heart V40 [%]	1.2±1.4	1±1	22.6	<0.01
Heart Dmean [cGy]	696.1±431.3	630.5±411.7	9.4	<0.05
Spinal cord Dmax [cGy]	1544.3±539.6	1550.4±667.1	-0.4	NS

PTV_new. The resulting DVHs from Plan2 were then compared to the original radiotherapy plans (Plan1). Tables 5.7 and 5.8 present DVH comparisons for 10 cases each of lung cancer and liver cancer patients.

On average, among the 10 lung cancer patients, there was little difference in target coverage and spinal cord protection between the two plans. However, Plan2 exhibited significant improvement over Plan1 in protecting the healthy lung and heart. For instance, Plan2 showed a 22.2% increase in V5 and V20 for the right lung, and a 25.9% increase in V40 for the heart.

For the 10 liver cancer patients, on average, Plan2 improved target coverage and spinal cord protection (although not statistically significant). Notably, Plan2 demonstrated clear superiority over Plan1 in protecting the normal liver and right kidney. For example, Plan2 increased V30 and V40 for the normal liver by 15.3% and 20%, respectively. Additionally, Plan2 increased V10, V15, and V20 for the right kidney by 21.3%, 26.9%, and 26.2%, respectively.

TABLE 5.8 – Dosimetric comparison of 10 liver cancer patients (mean and std).

structure	Plan1	Plan2	Improve [%]	p-value
PTV D98% [cGy]	5005.4±50	5020.8±30	-	NS
PTV D2% [cGy]	5480.3±30	5474.1±21	-	NS
PTV CI	1.12±0.04	1.08±0.02	3.5	NS
PTV HI (%)	9.5±1.3	9.1±0.9	4.2	NS
Normal liver V30 [%]	10.4±6.5	8.8±5.8	15.3	<0.05
Normal liver V40 [%]	2.5±1.6	2.0±1.4	20.0	<0.05
Normal liver Dmean [cGy]	1114±145	1080±140	3.1	<0.05
Right kidney V5 [%]	22.5±20.4	21.2±18.6	5.3	<0.01
Right kidney V10 [%]	16.9±13.7	13.3±10	21.3	<0.05
Right kidnay V15 [%]	10.4±6.7	7.6±5.2	26.9	<0.05
Right kidney V20 [%]	6.1±4.2	4.5±4.0	26.2	NS
Right kidney Dmean [cGy]	454.2±44.8	382.9±48.6	15.6	<0.01
Spinal cord Dmax [cGy]	1964.3±839.6	1901.4±761.1	3.2	NS
Heart V30 [%]	7.4±6.6	6.2±5.8	15.6	<0.05
Heart V40 [%]	1.2±1.4	1±1	22.6	<0.01
Heart Dmean [cGy]	696.1±431.3	630.5±411.7	9.4	<0.05
Spinal cord Dmax [cGy]	1544.3±539.6	1550.4±667.1	-0.4	NS

5.3.4 Discussion

The Elekta Unity system allows real-time acquisition of orthogonal coronal and sagittal MR cine, enabling the reconstruction of the tumor trajectory during radiotherapy by measuring its three spatial components. This study has successfully verified the performance of the proposed end-to-end online solution for patient-specific 3D gating signal in MRI-guided radiotherapy. To the best of our knowledge, this is the first evaluation of the time cost and accuracy of an end-to-end online MR cine-based 3D gating signal prediction system. Furthermore, it is worth noting that the proposed solution is universally applicable to all image acquisition modalities, such as X-ray, CBCT, and ultrasound, for precision radiotherapy. Previous studies [148][67][196][55] have demonstrated the effectiveness of various image acquisition modalities in precision radiotherapy.

Efficiency in tumor localization and motion prediction is crucial for the success of gating systems, especially in situations where inevitable system delays exist. In radiation therapy, accurate and rapid tracking and prediction of tumor movement are vital to ensure the effectiveness of treatment and minimize the potential impact of uncertainties. The proposed online solution provides a fast and accurate method for patient-specific 3D gating systems in MRgRT, contributing to improved treatment outcomes and reduced side effects on surrounding normal tissues.

This chapter discusses the selection and optimization of gating windows. Seregni et al. [145] proposed a spherical window, determining the window size and duty cycle balance by analyzing the probability density function (PDF) of each patient's motion trajectory. The window size (w) was set to 30% of the 3D motion range of the tumor, and the optimal irradiation position was chosen by maximizing the duty cycle. This means that the gating window is of equal size in all three directions. However, by analyzing the patient's respiratory motion curve, it was found that the tumor's movement in the SI direction is significantly greater than in the AP and LR directions.

Therefore, the spherical gating window proposed by Seregni et al. does not fit well with the tumor's motion curve. Additionally, in radiotherapy planning, the PTV can only expand a fixed size in three directions based on the CTV or GTV. This constraint makes the gating window have to be in the shape of a cuboid. The rectangular cuboid gating window we proposed greatly reduces the volume of the gating window while increasing the duty cycle. The volume of the spherical gating window is even approximately twice that of the rectangular cuboid gating window, which will lead to a significant increase in the volume of the PTV in the radiotherapy plan, thereby exposing the OAR to more additional radiation doses and causing more severe side effects.

Theoretically, in the proposed framework, the predicted 3D gating signal should be more accurate if the groundtruth gating signal considers the motion of the tumor in all three directions simultaneously, i.e. if a threshold smaller than its motion amplitude is set in each of the three directions. However, as shown in Table3, for the average results of 10 lung cancers, the predicted 3D gating signal is more accurate when determined by gating signals in both SI and AP directions, rather than considering all three directions of SI, AP, and LR together. Analyzing the motion trajectories of the tumors in the SI, AP and LR directions for the 10 lung cancer cases, their average motion amplitudes were 12.8mm, 4.2mm and 2.8mm, respectively, and their average signal-to-noise ratios were 4.3dB, 0.5dB and -1.4dB. Thus, the tumors showed dominant motion in the SI direction, resulting in better tracking and prediction performance, while the LR direction exhibited the least motion and worst signal-to-noise ratio, potentially introducing greater prediction errors. Considering only SI motion or both SI and AP motion, rather than all three directions simultaneously, is more reasonable in terms of prediction accuracy and cycle time efficiency.

Geometric uncertainty and computational cost in the prediction of automatic tumor tracking and gating signals were quantified by simulating beam gating. Three correlation-based tracking algorithms were tested : TM, MOSSE, and KCF. Based on these algorithms, we calculated the tumor center of mass to improve tracking accuracy. KCF performed best in terms of both time cost and tracking accuracy for both liver and lung cancer patients. For gated radiotherapy, it is critical that the beam on/off control is accurately predicted when the target crosses the threshold position. Therefore, we propose a time-scale gating accuracy to compare it with the ideal gating signal. The gating accuracy results show that the binary gating signal of the proposed framework achieves more than 90% temporal accuracy.

Furthermore, the corresponding true tumor motion amplitude, i.e. the predicted threshold at the gating trigger, can be calculated from the timing of the beam switch triggered by the gating signal predicted by the proposed system. By comparing the ideal threshold with the predicted threshold, the gating threshold error measures the geometric uncertainty of beam triggering during gating. In subsequent work, this predicted threshold can be used as an extrapolation criterion for the PTV in the radiotherapy plan. Thus, the DVH of the PTV and OAR in the proposed framework can be calculated and compared with the original plan without this gating system, in order to obtain validation of the dosimetric improvement.

5.4 Conclusion

In summary, the developed online system, combining KCF and ALR, offers a cost-effective and efficient solution for accurate tumor motion tracking and prediction in motion-compensated radiotherapy. The system's performance demonstrates significant improvements in tracking accuracy and gating efficiency. Leveraging cine-MRI guidance, it provides real-time tumor motion prediction and gating decisions, enhancing the precision and efficacy of motion compensated treatments. The patient-specific approach allows adaptation to individual characteristics, particularly crucial for lung and liver cancers with varying inter-patient tumor motion. Additionally, the high gating accuracy achieved in both lung and liver cancer patients highlights the system's versatility and potential application in diverse tumor types. Finally, dose verification demonstrates that the proposed online gating system significantly improves the protection of surrounding critical organs. Overall, the system's robustness and reliability make it a valuable tool in motion-compensated radiotherapy for thoracic and abdominal cancer patients. Accurate beam gating is essential to ensure precise delivery of radiation, and our proposed framework's high temporal accuracy provides confidence in its reliability for real-time radiotherapy.

CONCLUSION AND PERSPECTIVES

Conclusion

Elekta Unity offers real-time high spatial resolution soft tissue imaging and holds the potential to compensate for respiratory motion through gating schemes. To enhance the precision of thoracoabdominal tumor radiotherapy, dynamic adjustment of dose delivery based on real-time observation of respiratory motion is required. However, from a technical standpoint, achieving safe and reliable real-time adaptive MR-guided radiotherapy (MRgRT) through Continuous Motion Management (CMM) still faces some challenging hurdles. The accuracy and efficiency of real-time tracking algorithms and tumor motion prediction algorithms in three-dimensional space determine the accuracy of implementing gating schemes in Elekta Unity.

This paper developed an end-to-end gating system for real-time motion compensation during lung cancer and liver cancer treatment on the Elekta Unity. This system can monitor and automatically locate the 3D spatial position of the tumor in real-time, and can predict the tumor's motion trajectory in three directions in advance. Based on the set gating rules, a unique gating signal can be generated to control the beam on and off during radiotherapy, thereby compensating for the inaccuracy of dose delivery due to respiratory motion.

The contributions of this thesis are as follows :

(1) Proposed a workflow for tumor tracking based on KCF

In this study, we first constructed a database of real patient MR motion monitoring in Unity, and evaluated three major tumor tracking algorithms in detail using 2D Cine-MRI data from 20 patients. We specifically highlighted the excellent performance of the KCF algorithm in real-time tracking. To address issues such as irregular tumor shapes and deformations caused by breathing, we introduced centroid calculation methods to improve the accuracy of the KCF algorithm in determining tumor positions. For positioning problems in the SI direction, we proposed a personalized slice selection scheme by calculating the correlation in different slice directions, effectively overcoming challenges posed by tumor shape changes in different planes. Overall, our proposed workflow for tumor tracking based on KCF is efficient and accurate on 2D Cine-MRI, providing a significant first step towards patient-specific gating schemes for thoracoabdominal tumor MR-guided radiotherapy in this thesis.

(2) Proposed a transfer C-NLSTM framework for tumor motion prediction

This study introduces a novel C-NLSTM model and validates its effectiveness in real-time prediction of respiratory motion using publicly available databases. Additionally, to address the challenge of insufficient patient 2D Cine-MRI data, transfer learning is introduced. It leverages pre-trained models and knowledge from existing datasets to effectively address related tasks with small datasets. In summary, this study presents a patient-specific transfer C-NLSTM model, evaluates the predictive performance of C-NLSTM on two large public databases, and then tests the transfer C-NLSTM on the Unity database for real-time prediction of tumor motion in MRgRT.

(3) Proposed a gating signal prediction algorithm based on 2D Cine-MRI

This study validated the effectiveness of linear regression for predicting the movement of internal organ or tumor in 2D Cine-MRI, and proposed an online gating signal prediction scheme to enhance the accuracy of MRgRT for liver and lung cancer. Furthermore, to address the issue of expensive training data, we proposed a patient-specific ALR model, where online data training for each patient lasted only 30 seconds as a burn-in period, and model parameters were updated during online prediction.Finally, we also validated that a prediction window of 0.6 seconds is more suitable than a 0.4-second window under the condition of a 0.5-second system delay.

(4) Proposed an efficient patient-specific gating scheme with orthogonal cine-MRI

This study combined previous work and presented an end-to-end online respiratory motion solution based on 2D Cine-MRI, specifically designed for MRgRT. It involved real-time monitoring and automatic localization of tumor spatial positions in three dimensions, as well as prediction of tumor motion trajectories in three directions. Additionally, it fitted an optimal cuboid to the motion range of each patient's tumor, obtaining the optimal gating window for each patient by solving for the optimal cuboid. Various schemes for generating three-dimensional gating signals based on tumor motion in one, two, or three directions were explored to adapt to the treatment needs of different patients. Finally, dosimetric validation of the proposed gating scheme demonstrated significant improvements in protecting surrounding critical organs.

The above three works introduced tumor tracking workflow, tumor motion prediction algorithm, and gating signal prediction algorithm, individually. Ultimately, we proposed an online gating system that integrates KCF and ALR, providing high accuracy and efficiency for motion compensation in liver and lung cancer radiotherapy. This system demonstrates outstanding performance in tracking precision and gating efficiency. Due to significant inter-patient variations in tumor motion, the patient-specific gating system allows for dynamic adjustment of gating thresholds based on individual characteristics. Furthermore, the high gating accuracy achieved in lung and liver cancer patients highlights its versatility and potential application across different thoracoabdominal tumor types. In summary, the robustness and reliability of this system make it an invaluable tool for motion-compensated radiotherapy in thoracoabdominal cancer patients.

Prospects for future work

While this research has made progress in achieving real-time localization and motion prediction of lung tumors and liver organs during the Elekta Unity radiotherapy, providing reasonably accurate three-dimensional gating signals for guiding gated radiation therapy, it still faces numerous technical challenges and hurdles in the workflow for managing respiratory motion in thoracoabdominal tumors, necessitating further research and exploration.

During the process of tumor tracking, while the centroid-based calculation method can effectively improve the accuracy of tumor localization, especially showing significant advantages in dealing with deformations caused by respiratory motion, we also recognize that centroid motion may not fully reflect subtle changes in the tumor's edge contour. This limitation may restrict the precision of radiotherapy in some cases. Therefore, the future work will mainly focus on how to more accurately track and describe the tumor's edge contour. Firstly, we will optimize the existing image segmentation techniques to improve the accuracy and stability of tumor edge contour extraction through improved algorithms and parameter settings. Secondly, we plan to explore new methods that combine centroid motion and edge contour information to more comprehensively reflect the tumor's motion state, providing a more reliable basis for radiotherapy.

For patients with liver cancer who have not received contrast agents, the identification of tumor boundaries is extremely difficult, making the quantification of liver tumor motion a challenging task. In this study, to overcome the inability to visualize liver tumors without the use of contrast agents, we used the motion of the liver centroid as a proxy for the motion of the tumor centroid. However, this remains an approximate method that cannot fully and accurately reflect the motion trajectory of the entire liver tumor in three-dimensional space. Therefore, the outlook for liver tumor tracking work primarily focuses on finding more suitable methods and structures to more precisely reflect the motion trajectory of the entire liver tumor in three-dimensional space. Additionally, we will investigate how to integrate individual patient differences and respiratory patterns to further optimize the accuracy and stability of tumor motion tracking.

This study validates the effectiveness of ALR in predicting tumor motion. It demonstrates higher prediction accuracy and efficiency on 2D Cine-MRI data compared to the RNN model, and only requires 30 seconds of training data, overcoming the difficulty of collecting individualized patient data on the Unity. Due to the limited number of Unity databases in this study and the need to optimize the model in real-time to cope with irregular patient respiratory motion, ALR is more suitable for the gating system proposed in this study. With the gradual enrichment of the Unity database and continuous advancements in software and hardware technology, we plan to train more robust RNN models. RNN models have unique advantages in processing sequential data, capable of capturing the time dependency and long-term dependency of tumor motion. Additionally, we have demonstrated that the patient-specific transfer C-NLSTM method can effectively improve the prediction performance of the RNN model. In future work, we will continue to deepen research in this field, explore the potential of more patient-specific transfer learning methods, and strive to better apply them to RNN models.

Compared to the gating technique applied in this study, the development of MLC tracking technology holds greater potential. This is particularly crucial for patients with significant tumor motion as it allows for free breathing during treatment without an extended beam-on time (100% duty cycle). While MLC tracking and VMAT are not currently available in the current clinical MR-linac version, the feasibility of implementing VMAT + MLC tracking on Elekta Unity has been demonstrated by Prescilla Uijtewaal and others [168]. However, further work is required to develop an integrated clinical workflow. The clinical treatment planning system needs to fully support VMAT on Elekta Unity, especially for daily plan adjustments. Additionally, imaging and motion estimation workflows should be tailored to individual patients.

Clinical real-time adaptive MRgRT requires thorough quality assurance and testing. Specialized end-to-end tests have been proposed to assess certain aspects of adaptive MR-guided RT [86][159][112][35] thus far. Future developments in end-to-end testing may focus on evaluating real-time imaging, dose calculations, and accumulation methods. Furthermore, mechanisms ensuring robust and safe radiation delivery need to be implemented within real-time MR-guided workflows.

Moreover, magnetic resonance-integrated proton therapy (MRiPT) is expected to become an important development direction for clinical applications in the next 5-10 years. Proton therapy, with its unique physical characteristics, can achieve high-precision irradiation of tumor tissues, thus imposing stricter requirements on the precision of proton beams [95][193]. Against this backdrop, the patient-specific gating system proposed by us is expected to play a greater role in the future. By combining the high-resolution imaging of MRI and the precise control of gating technology, we can achieve accurate positioning and delivery of proton beams, thereby further enhancing the effectiveness and safety of radiotherapy. Therefore, future research efforts will be focused on further improving and optimizing the patient-specific gating system to meet the needs of high-precision radiotherapy, such as proton therapy.

LIST OF PUBLICATIONS

International Journals

1. Yang Li, Zuyi Yu, Yang Chen, Chunfeng Yang, Yue Li, X. Allen Li and Baosheng Li. Automatic seizure detection using fully convolutional nested LSTM [J]. International journal of neural systems, 2020, 30(04) : 2050019. (Q1, IF=8.0)

2. Yang Li, Zhenjiang Li, Jian Zhu, Baosheng Li, Huazhong Shu, and Di Ge. Online prediction for respiratory movement compensation : a patient-specific gating control for MRI-guided radiotherapy [J]. Radiation Oncology, 2023, 18(1) : 149. (Q2, IF=3.6)

3. Yang Li, Zhenjiang Li, Jian Zhu, Baosheng Li and Di Ge. Tumor motion prediction using transfer C-NLSTM in MRI-guided Radiotherapy [J]. Engineering Applications of Artificial Intelligence. (Under review)

International Conferences

1. Yang Li, Zhenjiang Li, Jian Zhu, Baosheng Li and Di Ge. Gating scheme with respiration motion prediction in MRI-guided Radiotherapy : a proof-of-concept study for lung cancer [C]. 6th Edition of International Cancer Conference, August 17-19, 2023 in London, UK. (Oral presentation)

2. Yang Li, Zhenjiang Li, Jian Zhu, Baosheng Li and Di Ge. An Efficient Patient-Specific Gating Scheme with Orthogonal Cine-MRI [C]. 66th Annual Meeting of the American Association of Physicists in Medicine. (Submitted)2024

BIBLIOGRAPHIE

[1] Bourque E ALEXANDRA et al., « A particle filter motion prediction algorithm based on an autoregressive model for real-time MRI-guided radiotherapy of lung cancer », in : *Biomedical Physics and Engineering Express* 3 (2017), URL : `https://api.semanticscholar.org/CorpusID:126205921`.

[2] Yusuke ANETAI et al., « A concept for classification of optimal breathing pattern for use in radiotherapy tracking, based on respiratory tumor kinematics and minimum jerk analysis », in : *Medical Physics* 43.*6Part1* (2016), p. 3168-3177.

[3] Hoffmann ASWIN et al., « MR-guided proton therapy : a review and a preview », in : *Journal of Applied Clinical Medical Physics* 15.*1* (2020), p. 1-13.

[4] Narendra C BABU et Eswara B REDDY, « A moving-average filter based hybrid ARIMA–ANN model for forecasting time series data », in : *Applied Soft Computing* 23 (2014), p. 27-38.

[5] Kathy L BAGLAN et al., « Accelerated partial breast irradiation using 3D conformal radiation therapy (3D-CRT) », in : *International Journal of Radiation Oncology and Biology and Physics* 55.*2* (2003), p. 302-311.

[6] Sarah BAKER et al., « A critical review of recent developments in radiotherapy for non-small cell lung cancer », in : *Radiation Oncology* 11 (2016), p. 1-14.

[7] Salem BELHAJ et Moncef TAGINA, « Modeling and Prediction of the Internet End-to-end Delay using Recurrent Neural Networks », in : *Networks* 4.*6* (2009), p. 528-535.

[8] Anders S BERTELSEN et al., « First clinical experiences with a high field 1.5 T MR linac », in : *Acta Oncologica* 58.*10* (2019), p. 1352-1357.

[9] Jenny BERTHOLET et al., « Real-time intrafraction motion monitoring in external beam radiotherapy », in : *Physics in Medicine and Biology* 64.*15* (2019), 15TR01.

[10] Henric BLOMGREN et al., « Stereotactic high dose fraction radiation therapy of extracranial tumors using an accelerator : clinical experience of the first thirty-one patients », in : *Acta Oncologica* 34.*6* (1995), p. 861-870.

[11] David S Bolme et al., « Visual object tracking using adaptive correlation filters », in : *2010 IEEE Computer Society Conference on Computer Vision and Pattern Recognition*, IEEE, 2010, p. 2544-2550.

[12] PTS Borman, BW Raaymakers et M Glitzner, « ReconSocket : a low-latency raw data streaming interface for real-time MRI-guided radiotherapy », in : *Physics in Medicine and Biology* 64.*18* (2019), p. 185008.

[13] Thomas Bortfeld, « IMRT : a review and preview », in : *Physics in Medicine and Biology* 51.*13* (2006), R363.

[14] Stephen Boyd et al., « Distributed optimization and statistical learning via the alternating direction method of multipliers », in : *Foundations and Trends® in Machine Learning* 3.*1* (2011), p. 1-122.

[15] Lau Brix et al., « Three-dimensional liver motion tracking using real-time two-dimensional MRI », in : *Medical Physics* 41.*4* (2014), p. 042302.

[16] Martin J Brown, David J Carlson et David J Brenner, « The tumor radiobiology of SRS and SBRT : are more than the 5 Rs involved ? », in : *International Journal of Radiation Oncology and Biology and Physics* 88.*2* (2014), p. 254-262.

[17] Waqas Bukhari et SM Hong, « Real-time prediction and gating of respiratory motion using an extended Kalman filter and Gaussian process regression », in : *Physics in Medicine and Biology* 60.*1* (2014), p. 233.

[18] Florian Büther, Mirco Hess et Klaus P Schäfers, « Investigating the influence of baseline drifts of respiratory signals in amplitude-based gating for positron emission tomography », in : *2014 IEEE Nuclear Science Symposium and Medical Imaging Conference (NSS/MIC)*, IEEE, 2014, p. 1-4.

[19] Wei Cao et al., « Changing profiles of cancer burden worldwide and in China : a secondary analysis of the global cancer statistics 2020 », in : *Chinese Medical Journal* 134.*07* (2021), p. 783-791.

[20] Laura I Cervino, Jiang Du et Steve B Jiang, « MRI-guided tumor tracking in lung cancer radiotherapy », in : *Physics in Medicine and Biology* 56.*13* (2011), url : `https://doi.org/10.1088/0031-9155/56/13/003`.

[21] Joe Y Chang et al., « Stereotactic ablative radiotherapy versus lobectomy for operable stage I non-small-cell lung cancer : a pooled analysis of two randomised trials », in : *The Lancet Oncology* 16.*6* (2015), p. 630-637.

[22] AM Chen et al., « MRI-guided radiotherapy for head and neck cancer : initial clinical experience », in : *Clinical and Translational Oncology* 20 (2018), p. 160-168.

[23] George TY Chen, Jong H Kung et Kevin P Beaudette, « Artifacts in computed tomography scanning of moving objects », in : *Seminars in Radiation Oncology*, t. 14, 1, Elsevier, 2004, p. 19-26.

[24] Qinsheng Chen et al., « Fluoroscopic study of tumor motion due to breathing : facilitating precise radiation therapy for lung cancer patients », in : *Medical Physics* 28.*9* (2001), p. 1850-1856.

[25] SeungWook Choi et al., « Performance enhancement of respiratory tumor motion prediction using adaptive support vector regression : Comparison with adaptive neural network method », in : *International Journal of Imaging Systems and Technology* 24.*1* (2014), p. 8-15, doi : `10.1002/IMA.22073`.

[26] Stephen G Chun et al., « Impact of intensity-modulated radiation therapy technique for locally advanced non–small-cell lung cancer : a secondary analysis of the NRG oncology RTOG 0617 randomized clinical trial », in : *Journal of Clinical Oncology* 35.*1* (2017), p. 56.

[27] Sjoerd Crijns et Bas Raaymakers, « From static to dynamic 1.5 T MRI-linac prototype : impact of gantry position related magnetic field variation on image fidelity », in : *Physics in Medicine and Biology* 59.*13* (2014), p. 3241.

[28] Ying Cui et al., « Robust fluoroscopic respiratory gating for lung cancer radiotherapy without implanted fiducial markers », in : *Physics in Medicine and Biology* 52.*3* (2007), p. 741.

[29] Justine M Cunningham et al., « Development and evaluation of a novel MR-compatible pelvic end-to-end phantom », in : *Journal of Applied Clinical Medical Physics* 20.*1* (2019), p. 265-275.

[30] Jennifer De Los Santos et al., « Image guided radiation therapy (IGRT) technologies for radiation therapy localization and delivery », in : *International Journal of Radiation Oncology and Biology and Physics* 87.*1* (2013), p. 33-45.

[31] Deon Dick et al., « A fiducial-less tracking method for radiation therapy of liver tumors by diaphragm disparity analysis part 2 : validation study by using clinical data », in : *Journal of Radiation Oncology* 7 (2018), p. 345-356.

[32] Jun Duan et al., « Dosimetric effect of respiration-gated beam on IMRT delivery », in : *Medical Physics* 30.*8* (2003), p. 2241-2252.

[33] Neal E Dunlap et al., « Size matters : a comparison of T1 and T2 peripheral non-small-cell lung cancers treated with stereotactic body radiation therapy (SBRT) », in : *The Journal of Thoracic and Cardiovascular Surgery* 140.*3* (2010), p. 583-589.

[34] Robert E Elliott et al., « Efficacy of gamma knife radiosurgery for small-volume recurrent malignant gliomas after initial radical resection », in : *World Neurosurgery* 76.*1-2* (2011), p. 128-140.

[35] Alina Elter et al., « End-to-end test of an online adaptive treatment procedure in MR-guided radiotherapy using a phantom with anthropomorphic structures », in : *Physics in Medicine and Biology* 64.*22* (2019), p. 225003.

[36] Ernst et Floris, *Compensating for Quasi-periodic Motion in Robotic Radiosurgery*, Springer New York, 2012.

[37] Floris Ernst, Alexander Schlaefer et Achim Schweikard, « Prediction of respiratory motion with wavelet-based multiscale autoregression », in : Springer, 2007, p. 668-675.

[38] Floris Ernst et Achim Schweikard, « Forecasting respiratory motion with accurate online support vector regression (SVRpred) », in : *International Journal of Computer Assisted Radiology and Surgery* 4 (2009), p. 439-447.

[39] P Esquinazi et al., « Induced magnetic ordering by proton irradiation in graphite », in : *Physical Review Letters* 91.*22* (2003), p. 227201.

[40] Mary Feng et al., « Characterization of pancreatic tumor motion using cine MRI : surrogates for tumor position should be used with caution », in : *International Journal of Radiation Oncology and Biology and Physics* 74.*3* (2009), p. 884-891.

[41] S Ferdinand et al., « Dosimetric analysis of Deep Inspiratory Breath-hold technique (DIBH) in left-sided breast cancer radiotherapy and evaluation of pre-treatment predictors of cardiac doses for guiding patient selection for DIBH », in : *Technical Innovations and Patient Support in Radiation Oncology* 17 (2021), p. 25-31.

[42] EC Ford et al., « Evaluation of respiratory movement during gated radiotherapy using film and electronic portal imaging », in : *International Journal of Radiation Oncology and Biology and Physics* 52.*2* (2002), p. 522-531.

[43] SD Fossa et al., « Optimal planning target volume for stage I testicular seminoma : a Medical Research Council randomized trial », in : *Journal of Clinical Oncology* 17.*4* (1999), p. 1146-1146.

[44] Dorota Gabryś et al., « Dosimetric comparison of liver tumour radiotherapy in all respiratory phases and in one phase using 4DCT », in : *Radiotherapy and Oncology* 100.*3* (2011), p. 360-364.

[45] Bernd Gagel et al., « Active breathing control (ABC) : determination and reduction of breathing-induced organ motion in the chest », in : *International Journal of Radiation Oncology and Biology and Physics* 67.*3* (2007), p. 742-749.

[46] John S Ginn et al., « Characterization of spatial distortion in a 0.35 T MRI-guided radiotherapy system », in : *Physics in Medicine and Biology* 62.*11* (2017), p. 4525.

[47] P Giraud et al., « Reduction of organ motion effects in IMRT and conformal 3D radiation delivery by using gating and tracking techniques », in : *Cancer/Radiothérapie* 10.*5* (2006), p. 269-282.

[48] Philippe Giraud et Annie Houle, « Respiratory gating for radiotherapy : main technical aspects and clinical benefits », in : *ISRN Pulmonology* 2013 (2013), p. 1-13.

[49] Markus Glitzner et al., « MLC-tracking performance on the Elekta unity MRI-linac », in : *Physics in Medicine and Biology* 64.*15* (2019), 15NT02.

[50] Gene H Golub, Michael Heath et Grace Wahba, « Generalized cross-validation as a method for choosing a good ridge parameter », in : *Technometrics* 21.*2* (1979), p. 215-223.

[51] Olga L Green et al., « First clinical implementation of real-time, real anatomy tracking and radiation beam control », in : *Medical Physics* 45.*8* (2018), p. 3728-3740.

[52] Matthias Guckenberger et al., « Is a single respiratory correlated 4D-CT study sufficient for evaluation of breathing motion ? », in : *International Journal of Radiation Oncology and Biology and Physics* 67.*5* (2007), p. 1352-1359.

[53] Joseph Hanley et al., « Deep inspiration breath-hold technique for lung tumors : the potential value of target immobilization and reduced lung density in dose escalation », in : *International Journal of Radiation Oncology and Biology and Physics* 45.*3* (1999), p. 603-611.

[54] Koji Hara et al., « Radiotherapy for hepatocellular carcinoma results in comparable survival to radiofrequency ablation : a propensity score analysis », in : *Hepatology* 69.*6* (2019), p. 2533-2545.

[55] Emma Harris, Davide Fontanarosa et Clive Baldock, « In the future, ultrasound guidance in radiotherapy will become a clinical standard », in : *Physical and Engineering Sciences in Medicine* (2021), p. 1-4.

[56] Justin Hartke, Matthew Johnson et Marwan Ghabril, « The diagnosis and treatment of hepatocellular carcinoma », in : *Seminars in Diagnostic Pathology*, t. 34, 2, Elsevier, 2017, p. 153-159.

[57] Trevor Hastie et al., *The elements of statistical learning : data mining, inference, and prediction*, t. 2, Springer, 2009.

[58] João F Henriques et al., « High-speed tracking with kernelized correlation filters », in : *IEEE Transactions on Pattern Analysis and Machine Intelligence* 37.*3* (2014), p. 583-596.

[59] Nicholas J Higham, *Accuracy and stability of numerical algorithms*, SIAM, 2002.

[60] Sepp Hochreiter et Jürgen Schmidhuber, « Long short-term memory », in : *Neural Computation* 9.*8* (1997), p. 1735-1780.

[61] Arthur E Hoerl et Robert W Kennard, « Ridge regression : Biased estimation for nonorthogonal problems », in : *Technometrics* 12.*1* (1970), p. 55-67.

[62] Jeremy DP Hoisak et al., « Correlation of lung tumor motion with external surrogate indicators of respiration », in : *International Journal of Radiation Oncology and Biology and Physics* 60.*4* (2004), p. 1298-1306.

[63] Mischa Hoogeman et al., « Clinical accuracy of the respiratory tumor tracking system of the cyberknife : assessment by analysis of log files », in : *International Journal of Radiation Oncology and Biology and Physics* 74.*1* (2009), p. 297-303.

[64] K. Huang et al., « A Comparative Study of a Novel AE-nLMS Filter and Two Traditional Filters in Predicting Respiration Induced Motion of the Tumor », in : *IEEE International Conference on Bioinformatics and Bioengineering*, 2010, p. 281-282.

[65] Dan Ionascu et al., « Internal-external correlation investigations of respiratory induced motion of lung tumors », in : *Medical Physics* 34.*10* (2007), p. 3893-3903.

[66] Nikhil IYENGAR et al., « Age-related alterations in the fractal scaling of cardiac interbeat interval dynamics », in : *American Journal of Physiology-Regulatory, Integrative and Comparative Physiology* 271.*4* (1996), R1078-R1084.

[67] Xiance JIN et al., « CBCT-based volumetric and dosimetric variation evaluation of volumetric modulated arc radiotherapy in the treatment of nasopharyngeal cancer patients », in : *Radiation Oncology* 8.*1* (2013), p. 279-279.

[68] Alexander JÖHL et al., « Performance comparison of prediction filters for respiratory motion tracking in radiotherapy », in : *Medical Physics* 47.*2* (2020), p. 643-650.

[69] Scott L JOHNSON et al., « 91 Initial clinical experience with an interactive, video-based patient-positioning system for head and neck treatment », in : *International Journal of Radiation Oncology and Biology and Physics* 36.*1* (1996), p. 204.

[70] Alan M KALET et al., « The dosimetric benefit of in-advance respiratory training for deep inspiration breath holding is realized during daily treatment in left breast radiotherapy : A comparative retrospective study of serial surface motion tracking », in : *Journal of Medical Imaging and Radiation Oncology* 65.*3* (2021), p. 354-364.

[71] Fazle KARIM et al., « LSTM fully convolutional networks for time series classification », in : *IEEE Access* 6 (2017), p. 1662-1669.

[72] Paul KEALL, « 4-dimensional computed tomography imaging and treatment planning », in : *Seminars in Radiation Oncology*, t. 14, 1, Elsevier, 2004, p. 81-90.

[73] Paul J KEALL et al., « The management of respiratory motion in radiation oncology report of AAPM Task Group 76 a », in : *Medical Physics* 33.*10* (2006), p. 3874-3900.

[74] Timothy D KEIPER et al., « Feasibility of real-time motion tracking using cine MRI during MR-guided radiation therapy for abdominal targets », in : *Medical Physics* 47.*8* (2020), p. 3554-3566.

[75] Mehdi KHASHEI et Mehdi BIJARI, « A novel hybridization of artificial neural networks and ARIMA models for time series forecasting », in : *Applied Soft Computing* 11.*2* (2011), p. 2664-2675.

[76] A Kim et al., « Effects of Preparatory Coaching and Home Practice for Deep Inspiration Breath Hold on Cardiac Dose for Left Breast Radiation Therapy », in : *Clinical Oncology* 30.*9* (2018), p. 571-577.

[77] David JW Kim et al., « Held-breath self-gating technique for radiotherapy of non–small-cell lung cancer : A feasibility study », in : *International Journal of Radiation Oncology and Biology and Physics* 49.*1* (2001), p. 43-49.

[78] Diederik P Kingma et Jimmy Ba, « Adam : A method for stochastic optimization », in : *arXiv preprint arXiv :1412.6980* (2014).

[79] Hans M Klein, *clinical low field strength magnetic resonance imaging : a practical guide to accessible MRI*, Springer, 2015.

[80] Sebastian Klüter, « Technical design and concept of a 0.35 T MR-Linac », in : *Clinical and Translational Radiation Oncology* 18 (2019), p. 98-101.

[81] Sebastian Klüter et al., « First prospective clinical evaluation of feasibility and patient acceptance of magnetic resonance-guided radiotherapy in Germany », in : *Strahlentherapie and Onkologie* 196 (2020), p. 691-698.

[82] Eugene J Koay et al., « The role of imaging in the clinical practice of radiation oncology for pancreatic cancer », in : *Abdominal Radiology* 43.*2* (2018), p. 393-403.

[83] Andreas Krauss, Simeon Nill et U Oelfke, « The comparative performance of four respiratory motion predictors for real-time tumour tracking », in : *Physics in Medicine and Biology* 56.*16* (2011), p. 5303.

[84] Patrick Kupelian et al., « Multi-institutional clinical experience with the Calypso System in localization and continuous, real-time monitoring of the prostate gland during external radiotherapy », in : *International Journal of Radiation Oncology and Biology and Physics* 67.*4* (2007), p. 1088-1098.

[85] James M Lamb et al., « Dosimetric validation of a magnetic resonance image gated radiotherapy system using a motion phantom and radiochromic film », in : *Journal of Applied Clinical Medical Physics* 18.*3* (2017), p. 163-169.

[86] James M Lamb et al., « Dosimetric validation of a magnetic resonance image gated radiotherapy system using a motion phantom and radiochromic film », in : *Journal of Applied Clinical Medical Physics* 18.*3* (2017), p. 163-169.

[87] Suk J Lee, Yuichi Motai et Martin Murphy, « Respiratory motion estimation with hybrid implementation of extended Kalman filter », in : *IEEE Transactions on Industrial Electronics* 59.*11* (2011), p. 4421-4432.

[88] Allen X Li, Paul J Keall et Orton G Colin, « Respiratory gating for radiation therapy is not ready for prime time », in : *Medical Physics* 34.*3* (2008), p. 26.

[89] Ruijiang Li et al., « Intrafraction verification of gated RapidArc by using beam-level kilovoltage X-ray images », in : *International Journal of Radiation Oncology and Biology and Physics* 83.*5* (2012), e709-e715.

[90] Yang Li et al., « Automatic seizure detection using fully convolutional nested LSTM », in : *International Journal of Neural Systems* 30.*04* (2020), p. 2050019.

[91] Yang Li et al., « Online prediction for respiratory movement compensation : a patient-specific gating control for MRI-guided radiotherapy », in : *Radiation Oncology* 18.*1* (2023), p. 149.

[92] Hui Lin et al., « Towards real-time respiratory motion prediction based on long short-term memory neural networks », in : *Physics in Medicine and Biology* 64.*8* (2019), p. 085010.

[93] Dale W Litzenberg et al., « Influence of intrafraction motion on margins for prostate radiotherapy », in : *International Journal of Radiation Oncology and Biology and Physics* 65.*2* (2006), p. 548-553.

[94] Ce Liu, Jenny Yuen et Antonio Torralba, « Sift flow : Dense correspondence across scenes and its applications », in : *IEEE Transactions on Pattern Analysis and Machine Intelligence* 33.*5* (2010), p. 978-994.

[95] H. Helen Liu et al., « Assessing respiration-induced tumor motion and internal target volume using four-dimensional computed tomography for radiotherapy of lung cancer. », in : *International Journal of Radiation Oncology and Biology and Physics* 68.*2* (2007), p. 531-540.

[96] Xiaoming Liu et William C Cho, « Precision medicine in immune checkpoint blockade therapy for non-small cell lung cancer », in : *Clinical and Translational Medicine* 6 (2017), p. 1-4.

[97] Josep M Llovet et al., « Sorafenib in advanced hepatocellular carcinoma », in : *New England Journal of Medicine* 359.*4* (2008), p. 378-390.

[98] Frank LOHR et al., « Noninvasive patient fixation for extracranial stereotactic radiotherapy », in : *International Journal of Radiation Oncology and Biology and Physics* 45.*2* (1999), p. 521-527.

[99] Elia LOMBARDO et al., « Offline and online LSTM networks for respiratory motion prediction in MR-guided radiotherapy », in : *Physics in Medicine and Biology* 67.*9* (2022), p. 095006.

[100] David G LOWE, « Distinctive image features from scale-invariant keypoints », in : *International Journal of Computer Vision* 60 (2004), p. 91-110.

[101] Xiaolei MA et al., « Long short-term memory neural network for traffic speed prediction using remote microwave sensor data », in : *Transportation Research Part C : Emerging Technologies* 54 (2015), p. 187-197.

[102] Rockwell T MACKIE et al., « Tomotherapy », in : *Seminars in Radiation Oncology*, t. 9, 1, Elsevier, 1999, p. 108-117.

[103] Majid MAFI et Saeed Montazeri MOGHADAM, « Real-time prediction of tumor motion using a dynamic neural network », in : *Medical and Biological Engineering and Computing* 58 (2020), p. 529-539.

[104] Gikas S MAGERAS et al., « Fluoroscopic evaluation of diaphragmatic motion reduction with a respiratory gated radiotherapy system », in : *Journal of Applied Clinical Medical Physics* 2.*4* (2001), p. 191-200.

[105] Jorge A MARRERO et al., « Observational registry of sorafenib use in clinical practice across Child-Pugh subgroups : the GIDEON study », in : *Journal of Hepatology* 65.*6* (2016), p. 1140-1147.

[106] Thomas R MAZUR et al., « SIFT-based dense pixel tracking on 0.35 T cine-MR images acquired during image-guided radiation therapy with application to gating optimization », in : *Medical Physics* 43.*1* (2016), p. 279-293.

[107] Catherine A. MCBAIN et al., « X-ray volumetric imaging in image-guided radiotherapy : The new standard in on-treatment imaging », in : *International Journal of Radiation Oncology and Biology and Physics* (2006).

[108] Jiangyuan MEI et al., « Learning a Mahalanobis Distance-Based Dynamic Time Warping Measure for Multivariate Time Series Classification », in : *IEEE Transactions on Systems Man and Cybernetics* 46.*6* (2016), p. 1363-1374, DOI : `10.1109/TCYB.2015.2426723`.

[109] P METCALFE et al., « The potential for an enhanced role for MRI in radiation-therapy treatment planning », in : *Technology in Cancer Research and Treatment* 12.*5* (2013), p. 429-446.

[110] Tomas MIKOLOV et al., « Recurrent neural network based language model », in : *Interspeech*, t. 2, 3, Makuhari, 2010, p. 1045-1048.

[111] Kathryn MITTAUER et al., « A new era of image guidance with magnetic resonance-guided radiation therapy for abdominal and thoracic malignancies », in : *Cureus* 10.*4* (2018).

[112] David MÖNNICH et al., « Quality assurance of IMRT treatment plans for a 1.5 T MR-linac using a 2D ionization chamber array and a static solid phantom », in : *Physics in Medicine and Biology* 65.*16* (2020), 16NT01.

[113] Shinichiro MORI et al., « Effective doses in four-dimensional computed tomography for lung radiotherapy planning », in : *Medical Dosimetry* 34.*1* (2009), p. 87-90.

[114] Rebecca MUIRHEAD et al., « The potential clinical benefit of respiratory gated radiotherapy (RGRT) in non-small cell lung cancer (NSCLC) », in : *Radiotherapy and Oncology* (2010), p. 172-177.

[115] M J MURPHY, M ISAAKSON et J JALDÉN, *Adaptive filtering to predict lung tumor motion during free breathing*, CARS 2002 Computer Assisted Radiology et Surgery, 2002.

[116] Martin J MURPHY et Sonja DIETERICH, « Comparative performance of linear and nonlinear neural networks to predict irregular breathing », in : *Physics in Medicine and Biology* 51.*22* (2006), p. 5903.

[117] Martin J MURPHY et Damodar POKHREL, « Optimization of an adaptive neural network to predict breathing », in : *Medical Physics* 36.*1* (2009), p. 40-47.

[118] Martin J MURPHY et al., « The effect of transponder motion on the accuracy of the Calypso electromagnetic localization system », in : *International Journal of Radiation Oncology and Biology and Physics* 72.*1* (2008), p. 295-299.

[119] Victor MURRAY et al., « Movienet : Deep space–time-coil reconstruction network without k-space data consistency for fast motion-resolved 4D MRI », in : *Magnetic Resonance in Medicine* (2023).

[120] Nico JD NAGELKERKE et al., « A note on a general definition of the coefficient of determination », in : *Biometrika* 78.*3* (1991), p. 691-692.

[121] Yoshiharu NEGORO et al., « The effectiveness of an immobilization device in conformal radiotherapy for lung tumor : reduction of respiratory tumor movement and evaluation of the daily setup accuracy », in : *International Journal of Radiation Oncology and Biology and Physics* 50.*4* (2001), p. 889-898.

[122] Se An OH et al., « Optimal Gating Window for Respiratory-Gated Radiotherapy with Real-Time Position Management and Respiration Guiding System for Liver Cancer Treatment », in : *Scientific Reports* 9.*1* (2019), p. 4384.

[123] Kiyoshi OHARA et al., « Irradiation synchronized with respiration gate », in : *International Journal of Radiation Oncology and Biology and Physics* 17.*4* (1989), p. 853-857.

[124] Laura PADILLA, Havne AMANDA, Laura CERVIO et al., « A survey of surface imaging use in radiation oncology in the United States », in : *Journal of Applied Clinical Medical Physics* 20.*12* (2019).

[125] Chiara PAGANELLI et al., « Scale invariant feature transform in adaptive radiation therapy : a tool for deformable image registration assessment and re-planning indication », in : *Physics in Medicine and Biology* 58.*2* (2012), p. 287.

[126] Chiara PAGANELLI et al., « Magnetic resonance imaging–guided versus surrogate-based motion tracking in liver radiation therapy : a prospective comparative study », in : *International Journal of Radiation Oncology and Biology and Physics* 91.*4* (2015), p. 840-848.

[127] Chiara PAGANELLI et al., « MRI-guidance for motion management in external beam radiotherapy : current status and future challenges », in : *Physics in Medicine and Biology* 63.*22* (2018), 22TR03.

[128] Chloe PANDELI et al., « Dose reduction to organs at risk with deep-inspiration breath-hold during right breast radiotherapy : a treatment planning study », in : *Radiation Oncology* 14 (2019), p. 223.

[129] E PAPPAS et al., « Dosimetric performance of the Elekta Unity MR-linac system : 2D and 3D dosimetry in anthropomorphic inhomogeneous geometry », in : *Physics in Medicine and Biology* 64.*22* (2019), p. 225009.

[130] Eric S PAULSON et al., « Consensus opinion on MRI simulation for external beam radiation treatment planning », in : *Radiotherapy and Oncology* 121.*2* (2016), p. 187-192.

[131] Bas W Raaymakers et al., « Integrating a 1.5 T MRI scanner with a 6 MV accelerator : proof of concept », in : *Physics in Medicine and Biology* 54.*12* (2009), N229.

[132] CR Ramsey, D Scaperoth et D Arwood, « Clinical experience with a commercial respiratory gating system », in : *International Journal of Radiation Oncology and Biology and Physics* 3.*48* (2000), p. 164-165.

[133] Charlotte Remy et al., « Potential of a probabilistic framework for target prediction from surrogate respiratory motion during lung radiotherapy », in : *Physics in Medicine and Biology* 66.*10* (2021), p. 105002.

[134] Nadeem Riaz et al., « Predicting respiratory tumor motion with multi-dimensional adaptive filters and support vector regression », in : *Physics in Medicine and Biology* 54.*19* (2009), p. 5735.

[135] Eike Rietzel, Tinsu Pan et George TY Chen, « Four-dimensional computed tomography : image formation and clinical protocol », in : *Medical Physics* 32.*4* (2005), p. 874-889.

[136] Teboh Roland et al., « Incorporating system latency associated with real-time target tracking radiotherapy in the dose prediction step », in : *Physics in Medicine and Biology* 55.*9* (2010), p. 2651.

[137] Dan Ruan, « Kernel density estimation-based real-time prediction for respiratory motion », in : *Physics in Medicine and Biology* 55.*5* (2010), p. 1311.

[138] Bryan C Russell et al., « LabelMe : a database and web-based tool for image annotation », in : *International Journal of Computer Vision* 77 (2008), p. 157-173.

[139] Sohail Sayeh et al., « Respiratory motion tracking for robotic radiosurgery », in : *Treating Tumors that Move with Respiration*, Springer, 2007, p. 15-29.

[140] Maria A Schmidt et Geoffrey S Payne, « Radiotherapy planning using MRI », in : *Physics in Medicine and Biology* 60.*22* (2015), R323.

[141] S SchNecker et al., « Treatment planning and evaluation of gated radiotherapy in left-sided breast cancer patients using the CatalystTM/SentinelTM system for deep inspiration breath-hold (DIBH) », in : *Radiation Oncology* 11.*143* (2016), p. 1-10.

[142] Achim Schweikard et al., « Robotic motion compensation for respiratory movement during radiosurgery », in : *Computer Aided Surgery* 5.*4* (2000), p. 263-277.

[143] Yvette Seppenwoolde et al., « Precise and real-time measurement of 3D tumor motion in lung due to breathing and heartbeat, measured during radiotherapy », in : *International Journal of Radiation Oncology and Biology and Physics* 53.*4* (2002), p. 822-834.

[144] Yvette Seppenwoolde et al., « Accuracy of tumor motion compensation algorithm from a robotic respiratory tracking system : a simulation study », in : *Medical Physics* 34.*7* (2007), p. 2774-2784.

[145] Matteo Seregni et al., « Motion prediction in MRI-guided radiotherapy based on interleaved orthogonal cine-MRI », in : *Physics in Medicine and Biology* 61.*2* (2016), p. 872.

[146] Matteo Seregni et al., « A hybrid image registration and matching framework for real-time motion tracking in MRI-guided radiotherapy », in : *IEEE Transactions on Biomedical Engineering* 65.*1* (2017), p. 131-139.

[147] Hua C Shao et al., « Automatic liver tumor localization using deep learning-based liver boundary motion estimation and biomechanical modeling (DL-Bio) », in : *Medical Physics* 48.*12* (2021), p. 7790-7805.

[148] Gregory C Sharp et al., « Prediction of respiratory tumour motion for real-time image-guided radiotherapy », in : *Physics in Medicine and Biology* 49.*3* (2004), p. 425.

[149] Xiutao Shi et al., « Evaluation of template matching for tumor motion management with cine-MR images in lung cancer patients », in : *Medical Physics* 41.*5* (2014), p. 052304.

[150] Hiroki Shirato et al., « Four-dimensional treatment planning and fluoroscopic real-time tumor tracking radiotherapy for moving tumor », in : *International Journal of Radiation Oncology and Biology and Physics* 48.*2* (2000), p. 435-442.

[151] Hiroki Shirato et al., « Physical aspects of a real-time tumor-tracking system for gated radiotherapy », in : *International Journal of Radiation Oncology and Biology and Physics* 48.*4* (2000), p. 1187-1195.

[152] Hiroki Shirato et al., « Feasibility of insertion/implantation of 2.0-mm-diameter gold internal fiducial markers for precise setup and real-time tumor tracking in radiotherapy », in : *International Journal of Radiation Oncology and Biology and Physics* 56.*1* (2003), p. 240-247.

[153] Hiroki Shirato et al., « Intrafractional tumor motion : lung and liver », in : *Seminars in Radiation Oncology*, t. 14, 1, Elsevier, 2004, p. 10-18.

[154] Hiroki Shirato et al., « Speed and amplitude of lung tumor motion precisely detected in four-dimensional setup and in real-time tumor-tracking radiotherapy », in : *International Journal of Radiation Oncology and Biology Colin, Orton G Physics* 64.*4* (2006), p. 1229-1236.

[155] L Simon et al., « Comparative study and clinical implementation of two breathing-adapted radiotherapy techniques : dosimetric benefits for lung cancer treatment », in : *Cancer Radiotherapie : Journal de la Societe Francaise de Radiotherapie Oncologique* 10.*6* (2006), p. 370-376.

[156] L Simon et al., « Practical recommendations for breathing-adapted radiotherapy », in : *Cancer Radiotherapie : Journal de la Societe Francaise de Radiotherapie Oncologique* 11.*4* (2007), p. 214-224.

[157] Ryan L Smith et al., « Evaluation of linear accelerator gating with real-time electromagnetic tracking », in : *International Journal of Radiation Oncology and Biology and Physics* 74.*3* (2009), p. 920-927.

[158] Ryan L Smith et al., « Integration of real-time internal electromagnetic position monitoring coupled with dynamic multileaf collimator tracking : An intensity-modulated radiation therapy feasibility study », in : *International Journal of Radiation Oncology and Biology and Physics* 74.*3* (2009), p. 868-875.

[159] Luisa S Stark et al., « Dosimetric and geometric end-to-end accuracy of a magnetic resonance guided linear accelerator », in : *Physics and Imaging in Radiation Oncology* 16 (2020), p. 109-112.

[160] Tingshi Su et al., « Long-term survival analysis of stereotactic ablative radiotherapy versus liver resection for small hepatocellular carcinoma », in : *International Journal of Radiation Oncology and Biology and Physics* 98.*3* (2017), p. 639-646.

[161] Hyuna Sung et al., « Global cancer statistics 2020 : GLOBOCAN estimates of incidence and mortality worldwide for 36 cancers in 185 countries », in : *CA : A Cancer Journal for Clinicians* 71.*3* (2021), p. 209-249.

[162] C. Tan et al., « A Survey on Deep Transfer Learning », in : *arXiv* (2018).

[163] José D Tascón-Vidarte et al., « Accuracy and consistency of intensity-based deformable image registration in 4DCT for tumor motion estimation in liver radiotherapy planning », in : *Plos One* 17.*7* (2022), e0271064.

[164] Robert Tibshirani, « Regression shrinkage and selection via the lasso », in : *Journal of the Royal Statistical Society Series B : Statistical Methodology* 58.*1* (1996), p. 267-288.

[165] Andros Tjandra et al., « Gated recurrent neural tensor network », in : *2016 International Joint Conference on Neural Networks (IJCNN)*, IEEE, 2016, p. 448-455.

[166] Tarraf Torfeh et al., « Geometric accuracy of the MR imaging techniques in the presence of motion », in : *Journal of Applied Clinical Medical Physics* 19.*2* (2018), p. 168-175.

[167] Marguerite Tyran et al., « Retrospective evaluation of decision-making for pancreatic stereotactic MR-guided adaptive radiotherapy », in : *Radiotherapy and Oncology* 129.*2* (2018), p. 319-325.

[168] Prescilla Uijtewaal et al., « Dosimetric evaluation of MRI-guided multi-leaf collimator tracking and trailing for lung stereotactic body radiation therapy », in : *Medical Physics* 48.*4* (2021), p. 1520-1532.

[169] Prescilla Uijtewaal et al., « First experimental demonstration of VMAT combined with MLC tracking for single and multi fraction lung SBRT on an MR-linac », in : *Radiotherapy and Oncology* 174 (2022), p. 149-157.

[170] René W.M. Underberg et al., « Four-dimensional CT scans for treatment planning in stereotactic radiotherapy for stage I lung cancer », in : *International Journal of Radiation Oncology and Biology and Physics* 60 (4 2004), p. 1283-1290.

[171] S Vedam et al., « Dosimetric impact of geometric errors due to respiratory motion prediction on dynamic multileaf collimator-based four-dimensional radiation delivery », in : *Medical Physics* 32.*6* (2005), p. 1607-1620.

[172] SS Vedam et al., « Determining parameters for respiration-gated radiotherapy », in : *Medical Physics* 28.*10* (2001), p. 2139-2146.

[173] SS Vedam et al., « Predicting respiratory motion for four-dimensional radiotherapy », in : *Medical Physics* 31.*8* (2004), p. 2274-2283.

[174] Namrata VIJAYVERGIA, Prashant C SHAH et Crystal S DENLINGER, « Survivorship in non–small cell lung cancer : challenges faced and steps forward », in : *Journal of the National Comprehensive Cancer Network* 13.*9* (2015), p. 1151-1161.

[175] Shalini K VINOD et Eric HAU, « Radiotherapy treatment for lung cancer : Current status and future directions », in : *Respirology* 25 (2020), p. 61-71.

[176] Jihong WANG et al., « Assessment of image quality and scatter and leakage radiation of an integrated MR-LINAC system », in : *Medical Physics* 45.*3* (2018), p. 1204-1209.

[177] Ran WANG et al., « A feasibility of respiration prediction based on deep Bi-LSTM for real-time tumor tracking », in : *IEEE Access* 6 (2018), p. 51262-51268.

[178] Lineke van der WEIDE et al., « Analysis of carina position as surrogate marker for delivering phase-gated radiotherapy », in : *International Journal of Radiation Oncology and Biology and Physics* 71.*4* (2008), p. 1111-1117.

[179] Anita M WERENSTEIJN-HONINGH et al., « Feasibility of stereotactic radiotherapy using a 1.5 T MR-linac : Multi-fraction treatment of pelvic lymph node oligometastases », in : *Radiotherapy and Oncology* 134 (2019), p. 50-54.

[180] Christopher G WILLETT et al., « The effect of the respiratory cycle on mediastinal and lung dimensions in Hodgkin's disease. Implications for radiotherapy gated to respiration », in : *Cancer* 60.*6* (1987), p. 1232-1237.

[181] Cort J. WILLMOTT et Kenji MATSUURA, « Advantages of the mean absolute error (MAE) over the root mean square error (RMSE) in assessing average model performance », in : *Climate Research* 30.*1* (2005), p. 79-82, DOI : `10.3354/CR030079`.

[182] Twyla R WILLOUGHBY et al., « Target localization and real-time tracking using the Calypso 4D localization system in patients with localized prostate cancer », in : *International Journal of Radiation Oncology and Biology and Physics* 65.*2* (2006), p. 528-534.

[183] Dennis WINKEL et al., « Target coverage and dose criteria based evaluation of the first clinical 1.5 T MR-linac SBRT treatments of lymph node oligometastases compared with conventional CBCT-linac treatment », in : *Radiotherapy and Oncology* 146 (2020), p. 118-125.

[184] Dirk Wolff et al., « Volumetric modulated arc therapy (VMAT) vs. serial tomotherapy, step-and-shoot IMRT and 3D-conformal RT for treatment of prostate cancer », in : *Radiotherapy and Oncology* 93.*2* (2009), p. 226-233.

[185] John W Wong et al., « The use of active breathing control (ABC) to reduce margin for breathing motion », in : *International Journal of Radiation Oncology and Biology and Physics* 44.*4* (1999), p. 911-919.

[186] Huanmei Wu et al., « Gating based on internal/external signals with dynamic correlation updates », in : *Physics in Medicine and Biology* 53.*24* (2008), p. 7137.

[187] Changfa Xia et al., « Cancer statistics in China and United States, 2022 : profiles, trends, and determinants », in : *Chinese Medical Journal* 135.*05* (2022), p. 584-590.

[188] Qianyi Xu et al., « Quantifying rigid and nonrigid motion of liver tumors during stereotactic body radiation therapy », in : *International Journal of Radiation Oncology and Biology and Physics* 90.*1* (2014), p. 94-101.

[189] Juan Yang et al., « Is diaphragm motion a good surrogate for liver tumor motion ? », in : *International Journal of Radiation Oncology and Biology and Physics* 90.*4* (2014), p. 952-958.

[190] SA Yoganathan et al., « Predicting respiratory motion using a novel patient specific dual deep recurrent neural networks », in : *Biomedical Physics and Engineering Express* 8.*6* (2022), p. 065013.

[191] Shumei Yu et al., « Rapid prediction of respiratory motion based on bidirectional gated recurrent unit network », in : *IEEE Access* 8 (2020), p. 49424-49435.

[192] Yong Yue et al., « Geometric Validation of K-Space Self-Gated 4D-MRI Vs. 4D-CT Using A Respiratory Motion Phantom », in : *Medical Physics* 41.*6* (2014), p. 572-573.

[193] Li Yupeng et al., « On the interplay effects with proton scanning beams in stage III lung cancer », in : *Medical Physics* 41.*2* (2014).

[194] Siwei Zhang et al., « Cancer incidence and mortality in China, 2015 », in : *Journal of the National Cancer Center* 1.*1* (2021), p. 2-11.

[195] Yuting Zhao et al., « Observation of different tumor motion magnitude within liver and estimate of internal motion margins in postoperative patients with hepatocellular carcinoma », in : *Cancer Management and Research* (2017), p. 839-848.

[196] LGM Zwart et al., « Cone-beam computed tomography-guided online adaptive radiotherapy is feasible for prostate cancer patients », in : *Physics and Imaging in Radiation Oncology* 22 (2022), p. 98-103.

[197] Lisanne GM Zwart et al., « Cone-beam computed tomography-guided online adaptive radiotherapy is feasible for prostate cancer patients », in : *Physics and Imaging in Radiation Oncology* 22 (2022), p. 98-103.

COLLEGE MATHS, TELECOMS
DOCTORAL INFORMATIQUE, SIGNAL
BRETAGNE SYSTEMES, ELECTRONIQUE

Université
de Rennes

Titre : Schéma de Gating spécifique au patient pour la radiothérapie de tumeur thoracoabdominale guidée par l'imagerie par résonance magnétique

Mot clés : MR-Linac ;Gating ;Suivi des tumeurs ;Prédiction du mouvement respiratoire

Résumé : L'objectif de cette thèse est de développer un système de synchronisation pour la compensation en temps réel des mouvements lors du traitement du cancer du poumon et du foie sur l'Elekta Unity. Ce système surveillera et localisera automatiquement la position tridimensionnelle de la tumeur en temps réel, et prédira sa trajectoire à 0.5 seconde. Un signal sera généré pour contrôler le faisceau pendant la radiothérapie, réduisant ainsi les inexactitudes dues au mouvement respiratoire.

Validation de l'efficacité du KCF dans le suivi des tumeurs en 2D sur des images IRM ciné. Proposition d'un modèle C-NLSTM spécifique au patient pour une meilleure prédiction du mouvement des tumeurs. Validation de la régression linéaire pour la prédiction du mouvement en utilisant des images MR ciné 2D. Intégration des travaux pour une solution complète de compensation des mouvements respiratoires, validée par étude dosimétrique pour protéger les organes à risque.

Title: Patient-specific gating scheme for thoracoabdominal tumor radiotherapy guided by magnetic resonance imaging

Keywords: MR-Linac; Gating; Tumor tracking; Respiratory motion prediction

Abstract: The aim of this thesis is to develop an end-to-end gating system for real-time motion compensation during lung and liver cancer treatment on the Elekta Unity. This system will monitor and automatically locate the three-dimensional position of the tumor in real-time and predict its trajectory within 0.5 seconds. A gating signal will be generated to control the beam on and off during radiotherapy, reducing inaccuracies in dose delivery due to respiratory motion.

The effectiveness of KCF in tracking tumors in 2D cine MRI images will be validated. A patient-specific C-NLSTM model is proposed for better tumor motion prediction. The effectiveness of linear regression for motion prediction using 2D cine MR images will be validated. Integrating the above studies, a complete respiratory motion compensation solution is proposed, which is validated by dosimetric studies to protect surrounding organs at risk.